DIPLOMA THESIS

Combined Thermogravimetric Analysis and Laser-induced Breakdown Spectroscopy measurements investigating hydrogen uptake in proton conducting oxides

(Thermogravimetrische und Laser-induzierte Plasmaspektroskopie Messungen zur Untersuchung der Wasserstoff-Aufnahme in protonenleitenden Oxiden)

Author: Alexander Holzer
Matr.Nr.: 11701291

carried out for the purpose of obtaining the degree **Diplom-Ingenieur (Dipl.-Ing.),** international comparable to **Master of Science (MSc),** as part of the master's programme Technical Chemistry (UE 066 490) with the specialisation in Applied Physical and Analytical Chemistry.

Supervised by

Assistant Prof. Dipl.-Ing. Dr.techn. Alexander Opitz,
Univ.Prof. Dipl.-Ing. Dr.techn. Andreas Limbeck
Dipl.-Ing. Dr.techn. Maximilian Weiss
Dipl.-Ing. Martin Krammer

Conducted at

Research Group Electrochemical Energy Conversion & Research Group Surface Analytics, Trace Analytics and Chemometry,
Institute of Chemical Technologies and Analytics (E164),
Faculty of Technical Chemistry, Vienna University of Technology

Vienna, February 2023

_____
Alexander Holzer

Acknowledgements

In the beginning, I would like to express my biggest gratitude to my supervisors Alexander Opitz and Andreas Limbeck. They always had an open ear for my concerns and some advice for optimization.

It was an honour to have the opportunity making my diploma thesis in two different research groups and get to know many helpful people, that are working in different fields. Especially I want to thank Maximilian Weiss and Martin Krammer for their advice and practical support at any time. Furthermore, I want to mention Harald Summerer for giving me insight in his diploma thesis that helped me a lot in the beginning and for providing some of his samples. Melanie Anstiss showed me how to synthesize the Y-doped barium zirconate powder and had an open door to listen to any problems I was concerned with.

I do not want to forget my friends, my student buddies, and my family, for which I am very grateful.

All in all, without these people, this diploma thesis wouldn't have been possible. Thanks for your support!

Abstract

Due to the ever-growing energy consumption, energy production, conversion and storage of renewable energy have become more important. Alternative energy carriers like hydrogen, produced via electrolysis of water and converted back to electrical energy with fuel cells, are expected to solve the problem of long-term energy storage. Proton ceramic electrochemical cells are promising candidates for both the electrolysis and the fuel cell operation. Proton conductivity in perovskite oxides typically arises from the uptake of water into oxygen vacancies. In literature, resulting weight changes or conductivity measurements are used for determination of the proton concentration. However, no spatially resolved information is available from these techniques.

In this thesis, a promising proton-conducting electrolyte material, yttrium-doped barium zirconate (BZY), is analysed by two different techniques: thermogravimetric analysis (TGA) and laser-induced breakdown spectroscopy (LIBS). The main goal is the optimization and the comparison of both techniques, which allows to get spatially resolved information via LIBS in addition to the overall water and thus proton uptake from TGA measurements. The TGA measurements help to control the determined hydrogen concentration of the LIBS measurements.

For the quantification of hydrogen in the oxide material by LIBS, matrix matched standards were prepared to create a calibration curve. Therefore, zirconium hydroxide and barium zirconate were used.

The water incorporation for dried in-house sintered BZY-pellets at 550°C result in 0.0319 wt. % H and is thus comparable to theory and literature results.

The optimized TGA measurement includes a drying step with argon, a treatment at the optimal temperature for water incorporation for stabilization with dry argon and the incorporation of water with humidified argon at the same temperature. Moreover, the results from TGA and LIBS are comparable to ex-situ measurements.

It can be concluded that the introduction of LIBS and TGA combined measurements opens the possibility to establish this method for characterisation of proton conducting oxide materials. Furthermore, first hydrogen depth profiles were measured by applying two different implementations.

Zusammenfassung

Aufgrund des stetig-wachsenden Energieverbrauchs, bekommen Energieerzeugung, Energieumwandlung und Speicherung erneuerbarer Energie eine bedeutendere Rolle. Alternative Energieträger wie beispielsweise Wasserstoff, der durch Elektrolyse von Wasser hergestellt und mit Brennstoffzellen wieder in elektrische Energie umgewandelt werden kann, haben das Potential das Problem der langfristigen Energiespeicherung zu lösen. Protonenleitende keramische elektrochemische Zellen sind vielversprechende Kandidaten sowohl für die Elektrolyse als auch für den Brennstoffzellenbetrieb. Die Protonenleitfähigkeit in Perowskit-oxiden entsteht typischerweise durch die Aufnahme von Wasser in Sauerstoffleerstellen. In der Literatur werden resultierende Gewichtsänderungen oder Leitfähigkeitsmessungen zur Bestimmung der Protonenkonzentration herangezogen. Durch diese Techniken sind jedoch keine ortsaufgelösten Informationen erhältlich.

In dieser Arbeit wird ein vielversprechendes protonenleitendes Elektrolytmaterial, Yttrium-dotiertes Bariumzirkonat (BZY), mit zwei verschiedenen Techniken analysiert: Thermogravimetrische Analyse (TGA) und laserinduzierte Plasmaspektroskopie (LIPS, engl. LIBS). Das Hauptziel dieser Arbeit ist die Optimierung und der Vergleich beider Techniken, die es ermöglichen, zusätzlich zur gesamten Wasser- und damit Protonenaufnahme aus TGA-Daten ortsaufgelöste Informationen mittels LIBS zu erhalten.

Für die Quantifizierung von Wasserstoff im Oxidmaterial wurden matrixangepasste Standards hergestellt, um eine Kalibrationsgerade zu erstellen. Hierfür wurde Zirkoniumhydroxid und Bariumzirkonat verwendet.

Die Wasseraufnahme für getrocknete hausintern gesinterte BZY-Pellets bei 550°C ergibt 0,0319 Gew.-%. H und ist somit vergleichbar mit Theorie- und Literaturergebnissen.

Die optimierte TGA-Messung beinhaltet einen Trocknungsschritt mit Argon, eine Behandlung bei optimaler Temperatur zur Wasseraufnahme unter trockenem Argon zur Stabilisierung und den Einbau von Wasser mit befeuchtetem Argon bei gleicher Temperatur. Darüber hinaus sind die Ergebnisse von TGA und LIBS zu ex-situ Messungen vergleichbar.

Es konnte gezeigt werden, dass die Einführung kombinierter LIBS- und TGA-Messungen die Möglichkeit eröffnet, dies zur Charakterisierung von protonenleitenden Oxidmaterialien zu etablieren. Weiters wurden erste Wasserstoff-Tiefenprofile mit zwei verschiedenen Durchführungen gemessen.

Table of Contents

List of abbreviations

AFC	Alkaline fuel cell
ANN	Artificial neural network
BZYX, BYZX	X mol% Yttrium-doped barium zirconate
CCD	Charge coupled device
CF-LIBS	Calibration free laser induced breakdown spectroscopy
CRM	Certified reference materials
DCFC	Direct carbon fuel cell
DFT	Density functional theory
DMFC	Direct methanol fuel cell
DTA	Differential thermal analysis
GC-MS-FTIR	Gas Chromatography-Mass Spectroscopy– Fourier Transformation Infrared Spectroscopy
GDC	Gadolinium doped ceria
ICCD	Intensified charge coupled device
ICP-MS	Inductively coupled plasma mass spectroscopy
ICP-OES	Inductively coupled plasma optical emission spectroscopy
IHS BZY15 Pellet	In-house sintered 15 mol% Y-doped barium zirconate pellet
LA-ICP-MS	Laser Ablation – Induced Coupled Plasma – Mass Spectroscopy
LIBS	Laser induced breakdown spectroscopy
LOD	Limit of detection
MCFC	Molten carbonate fuel cell
MLR	Multilinear regression
Nd:YAG	Neodym-doped yttrium aluminium garnet
NRRA	^{15}N nuclear resonance reaction analysis
PAFC	Phosphoric acid fuel cell
PEMFC	Proton exchange membrane fuel cell
PLS	Partial least squares
SIMS	Secondary ion mass spectroscopy
SOFC	Solid oxide fuel cell
SVM	Support vector machine
TGA	Thermogravimetric analysis
XRD	X-Ray diffraction
XRF	X-Ray fluorescence
YSZ	Yttria stabilized zirconia

1. Introduction

1.1. The role of proton conductors for energy conversion

The expanding population and increase of energy consumption per capita bring new challenges in near future[1]. Züttel et al. [2] predicted a worldwide average consumption of 2 kW per capita. Often the increase in efficiency is directly connected to an increase in energy consumption and economy growth. In history this phenomenon appeared, when James Watt improved the efficiency of the steam engine by a factor of four[2]. This introduced the industrialization[2].
Already in 1896 Svante Arrhenius suggested to reduce the CO_2 emission. Emissions affect our environment: Doubling of the atmosphere's carbon dioxide content would cause an average temperature rise of 3-6°C. [2], [3]
A problem is often attached to options of answers, restricted to your settings. The future sustainable energy should be a secure supply, locally available to rule out dependency and environmentally friendly, especially by decreasing the global carbon dioxide production. Furthermore, green energy is often produced, when the demand is low, hence energy storage systems are needed to tackle for this issue.
Energy storing often includes energy loss and many of these difficulties can be solved by the energy carrier hydrogen. The European Commission predicted for 2040 that 35 % of the newly produced vehicles will run by zero-carbon hydrogen[4].

A main advantage of hydrogen is the more than doubled gravimetric energy storage capacity compared to conventional fuels[1]. The big difference occurs because conventional combustion engines convert chemical energy into heat and further to mechanical energy. This way of transformation is always connected to a significant energy loss. A solution for this problem is a fuel cell. Fuel cells in general use the chemical energy directly and more efficiently to produce the most valuable energy type, electrical energy[1]. The internal circuit via ion transfer allows to produce energy in the external circuit via electron transfer[5]. The main components of a fuel cell are an electrolyte, an anode, a cathode and, if multiple cells are connected in series to yield a stack, an interconnect material. The different fuel cell types available are commonly distinguished on the basis of their electrolyte, since this has a significant influence on the cell's operating characteristics such as temperature: Proton exchange membrane fuel cell (PEMFC), solid oxide fuel cell (SOFC), molten carbonate fuel cell (MCFC), phosphoric acid fuel cell (PAFC), alkaline fuel cell (AFC) and some more special types like the direct carbon fuel cell (DCFC), or the direct methanol fuel cell (DMFC).[6]

Solid oxide fuel cells show many advantages, like high electrical efficiency, high tolerance to contaminants, fuel flexibility and inexpensive catalysts[6]. Depending on the mobile ion in the ceramic electrolyte, they can be divided in proton and oxide conducting SOFCs. Proton conducting SOFCs show a higher theoretic efficiency due to the fact, that water is formed on the cathode and hence hydrogen is not diluted upon operation[7], [8]. For proton conducting SOFCs different electrolyte materials are used. One very promising electrolyte is Y-doped barium zirconate (BZY), which is typically operated at temperatures of about 600°C and therefore opens the possibility to use methane as fuel gas[9]. Furthermore, the material shows high chemical stability towards CO_2 and high proton conductivity at lower temperatures[10]–[13].

1.2. Analytical methods for characterization of proton conductors

To further improve the efficiency of proton conducting SOFCs, methods for characterisation and determination of functionality of the electrolyte are necessary. Commonly, the proton concentration is determined indirectly by thermogravimetric analysis (TGA) of the material's water uptake in humidified atmosphere.

Fabbri et al.[14] analysed BZY30, BZY40, BZY50 and BZY60 powders. The water uptake experiment included a drying step at 1000°C and dry nitrogen for one hour followed by decreasing temperature in steps of 200°C. For each temperature a dwell time of 2 h was maintained to equilibrate the material to the humidified atmosphere (p_{H_2O}=0.03 atm).
Goncalves et al.[15] analysed BZY10, BZY20 and BZY30 powders. First a drying step at 1000°C for 30 min was done under dry air and secondly humidified air (p_{H_2O}=0.021 atm) was used while reducing the temperature in steps of 100°C. Equilibration times of 3 h for each temperature were programmed.

In comparison, Yamazaki et al.[16] analysed BZY20, BZY30, BZY40 and undoped $BaZrO_3$ powder by thermogravimetric analysis. The water uptake experiment included a drying step at 1000°C for 0.5 h under dry nitrogen to remove water and possibly surface carbon dioxide. The gas phase was saturated by water (p_{H_2O}=0.023 atm) and the temperature decreased by steps of 100°C to room temperature with equilibration times of 2 h. For the temperature range of 50-500°C, where the equilibrium constant behaves Arrhenius-like, thermodynamic parameters were calculated. For the complete change in entropy by water vapor dissolution, a higher weight change was suspected than the measured experimental values. Therefore, heat capacity measurements could help to understand the difference in entropy. The high temperature measurements include weight changes due to oxidation and hydration and this can not be distinguished by thermogravimetric analysis because only the resulting weight change is registered and no information about the chemical species is available. To resolve this, thermal analysis under dry oxygen would be an opportunity. Goncalves et al.[15] compared direct isothermal water uptake calorimetry measurements with thermogravimetry experiments and calculated the hydration energies. For calorimetry measurements, the instrument must be calibrated against the standard enthalpy of fusion of metallic gallium. The measurements included a degassing step, a cooling step for measuring the free space volume and the water uptake with an incremental dose mode step. Here the heat effect is measured and by dividing the amount of water and mass of the sample, the hydration enthalpy can be calculated.

Yamazaki et al.[16] and Fabbri et al.[14] showed that the proton concentration due to water uptake increases with increasing Y content for Y-doped barium zirconate. This is because of the linear relationship between the yttrium concentration and the oxygen vacancies in the BZY lattice.

Since TGA only delivers weight changes but does not provide information on the mobility of these point defects additional techniques are required to obtain information on the material's conductivity. For measuring this quantity, electrochemical impedance spectroscopy can be employed. Impedance spectroscopy allows to extract bulk resistances from the complex impedance as a function of used frequency. Impedance spectroscopy measurements[17]–[19] show the excellent proton conductivity of BZY10 in the order of 0.04 $\Omega^{-1}cm^{-1}$ at 400°C.
However, at temperatures significantly above 600-700°C where proton concentrations are low and oxygen vacancies become mobile, at partial pressures where the respective material also conducts electronic charge carriers, impedance spectroscopy can typically only yield its total conductivity. To get a more complete picture on the relationship between water uptake and ionic conductivity of perovskite-type proton conductors, complementary analytical measurements of the proton concentration are thus highly desirable.

Hydrogen is an element which can directly be analysed only by a few analytical techniques. In literature infrared spectroscopy[20], [21], Neutron deflection[22], [23], hydrogen nuclear magnetic resonance[24], secondary ion mass spectrometry[25], [26] and Karl-Fischer titration for analysis of water content[27]–[29] are used. Furthermore, thermogravimetric analysis[7], [14]–[16], [30]–[33] without chemical information, laser ablation – induced coupled plasma – mass spectroscopy (LA-ICP-MS) measurements[34] for deuterium and laser-induced breakdown spectroscopy[35], [36] can be used. X-ray fluorescence (XRF) and other X-ray techniques are not useable for hydrogen analysis.

Quantification of hydrogen is not easy and hence only a few techniques are available for this aim. Hydrated and dry BZY samples show little differences in their Raman spectra. Giannici et al.[37] reported sharper peaks for hydrated BZY spectra due to the smaller disturbance of single charged OH groups on anion sites in comparison to double charged oxygen vacancies. An additional peak at 548 cm^{-1} for samples directly exposed to humidified hydrogen was reported by Welander et al.[38]. They justify the additional peak because of M-O bending/stretching modes or a reconstruction of the BZY surface structure resulting in a new surface phase due to the volatile Ba. In contradiction, Karlsson et al.[39], [40] reported, that there is no systematic change in the spectra due to the humidification. Infrared spectra of different Y-doped barium zirconates by Goncalves et al.[15] show small differences. The stretching mode for the M-O (M=Zr, Y) bond in BO_6 octahedra is at 545 cm^{-1} and for higher doped barium zirconate this peak split in two peaks due to lattice distortion. The O-H stretching mode for hydrated samples at 3450 cm^{-1} is visible, but it is not possible to quantify the hydrogen.

Alternatively, the absolute hydrogen concentration can be determined by ^{15}N nuclear resonance reaction analysis (NRRA). Groß et al.[17] used the nuclear resonance reaction $^{1}H(^{15}N, \alpha\gamma)^{12}C$ and Kapton ($C_{22}H_{10}N_2O_4$) as a calibration standard. Therefore, the γ-ray yield of a sample is compared to the γ-ray yield of the calibration standard for which the hydrogen concentration is known. For BZY15, Groß et al.[17] showed that 15 mol% H is the maximum possible concentration, which is in accordance with the defect chemical model that predicts a maximum of one H_2O being incorporated per oxygen vacancy. In addition, the proton concentration in BZY15 depends on the temperature and can be calculated by the two-site model based on Fermi-Dirac statistics[17]. As a consequence, the proton concentrations at operation temperatures of proton conducting cells can be expected to be lower than the 15 mol% and indeed experimentally a hydrogen concentration of about 7.5 mol% at 550°C was measured. The hydrogen concentration is a function of the water vapour partial pressure. Increasing water vapour pressure leads to a higher hydrogen concentration. Groß et al.[17] reported the water incorporation into a 1 µm film sample at four different temperatures and a constant water vapour pressure of 100 mbar. The lower temperatures show higher hydrogen concentration, like the two-site model predicted. What was on the first glance surprising is that the sample surfaces in this study showed a little higher hydrogen concentration in comparison to the maximum theoretical possible hydrogen concentration. The authors explain this observation by adsorbed water and an almost constant hydrogen concentration in the bulk. For example, while for the bulk of a sample about 9 mol% H at 550°C are expected, its surface showed a maximum of hydrogen of about 12 mol% H at 550°C. This clearly indicates that water adsorbed to the surface may be a critical factor leading to errors in TGA measurements of hydrogen concentration in BZY and related materials. Moreover, Groß et al.[17] postulated, that the drying of the humidified BZY samples is a limiting factor for the reproducibility of the humidification. For BZY15 a residual hydrogen fraction of 1.75 mol% could not be removed at 700°C in a dried argon-oxygen (80/20) atmosphere.

In addition to quantitative chemical analysis the used materials are often characterised by XRD measurements to verify the present phases and purity. Giannici et al.[37] focused on the structure of proton-conducting Y-doped $BaZrO_3$. They used high resolution X-ray diffraction (HR-XRD) to resolve the slightly tetragonally distorted crystal structure and extended X-ray absorption fine structure (EXAFS) to determine the local environment of Zr^{4+} and Y^{3+}. It is reported that the distortion limits the Y^{3+} solubility and therefore the correlated proton conduction property. Goncalves et al.[15] used an electron probe, a wavelength dispersive spectrometry, to analyse the stoichiometry.

1.3. Synthesis routes for $BaZrO_3$-based proton conductors

Groß et al.[17] used barium carbonate, zirconia and yttria for the bulk samples. The powder mixture was milled, calcinated at 1600°C twice and pressed isostatically into pellets. Those pellets were sintered at 1600°C in air for 24 h. The films were produced by dip-coating of a single crystal silicon substrate in a precursor solution, drying at 400°C in a hot current of air, calcinating for 30 min at 600°C and sintering for 12 h at 600°C. The precursor solution includes zirconium n-propoxide in n-propanol, barium acetate and yttrium acetate.

Fabbri et al.[14] prepared BZY powder by a Pechini procedure. The authors used $Ba(NO_3)_2$, $Zr(CH_3CO_2CHCOCH_3)_2$, $Y(NO_3)_3{\cdot}6H_2O$ and citric acid as chelating agent. The metal cations and citric acid were mixed in water until a transparent solution was obtained. Ethylene glycol was added and under continuous stirring it was heated up to 180°C. A viscous gel was obtained after the polyesterification. This gel was converted into a brown ash after heating overnight. The grinded powder was calcinated at 1100°C for 8 h to obtain a single crystalline phase. [14]

1.4. Goal of this thesis

In this diploma thesis, the hydrogen uptake of Y-doped barium zirconate, which is used in solid oxide fuel cells (SOFCs), was studied. This was done by employing two different methods for the analysis of the hydrogen content in perovskite-type proton conducting oxides: thermogravimetric analysis of water uptake in humid atmosphere and laser induced breakdown spectroscopy. For TGA water uptake measurements an inhouse developed instrument was adapted to account for the peculiarities of measurements with H_2O containing gas. The hydrogen concentration, introduced by water uptake in the samples, was evaluated by measuring the mass changes and additionally quantified by LIBS measurements. By introducing the latter additional chemical information helps to interpret the TGA measurements.

For further evaluation of reproducibility of the TGA measurements, external (ex-situ) in a furnace with controlled gas supply and determination of the weight by an analytical balance at room temperature are done. Furthermore, ex-situ experiments allow a quick change of the gas atmosphere to freeze in the actual hydrogen amount, thus allowing to analyse the hydrogen content by a subsequent LIBS measurement. This also enables to investigate depth profiles of hydrogen.

Quantification by LIBS showed challenges because standards were needed and matrix effects occurred. Certified reference materials are often not available or very expensive and therefore the standards were prepared by ourselves. The choice of components is restricted by the tendency to form carbon dioxide, the hygroscopy and mechanical stability because it needs to be grinded, mixed and pressed. On the other hand, TGA measurements are not spatially resolved because only mass changes at specific temperatures are recognized. In this thesis, the benefits of both techniques are combined and thus are another step forward in the understanding of the water-uptake into $BaZrO_3$-type ceramics in more detail.

2. Theory

2.1. Hydrogen as an energy carrier and fuel cells in general

Hydrogen is the lightest and most abundant element in the universe, accounting for more than 90 % of all atoms. It shows the highest energy content, and its oxidation inside a fuel cell only produces water. [1]

One big disadvantage of gaseous hydrogen is the low volumetric energy density of about 0.01 MJ/L in comparison to gasoline (32 MJ/L). Due to the bad volumetric density, storage of large hydrogen amounts show difficulties. [5]
The gravimetric energy density of 120 MJ/kg compared to gasoline (44 MJ/kg) is very high[5]. In Table 1 the energy content of different fuels is compared. Gaseous and liquid hydrogen show the highest gravimetric energy contents, but conventional diesel and coal show the highest volumetric energy contents.

Table 1: Energy contents from some selected fuels[1]

Fuel	Gravimetric energy contents (MJ/kg)	Volumetric energy contents (MJ/L)
Gaseous hydrogen	119.96 - 141.88	0.011 - 0.013
Liquid hydrogen	120.04 - 141.77	8.523 - 10.066
Natural gas	47.13 - 52.21	0.032 - 0.036
Conventional diesel	42.78 - 45.76	35.080 - 37.523
Coal	22.73 - 23.96	29.549 - 31.148
Ethanol	26.95 - 29.84	21.264 - 23.544

There are different opportunities to produce hydrogen, mainly electrolysis, reforming and pyrolysis. Reforming is a technology for converting hydrogen containing material into a hydrogen rich stream. There are different types like hydrocarbon reforming, plasma reforming, aqueous phase reforming, ammonia reforming and some more. Pyrolysis is a similar, but without water or oxygen present. Furthermore, hydrogen can be produced from water or from biomass. Electrolysis, thermochemical water splitting, photo electrolysis are technologies for hydrogen production from water.[41]
Electrolysis needs thermodynamically 1.23 V or a thermoneutral voltage of 1.481 V at room temperature and ambient pressure[2]. To split water with less electrical energy, the temperature is lift up, e.g. to 1000°C[2]. The production of hydrogen by direct thermal dissociation needs high temperatures of about 2300°C and above[2], [42].
Hydrogen is only classified as renewable, if it is produced by electricity from renewable sources[2].

In Figure 1 the hydrogen cycle is shown. Hydrogen is produced, stored and used. The usage of hydrogen often refers to a conversion, where water is produced. Thus, the hydrogen cycle closes and hydrogen can be produced in the next cycle.

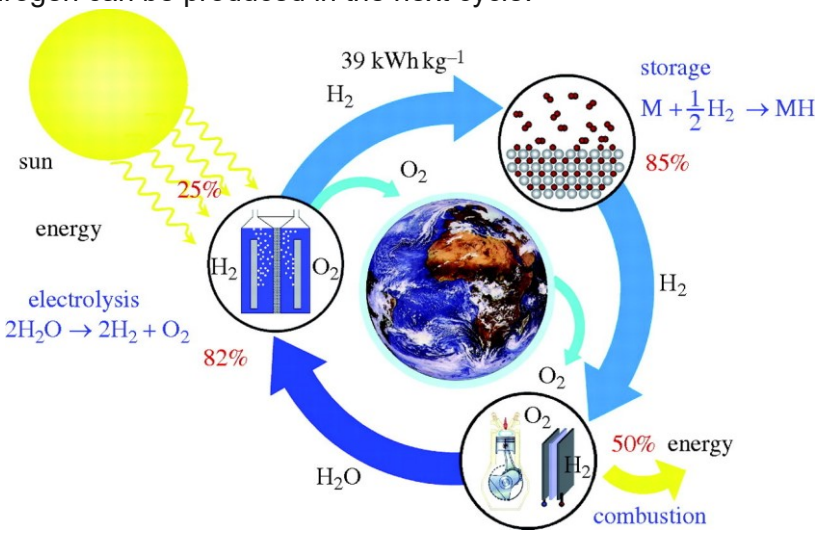

Figure 1: The hydrogen cycle: Hydrogen is produced by electrolysis of water using electrical energy, stored by different techniques and converted. The conversion product water can be used for further electrolysis, which closes the hydrogen cycle. [2]

There are three different hydrogen storage systems: gaseous, liquid and solid-state storage systems[1]. Furthermore, stationary and mobile hydrogen storage systems need different requirements. The U.S. Department of Energy (DOE) goals determine the storage parameter that should be achieved: the gravimetric capacity, volumetric capacity, operating temperature and cycle life is defined. The most used technique for hydrogen storage is compressed hydrogen in carbon fibre reinforced plastic tanks. Cryogenic storage and more often cryo-compressed storage is a good alternative technique. The additional compression prevents the evaporation losses that cryogenic storage includes. The application for transportation vehicles is very important and it makes the longest driving distance and no evaporative losses while parking for eight hours possible. It is the only technique that reached the DOE 2017 target values. The third storage system includes solid-state techniques which work by adsorption and/or absorption including metal or chemical hydrides, high surface area sorbents like metal-organic frameworks (MOFs) or carbon-based materials. This storage technique shows a high safety level. However, often solid-state hydrogen storage materials show low storage capacities. [1], [5]

When electrical energy is needed, hydrogen can be converted to electrical energy in a fuel cell by generating electricity in the external circuit and internal ion transfer.
There are plenty different fuel cells, some of them are compared by their power density and specific power in Figure 2. Additionally, there are generators, combustion engines and photovoltaic cells compared as well. Portable and transportation applications should be light and small in volume, therefore volumetric (power density) and gravimetric power density (specific power) are important performance characteristics. [43]

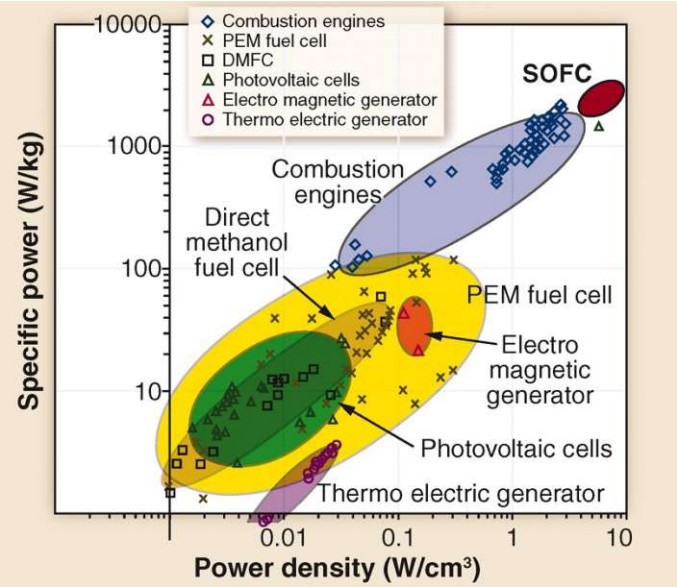

Figure 2: Comparison of solid oxide fuel cells (SOFCs) with other energy conversion devices in their power density and specific power[43]

SOFCs show an electrical efficiency of about 65 % and by combined heat and power application the efficiency can be raised up to more than 85 %[43].
Another option to increase the theoretical efficiency is to decrease the temperature. At 900°C 63 % is elevated to 81 % at 350°C. PEMFC show in comparison a higher electrical efficiency of about 50 – 70 %, while operating at lower temperatures of about 80°C[44]. The used hydrogen needs to be prepared, for example by water gas shift or electrolysis and this decreases the overall efficiency. Additionally, carbon monoxide is a poison for PEMFCs and therefore high purity is needed which is combined with high costs. [43]

A big advantage of solid oxide fuel cells (SOFCs) in comparison to polymer electrolyte fuel cells (PEMFCs) is the fuel flexibility. The existing hydrocarbon fuel infrastructure can be used and efficiency is increased compared to combustion engines. Furthermore, corresponding CO_2 emissions are reduced. To apply fuel cells for transportation systems the operating temperature needs to be decreased to low or intermediate temperature range to become more feasible. [7], [43]

There are two different types of SOFCs, the proton-conducting (H^+-SOFC) and the oxide-conducting SOFC (O^{2-}-SOFC), see Figure 3. H^+-SOFCs show a higher ionic conductivity, a higher electrical efficiency and a lower activation energy of H^+-transport compared to O^{2-}-transport[7], [45].

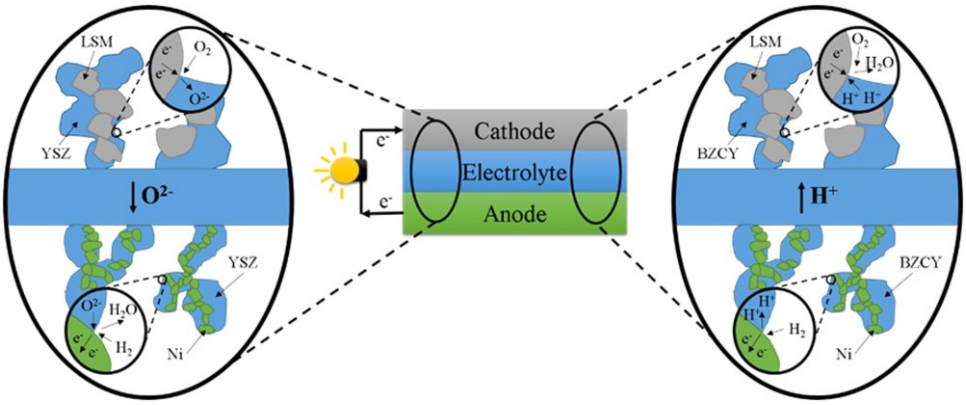

Figure 3: Schematic overview of solid oxide fuel cells (SOFCs): Oxide- and proton-conducting SOFC[7]

For oxide-conducting SOFCs the electrode reactions are given by

$$\text{Cathode: } \frac{1}{2}O_2 + 2e^- \rightarrow O^{2-} \quad \textbf{(1)}$$

$$\text{Anode: } H_2 + O^{2-} \rightarrow H_2O + 2e^- \quad \textbf{(2)}$$

Typical O^{2-}-conducting electrolytes are yttria stabilized zirconia (YSZ) and gadolinium doped ceria (GDC). On the anode-side the fuel gas is added and for oxide-conducting SOFCs there the water is produced and dilutes the fuel. This leads to lower efficiency. [7], [8]

For proton-conducting SOFCs the water is produced on the cathode, which brings a big advantage that hydrogen is not diluted and the resulting higher fuel utilization increases cell efficiency.

$$\text{Cathode: } 2H^+ + \frac{1}{2}O_2 + 2e^- \rightarrow H_2O \quad \textbf{(3)}$$

$$\text{Anode: } H_2 \rightarrow 2H^+ + 2e^- \quad \textbf{(4)}$$

Very promising proton-conducting electrolytes are barium zirconates ($BaZrO_3$) and barium cerates ($BaCeO_3$) doped by trivalent dopant like ytterbium or yttrium. [7]
In chapter 2.2 more details for proton-conducting materials are given.

2.2. Proton-conducting materials and applications

The electrolyte in a proton conducting solid oxide cell needs important characteristics: Sufficiently fast proton transport at intermediate or low temperatures, ideally no electronic conductivity, thermal and chemical stability of the electrolyte material in contact with fuel gas and air, and compatibility with the other materials used. The higher operating temperatures of proton conducting ceramic cells compared to PEM cells, allows the use of methane-containing fuel and will be important for a continuous transition of methane to hydrogen in future[9].

Proton conducting oxide materials like $BaTiO_3$ and ZnO were already mentioned in the 1940s and barium zirconate in 1993 by H. Iwahara[46]–[49]. The combination of high proton conductivity and thermodynamic stability make acceptor doped perovskite-type oxides relevant for many applications[10].

Doped $BaZrO_3$ is chemically stable and a good proton-conducting electrolyte at intermediate temperatures of 400-650°C due to the low activation energy of proton transport[37], [50].

In general, the activation energy is determined in the Arrhenius equation and the conductivity $\boldsymbol{\sigma}$ can be determined with the following equation.

$$\boldsymbol{\sigma} = \frac{\mathrm{A}}{T} \cdot \exp\left(-\frac{E_a}{RT}\right) \quad \textbf{(5)}$$

A is the preexponential factor, which is built up by the number of possible jump directions, the jump distance, the fraction of jump destinations that are vacant, the vibration frequency and the jump entropy. Therefore, the preexponential factor A contains information about the charge carrier, microstructure and crystallography of the sample. In equation (5) the molar gas constant R, the temperature T and the activation energy E_a is in the exponential part of the Arrhenius equation. [51]

2.2.1. Perovskites and proton conducting mechanism

Perovskites have the general chemical formula ABX_3 and A usually describes the large cation, B the smaller cation and X is an anion. Perovskites have important applications, e.g.: Barium titanate as a ferroelectric perovskite is used as a piezoelectric material, like the majority of ferroelectric perovskites[49].
There are four groups of perovskite with a high proton conductivity: cerate-based, zirconate based, single doped zirconate-cerate-based and hybrid-doped zirconate-cerate based proton conductors. $BaCeO_3$ is highly basic and it easily reacts with water vapour or carbon dioxide to barium hydroxide or barium carbonate. [7]
By using different dopants, the crystal structure changes. The Goldschmidt tolerance factor t is a general factor for perovskites to predict the lattice distortions:

$$\mathrm{t} = \frac{(r_A + r_X)}{\sqrt{2}(r_B + r_X)} \quad \textbf{(6)}$$

Here r_A is the radius of the cage site cation and r_B is the radius of the surrounding octahedrally coordinated cation. The radius of the anion is called r_x.[49]
Zero lattice distortion is predicted when the ionic radii of the cations perfectly matches in the cubic structure, then the factor t equals one. For oxides a range for the factor t of 0.9-1.0 predicts cubic perovskite structure. For t>1 a hexagonal packing (large A and small B) of AX_3 layers is a reasonable possibility. In the range of 0.71-0.9 a structure of lower symmetry than cubic and for even smaller values the ilmenite structure is predicted[37], [49].

Undoped barium zirconate has a t-factor of 1.004, so Ba^{2+} and Zr^{4+} match well and the unit cell is cubic. Y-doped BZY includes Y^{3+} with an ionic radius of 0.9 Å instead of 0.72 Å of Zr^{4+}, so a distortion is predicted[37]. In Table 2 different acceptor dopants in barium zirconate are compared in their ionic radius. The influence of the ion radius on the structure, resulting in different protonic defect mobility is shown in Figure 4.

Table 2: Ratio of ionic radii of different dopants and Zr^{4+} in barium zirconate

dopant	$r / r_{Zr^{4+}}$
Gd^{3+}	1.27
Y^{3+}	1.16
Sc^{3+}	1.01
In^{3+}	1.01

The proton mobility in Y-doped barium zirconate is much higher than other materials and is illustrated in Figure 4.

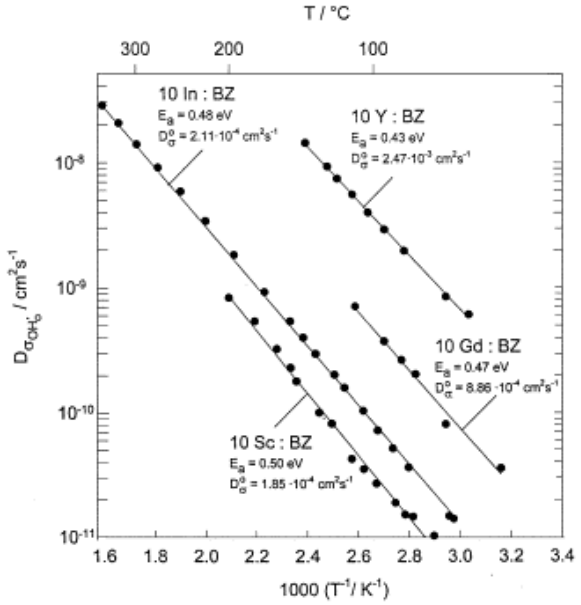

Figure 4: Protonic defect diffusion in barium zirconate with different acceptor dopants[10]

To optimize the proton conductivity the mechanism in these materials needs to be understood. In literature[52] a hopping mechanism of protons is suggested, see left side of Figure 5. The proton jumps from oxide ion to oxide ion, by forming and breaking bonds.
Kreuer[9] showed two different proton transport phenomena, the rotational diffusion, and the proton transfer (Figure 5, right side). The rotational diffusion is around the same oxide ion and the proton transfer is toward a neighbouring oxide ion. In contrast the oxygens do not show a long-range diffusion, they stay at their crystallographic positions. Experimentally it is shown by muon spin spectroscopy[53], the implementation of spin-polarized muons and the recognized change in spin motion, and quasi-elastic neutron scattering[54] that rotational diffusion is fast with low activation barriers. Additional molecular dynamics simulations do support and suggest the proton transfer as the rate-limiting step[9].

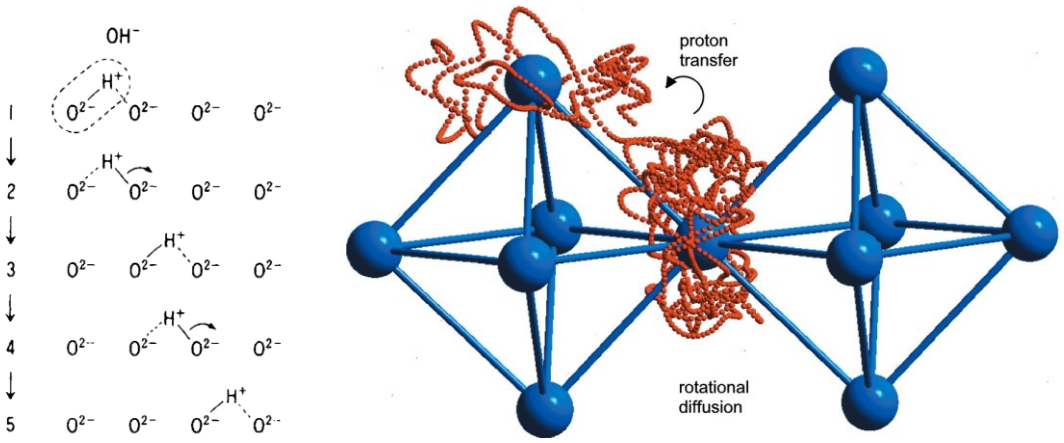

Figure 5: Possible proton conducting mechanism
(left: proton migration in perovskite-type oxide[52],
right: Proton transfer and rotational diffusion of a proton in a perovskite[9])

2.2.2. Defect chemistry

In general, conducting mechanisms include the transportation of ions inside a material. Therefore, empty ion places, so called vacancies are needed. Introducing cation or oxide-ion vacancies allows migration or incorporation of ions. These ions can migrate to the next vacancy and end up in a conductivity. Usually, the mobility of the e.g., oxide-vacancy is high enough to migrate to the surface and incorporates the ion.

Furthermore, interstitial atoms can introduce conductivity as well because the introduction of an additional ion can kick another ion and leads to migration. These vacancies and interstitials are caused by intrinsic or extrinsic defects. A common notation in defect chemistry is by Kröger and Vink to understand and describe these defects:

$$S_L^C \tag{7}$$

Here the species S can be an atom, ion, electron (e), electron hole (h) or a vacancy (V). The subscript L refers to the place where the species is located. The location can be a lattice site, e.g. at a position of an atom, or an interstitial site (i). The superscript C shows the charge difference to the perfect crystal that is introduced by the species S at the location L. Positive (•), negative (‘) and neutral relative charge (x) is possible[55]. For example, an oxygen vacancy is noted as $V_O^{\bullet\bullet}$ and indicates that the place of the oxygen is unoccupied and a positive charge is registered.

2.2.3. Y-doped Barium zirconate

High proton-conductivity at low temperatures, the possibility to use methane as fuel gas and high chemical stability towards CO_2 make Y-doped barium zirconate to a promising proton-conducting electrolyte material. To reach high stability and dense pellets, much research effort in the sintering process was needed.[10]–[13]

In general sintering of Y-doped $BaZrO_3$ is difficult. Rashid et al. reported, that electrical properties get better when the sintering temperature is higher and the grain boundary resistance is minimized as well. [7] For reducing the sintering temperature, sintering promotors, like NiO, CuO or ZnO are added[7], [24], [56], [57]. The pellets used in this study were sintered by adding NiO. A big advantage of BZY is the chemical stability towards CO_2 and the already mentioned high proton conductivity at lower temperatures[10]–[13]. In contrast $BaCeO_3$ has a high proton conductivity as well, but under CO_2 it decomposes to CeO_2 and $Ba(OH)_2$[50].
As already described in chapter 2.2, oxygen vacancies are needed for proton conduction. The Kröger Vink notation summarizes that two Zr^{4+} are substituted by two Y^{3+}, which equals one oxygen vacancy in the charge balance.

$$Y_2O_3 + 2Zr_{Zr}^{x} + O_O^{x} \rightleftarrows 2Y'_{Zr} + V_O^{\bullet\bullet} + 2ZrO_2 \qquad (8)$$

The formation of y-doped BZY is visualized in Figure 6. Here the cubic structure of barium zirconate is demonstrated on the left side. The blue zirconium ion at the position ½,½,½ with the surrounding octahedra of the oxygen ions and the barium ions in the corner position.

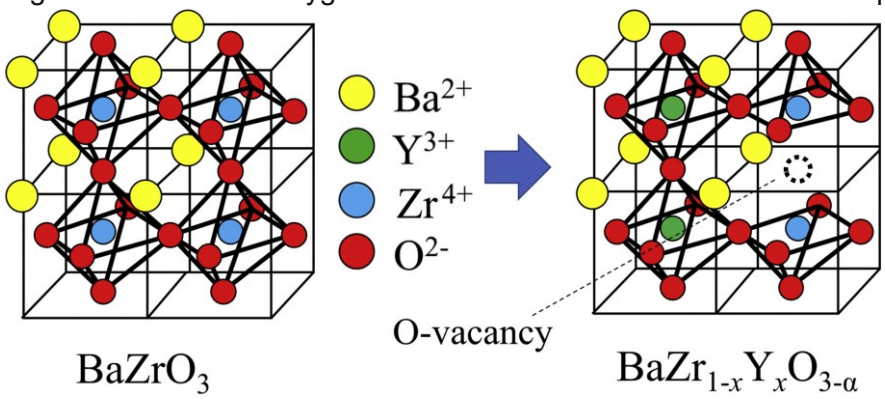

Figure 6: Formation of oxygen vacancies in Y-doped Barium zirconate [50]

BZY is very slightly tetragonally distorted due to the bigger yttrium ion, like already described in chapter 2.2. This distortion limits the Y^{+3} solubility[37]. The amount of dopant and sintering conditions influence the structure. In literature there are different crystal structures mentioned: Schober et al.[58] mentioned a cubic structure for BZY with a Y-content of zero to 10 %, Kreuer et al. published a tetragonal P4 mm unit cell for BZY10, BZY15, BZY20 and a cubic unit cell Pm-3m for BZY2, BZY5 and BZY25. Yamazaki[16] reported cubic structure for undoped $BaZrO_3$, BZY20, BZY30 and BZY40. There is some difference in literature, but generally a low dopant concentration is cubic, higher level of about 10 % to 20 % dopant concentration are tetragonal and even higher concentrations show a cubic unit cell.
Yttrium-doped barium zirconate is used as electrolyte in different electrochemical hydrogen devices, e.g., hydrogen sensors, hydrogen pumps and fuel cells. Those devices include a basic setup of two electrodes, anode and cathode, separated by a proton-conducting solid electrolyte[50].

Another promising material is Y-doped $BaCeZrO_3$ because of the higher conductivity than other Y-doped electrolytes[7], [59], [60]. Furthermore, in literature it is shown that with increased zirconium content the stability increases further, but the ionic conductivity decreases[7], [60].

2.3. Formation of protonic defects in proton conducting oxides

At moderate temperatures protonic defects are created by a dissociative absorption of water. The water in gas phase forms a hydroxide ion and a proton. The oxygen vacancy is filled by the hydroxide ion and the proton binds to a lattice oxygen.
This reaction in Kröger Vink notation

$$H_2O + V_O^{\bullet\bullet} + O_O^x \rightleftarrows 2OH_O^{\bullet} \quad (9)$$

visualizes that every water molecule creates two hydroxides, i.e., positive protonic defects, at an oxygen ion position. The diffusion of these charged defects into the bulk of a proton conducting oxide upon water incorporation is only possible with counter diffusion of oxygen ion vacancies. Consequently, for successful hydration, these oxides need an oxide ion conductivity at low water partial pressure[9].
Furthermore, Kim et al. showed by density functional theory (DFT) calculations at a BaO terminated $BaZrO_3$ (0 0 1) surface that protons have a strong tendency to segregate to the surface. The Y-acceptors compensate the positively charged hydroxide species, but some positive charge in the depth of about 3 nm is recognised. The surface behaves similar to grain boundaries[11], [61].
The appearance of electron holes (h) at high oxygen activities can be ignored for large band gap oxides at temperatures less than 750°C[62], [63]. The reaction shown in equation (9) is reversible, so the equilibrium constant for the hydration reaction can be calculated by using the concentration of the products, divided by the educts of the dissociative absorption. For water the partial pressure is used. The equilibrium constant

$$K = \frac{[OH_O^{\bullet}]^2}{p_{H_2O}[V_O^{\bullet\bullet}][O_O^x]} = \exp\left(\frac{\Delta S°}{R}\right)\exp\left(-\frac{\Delta H°}{RT}\right) \quad (10)$$

is connected to the reaction entropy S°, the reaction enthalpy H°, the gas constant R and the temperature T[9]. The site restrictions, the number of oxygen sites per formula unit of barium zirconate

$$[O_O^x] + [V_O^{\bullet\bullet}] + [OH_O^{\bullet}] = 3 \quad (11)$$

and the condition of electroneutrality (electrons and electron holes neglected)

$$2[V_O^{\bullet\bullet}] + [OH_O^{\bullet}] + [R_A^{\bullet}] - [R_B'] = 0 \quad (12)$$

is inserted in equation (10). In general, $[R_A^{\bullet}]$ and $[R_B']$ represent the dopant concentration R on the A or B place. For BZY $[R_B']$ is the concentration of yttrium positioned on zirconium sites $[Y_{Zr}']$ and $[R_A^{\bullet}]$ represents the concentration of yttrium on barium sites.
By using the effective dopant concentration $S = [R_B'] - [R_A^{\bullet}]$ the equilibrium constant is defined as

$$K = \frac{4[OH_O^{\bullet}]^2}{p_{H_2O}(S - [OH_O^{\bullet}])(6 - S - [OH_O^{\bullet}])} \quad (13)$$

and the protonic defect concentration can be calculated by the following equation[9].

$$[OH_O^{\bullet}] = \frac{3Kp_{H_2O} - \sqrt{Kp_{H_2O}(9Kp_{H_2O} - 6Kp_{H_2O}S + Kp_{H_2O}S^2 + 24S - 4S^2)}}{Kp_{H_2O} - 4} \quad (14)$$

For proton conducting oxides the hydration energy E_{hyd}, the proton-dopant association energy E_{as} and the oxygen affinity $E_{O.dopant}$ are indicator parameters for proton conductivity. The formula of the hydration energy includes those energies by adding the hydrogen affinity $E_{H.host}$.[31]

$$E_{hyd} = E_{O.dopant} + 2E_{H.host} + 2E_{as} \quad \textbf{(15)}$$

The oxygen affinity $E_{O.dopant}$ is defined as the released energy, when an oxygen vacancy is filled by an oxygen close to a dopant atom. High proton conductivity is predicted for materials with high crystal symmetry, large anion coordination number and large molar volume like in barium zirconate. Ideal materials should show a larger, more negative hydration energy and smaller, less negative association energy to enhance proton conductivity at intermediate temperatures. Large association energy leads to low mobility of the incorporated protons. [31] The hydration enthalpy of different proton-conducting materials is shown in Figure 7 and the hydration enthalpy in kJ/mol can easily be converted into the hydration energy in eV, by the factor of 1/96.485.

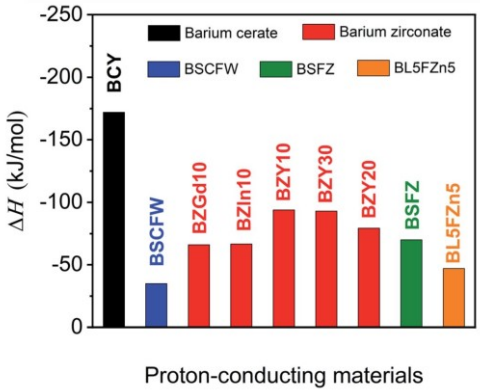

Figure 7: Hydration enthalpy of state-of-the-art proton-conducting oxides[64]

Groß et al.[17] determined the absolute content of absorbed hydrogen by ex situ ^{15}N nuclear resonance reaction analysis (NRRA) and to evaluate the thermodynamical data of the dissociative water vapor absorption in BZY15 a two-site model based on Fermi-Dirac was used, which only allows single proton occupancy and double or triple occupancy, like forming H_2O or H_3O^+ are forbidden. On the left side in Figure 8 the hydrogen content is shown as a function of the water pressure at four different temperatures. The open symbols represent bulk samples and the solid symbols data of film samples. The solid lines are simultaneous least-square fit of the hydrogen concentration and temperature dependency of water vapour partial pressure.

The right side of Figure 8 shows the temperature dependency of the hydrogen concentration at a constant water vapour pressure of 100 mbar. The two-state model based on Fermi-Dirac statistics allowed to determine the thermodynamical data, which are shown by solid squares. The open symbols represent measured data using ^{15}N NRRA. This plot refers to the importance of the drying step to realize reproduceable humidification. If the sample is only dried at lower temperatures, the complete drying is not possible and residual hydrogen fractions remain in the sample.

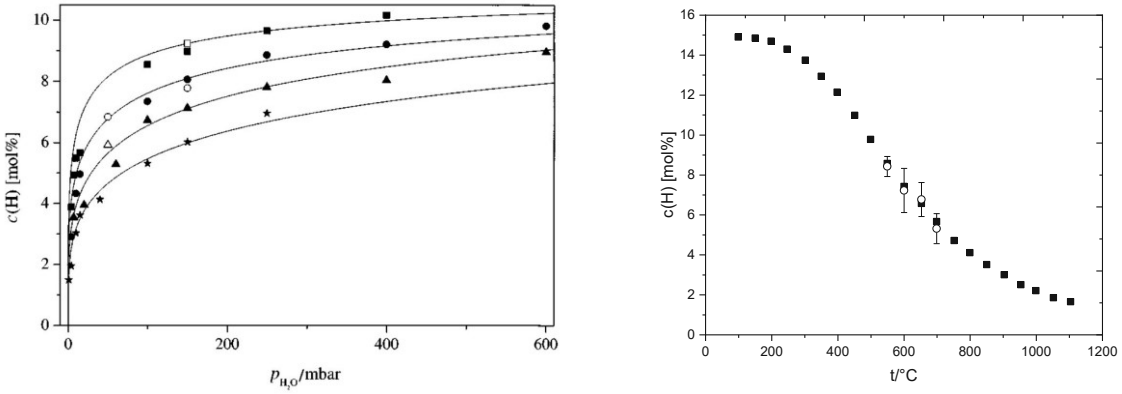

Figure 8: Water partial pressure- & temperature-dependency of proton concentration in BZY15 (left: Water vapour pressure-hydrogen composition isotherms determined at four different temperatures[17]: ■ 550°C, ● 600°C, ▲ 650°C, ★ 700°C. The solid lines represent a fit of the data. Solid symbols (open symbols) represent data of film samples (bulk samples); right: Proton concentration in BZY15 as a function of the temperature at a constant water vapour pressure of 100 mbar, modified from[17]. The solid symbols represent calculated data, the open symbols the measured data using the ^{15}N NRRA method, including the statistical errors.)

The proton conductivity is the product of proton concentration C_H or noted as $[OH_O^{\bullet}]$, proton diffusivity D_H and squared Faraday's constant F, divided by the temperature T and gas constant R – this relationship is commonly known as Nernst-Einstein relationship. [31]

$$\sigma_H = \frac{F^2\, C_H\, D_H}{RT} \tag{16}$$

The optimal doping results in high proton concentration and high proton diffusivity in the desired temperature range. Like the formula (17) and (18)(19) predict, C_H and D_H show different trends as a function of temperature. The proton concentration is higher at lower temperatures because hydration enthalpy is negative. Proton diffusivity increases with increasing temperatures.[31]

$$\mathrm{C_H} = [\mathrm{OH_O^{\bullet}}] = \sqrt{[\mathrm{V_O^{\bullet\bullet}}][\mathrm{O_O^x}]\, \mathrm{p_{H_2O}}\, \exp\left(\frac{\Delta \mathrm{S}^\circ}{\mathrm{R}}\right) \exp\left(-\frac{\Delta \mathrm{H}^\circ}{\mathrm{RT}}\right)} \tag{17}$$

Here $[\mathrm{O_O^x}]$ is the oxide-ion concentration, $[\mathrm{V_O^{\bullet\bullet}}]$ the oxygen vacancy concentration, $\mathrm{p_{H_2O}}$ the water partial pressure, $\Delta S°$ the hydration entropy, $\Delta H°$ the hydration enthalpy[31].

$$D_H = \frac{D_0 \exp\left(\frac{-\mathrm{E}_a}{\mathrm{RT}}\right)}{1 + C_{M.free}\, A \exp\left(\frac{-\mathrm{E}_{as}}{\mathrm{RT}}\right)} \tag{18}$$

For the proton diffusivity the preexponential factor D_0, the activation energy for proton diffusion E_a, the concentration of dopant atoms $C_{M.free}$, the constant related to the association entropy A and the proton-dopant association energy E_{as} is needed[31].

The formation of protonic defects, described by reaction (9), includes a significant weight increase which is usually measured by thermogravimetric analysis (TGA)[9]. This technique is described in more detail in chapter 2.4.1.
Yamazaki et al.[16] used a Netzsch STA Jupiter 449 C and Y-doped barium zirconate powders $Ba(Zr_{1-x}Y_x)O_{3-\delta}$ with x=20, 30 or 40, produced by glycine nitrate combustion synthesis and used barium-, zirconium-oxy- and yttrium-nitrate. The powder was calcinated at 1200°C for 5 h under air and attritor milled at 500 rpm for 5 h. Yamazaki et al.[16] reported, that the specific surface area can influence the water uptake kinetics and therefore determined it by the Brunauer-Emmett-Teller (BET) method. For TGA measurements, the powders were degassed for 16 h with ultrahigh-purity nitrogen at 80°C and inside the TGA heated up to 1000°C and held for 0.5 h under dry nitrogen to remove water or carbon dioxide. The water uptake is introduced by water saturated nitrogen (p_{H_2O}=0.023 atm), temperature steps of 100°C and 2 h equilibration time for each temperature. Often humidification is done by bubbling gas trough water in a riser pipe, but it is also possible to use a water vapor generator Adrop Asteam DV2MK to introduce water vapor(p_{H_2O}=0.23 atm) for the water uptake, as shown by Lesnichyova et al.[65].
In Figure 9 the water uptake of BZY is shown. The left side includes TGA measurements of the different Y-doped barium zirconates.

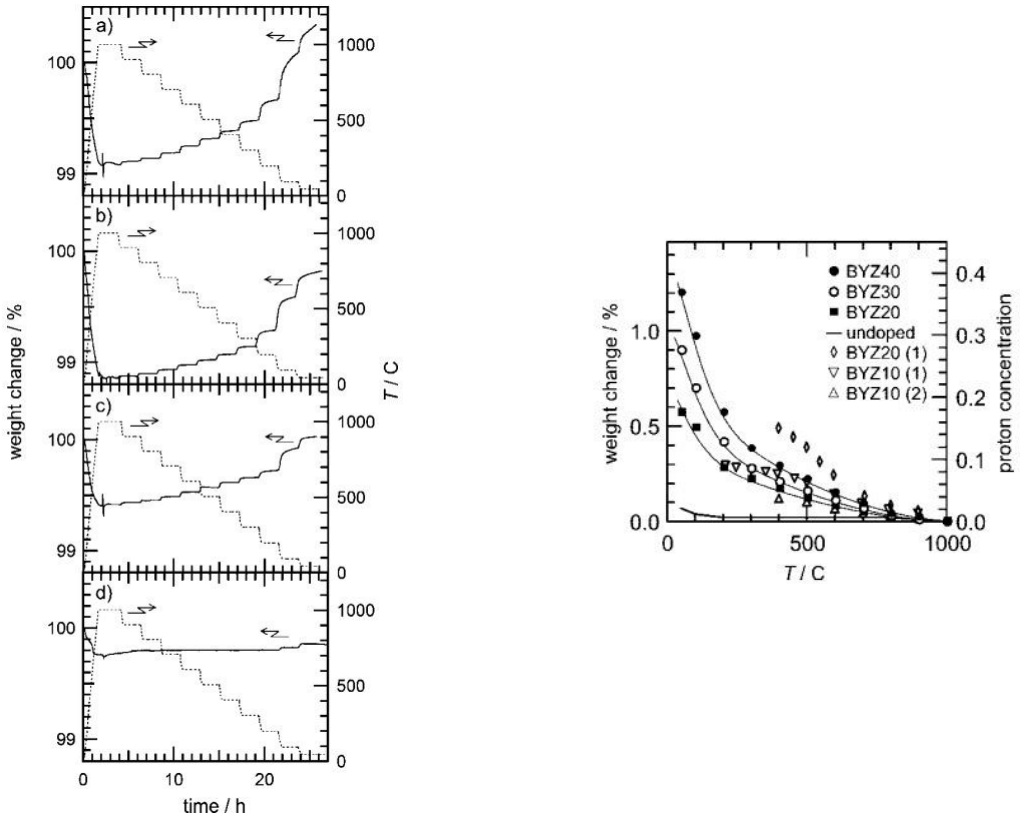

Figure 9: Water uptake of Y-doped barium zirconate[16]
(left: Weight change of BYZ40, BYZ30, BYZ20, undoped BYZ and temperature variation as function of time;
right: Weight change and proton concentration of all powders as a function of temperature and comparison to (1): Kreuer et al.[66] ; (2): Schober and Bohn[67])

The undoped barium zirconate shows an increase of ~0.07 % at 50°C. No yttrium dopant results in no extrinsic oxygen vacancies and the weight gain is due to adsorbed water molecules. Alternatively, it is also possible that some acceptor impurities were inside the

material. This increase is subtracted for the other powders, to show only the weight increase due to the y-dopant related water uptake. Those TGA measurements were used to determine the proton concentration and are compared to measurements of Schober and Bohn[67] and Kreuer et al.[66]. In conclusion the proton concentration increases with decreasing temperature and increasing yttrium content.

2.4. Methods for qualitative and quantitative analysis of hydrogen

In this thesis, TGA and LIBS measurements were done to analyse the hydrogen uptake of BZY samples. Some background regarding these methods can be found in the following sections.

2.4.1. Thermogravimetric Analysis

Thermogravimetric analysis (TGA) is a technique that records weight changes as a function of temperature. The setup includes a precision balance and a furnace including a corresponding controller for programming the temperature variation over time. By relating TGA data to physical phenomena, information about vaporisation, sublimation, absorption, adsorption and desorption can be provided. Chemical phenomena like chemisorption, desolvation (dehydration), decomposition, oxidative degradation and solid gas reactions can be tracked as well. Often it is combined with differential thermal analysis (DTA), where the heat input is measured as a function of the temperature. This enables information about physical phenomena like phase transition and fusion. [68]
A typical thermogram, a plot of sample mass change vs. temperature is shown in Figure 10. It shows different sections, where specific phenomena appear. In the first section, physisorbed water and volatile compounds, solvents and trapped gases evolve below 150 °C. In the second section, 150-250°C, chemisorbed water and additives or volatile decomposition products are recognized. In the third section, compounds begin to decompose above 250°C, between the inflection points of the TG curve (T_{onset} and T_{endset}). In the fourth section, non-volatile inorganic ashes and metals remain. In oxidizing environment metals are oxidized and gain mass in section five. [69]

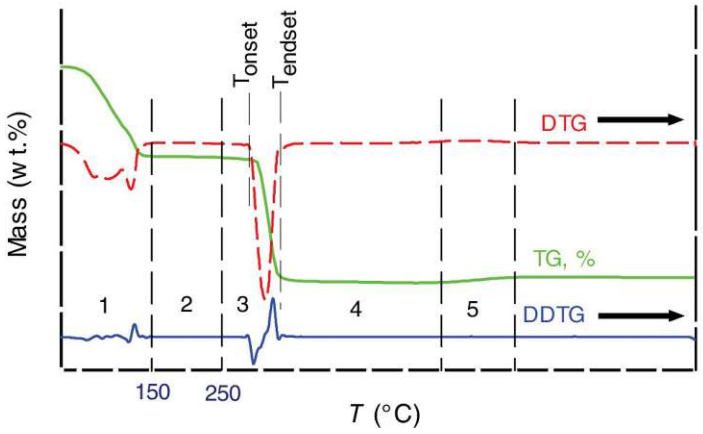

Figure 10: Thermogram (TG curve in green, DTG curve: first derivative in red, DDTG: second derivative in blue) of $Mn(CH_3CO_2)_2.4H_2O$ heated up to 900°C in air[69]

In general, there are different types of TGA-setups and the heating/cooling system is always parallel to the gas flow stream. Some are loaded from the top, so the balance is at the bottom and the sample pan is connected via a stem support rod. The gas is purged from the bottom to the top. Another type is loaded from the side, so the balance is connected to a horizontal sample support. The third type is loaded from the bottom, because the sample is hanging

down from the balance. In all types, radiant shields are installed near the balance to decrease fluctuations and prevents noise in the mass signal. [69]
For standard TGA measurements commercially available analysers, like TG 209 F3 Tarsus (NETZSCH) or TGA Thermostep (ELTRA) are used. These setups are compact and can be handled fully automatic. In Figure 11 on the left a typical TGA setup by NETZSCH is shown. Here the sample is placed on the sample pan, which is connected via a stem support rod and surrounding radiation shields to the microbalance. The weighing chamber is flushed by a protective gas to avoid damages by the used gases. The furnace allows temperatures from room temperature to 1000°C.
Furthermore, carousel sample systems are used, see Figure 11 on the right side. Here 19 crucibles and one reference crucible allow standard measurements. Analysis of coal, which is described in ASTM Norm D7582, gives information of the moisture, ash and volatiles content in the samples. The analysis of cement typically show the moisture and loss on ignition(LOI), and for other chemicals it is often used to determine the decomposition at different temperatures.[70], [71]

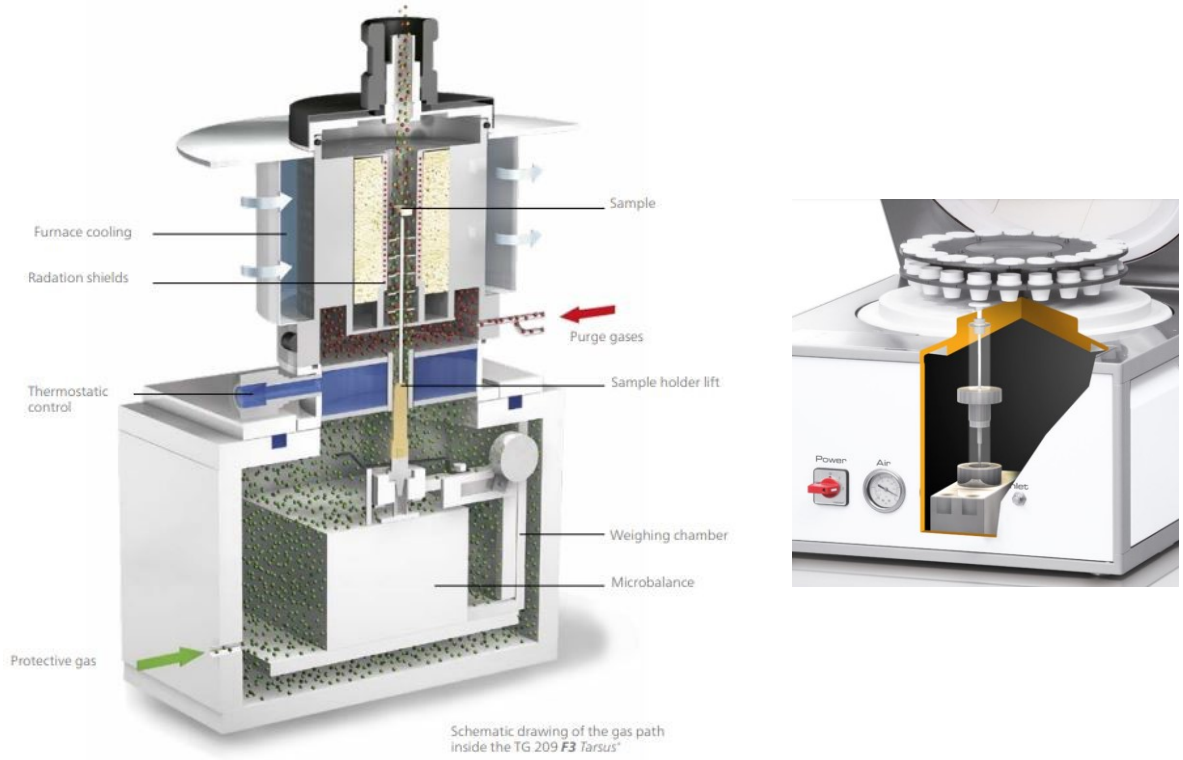

Figure 11: Schematic setup of a commercial TGA
(left: NETZSCH TG 209 F3 Tarsus[70], right: ELTRA TGA Thermostep[71])

More advanced instruments are already used. The fluidized bed TGA setup includes a quartz reactor and an electrical furnace and helps to monitor the reaction additionally to the standard techniques like for the product gases gas chromatography - mass spectroscopy – Fourier transformation infrared spectroscopy (GC-MS-FTIR). Alternative heating systems like induction heating or microwave furnace are also available.[69]

2.4.2. Laser-induced Breakdown Spectroscopy

Laser-induced breakdown spectroscopy (LIBS) is the combination of laser ablation for creation of a plasma plume and a detection system for recognizing the emitted radiation. The laser is focussed by lenses, the sample is ablated, atomized, and forms a plasma. The plasma includes ions, free electrons, atoms and molecules. The high temperature excites electrons of the atoms and during relaxation to the ground state characteristic elemental lines are emitted. The emission is detected by a spectrometer and a detection system. A moveable sample stage makes spatially resolved measurements possible. For selection of the ablation region a microscope is integrated. The constitution of the samples is monitored by simultaneous qualitative and quantitative analysis of almost all elements with detection limits ranging from µg/g to mg/g, depending on the element. For quantification standards are needed, because the ablation step include matrix effects and the interaction with the sample is material dependent resulting in distinct variations on atomisation and excitation efficiency. [35], [72]

In comparison to other techniques, LIBS measurements can be applied to solid, liquid and gaseous samples and every element of the periodic system can be analysed. Furthermore, measurements at any atmosphere are possible. For solid samples often no preparation and no dilution is necessary. By analysing multiple elements simultaneously within few seconds, it is an important qualitative and quantitative tool with a working range of trace elements of µg/g and main components of ‰ levels. Other techniques like LA-ICP-MS show a lower limit of detection (LOD) of some ng/g for some elements, but detection of hydrogen is not possible. The ablation of the sample allows depth profiling and a high spatial resolution. A main disadvantage are matrix effects, that's why often laser spots are replaced by bigger laser patterns and standards should include the same components as the sample. Matrix effects show a large influence of small inhomogeneity. This is a big problem for the solid state standard preparation for quantification and is often connected with a more time-consuming optimization of the standard preparation.[72]–[74]

The mechanism of laser ablation includes the absorption of the focused laser beam, heating, melting and the vaporization of the sample. In comparison to gases, solid samples show a quick transformation of most of the excitation into heat, because of the lattice via phonon vibration. Laser ablation is a widely used technique for a controlled way to create an aerosol directly from the solid sample. No additional sample preparation is required, for example dissolution can be avoided. The solvent can introduce impurities and especially for ceramics it is sometimes difficult to bring the sample into liquid phase. Pulsed laser in the nanosecond and femtosecond range are used. Femtosecond lasers create well-defined craters and better ablative reproducibility, because of less heat dissipation, but atomisation and excitation are less efficient and femtosecond lasers are more expensive. Furthermore, the laser pulse is already ceased when the plasma is created and therefore no plasma shielding appears, see Figure 13. Plasma shielding causes that some of the laser energy is not transferred to the sample. [35], [72], [73]

If the required laser irradiance generates enough free electrons ionization processes generate a plasma, which expands while emitting light. The vaporized sample is flushed by a gas stream of a noble gas, helium or argon. Thus, in addition to spectral analysis of the plasma emission by LIBS, this also opens the possibility to analyse the aerosol by ICP-MS, ICP-OES or other analytical techniques. [35], [73]

Important laser properties are its wavelength, irradiance, pulse energy and pulse width. Shorter wavelengths show a higher ablation efficiency and less fractionation. [75]–[77]

In literature different lasers, Ti:Sapphire, excimer for the UV region and Nd:YAG laser for near IR, visible and UV regions, are used. In our setup a Nd:YAG laser is used. These lasers are made up of a single crystal yttrium-aluminium-garnet doped with Neodymium and by a Q-switch the laser is pulsed. The fundamental wavelength of 1064 nm is quartered to 266 nm or divided by five to 213 nm by second-harmonic generation. In general, compact diode pumped Q-switched Nd:YAG lasers have high beam quality, a repetition rate of 10-30 Hz with an energy per pulse of a few 100 mJ and pulse width of few nanoseconds. Like already mentioned, the pulse width is an important property of a laser. Femtosecond lasers show a more controlled process of laser ablation, which leads to clean craters, in comparison to nanosecond lasers. The very short pulses create mostly atomic emission, and the plume is close to stochiometric sample evaporation. The lack of portability and high costs limit the usage of femtosecond lasers. [72]

The setup of the LIBS system used in this study is visualized in Figure 12.

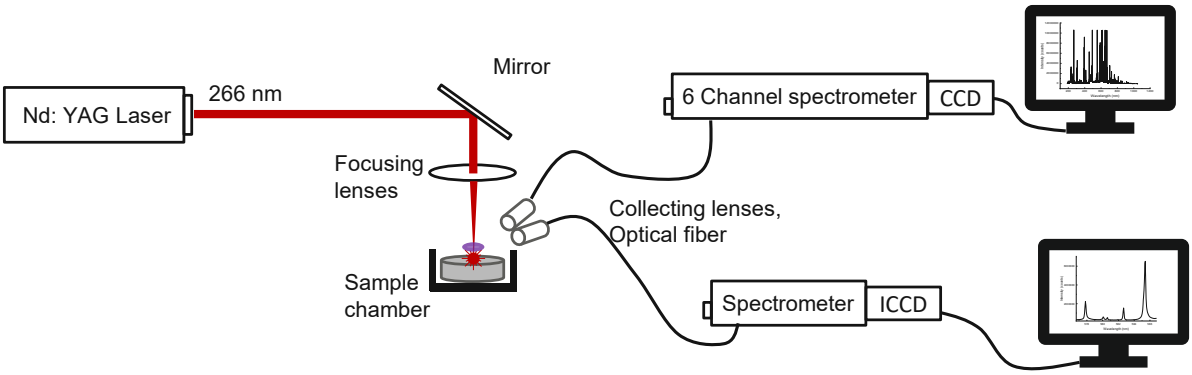

Figure 12: Schematic setup of the used Laser-induced breakdown spectroscopy

The temporal course of the emission signals of a typical LIBS measurement are schematically illustrated in Figure 13. The emission spectrum can include ionic emissions, which are in the beginning, followed by atomic emissions and molecular emissions. Furthermore, a background continuum is caused by Bremsstrahlung. For each measurement the time frame should be optimized to get the best signal to noise ratio by changing the “Gate Delay”, “Gate Width” and “Intensifier Gain”. The Gate Delay is the time between the start of the laser pulse and the beginning of data collection. The Gate Width defines how long the detector collects data and the intensifier gain is the opportunity to intensify the signal to take advantage of the whole dynamic range. [78]

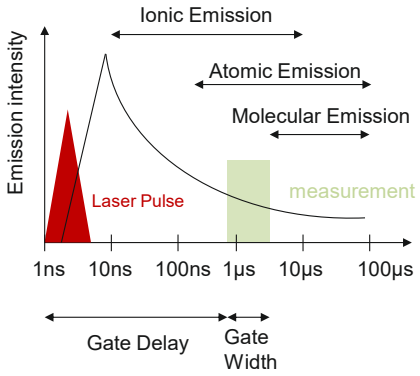

Figure 13: Optimization of time frame for LIBS measurement (ionic, atomic and molecular emission), adopted from [78]

The optical system includes collecting lenses, optical fibers and the spectrometer. Often Czerny-Tuner, like in the setup we used, or Echelle monochromators are connected to the detectors. Detectors like photomultiplier tubes (PMT), photodiode array (PDA), charged coupled devices (CCD), intensified charge coupled devices (ICCD) are used. Like the name CCD indicate, the information is represented by a packet of electrons. The CCD generates charge, collects and transfers it on a metal insulator semiconductor and detect at so called gates. It is the most sensitive multichannel detector and ICCD are for time-domain measurements, but also to enhance the signal intensity. In the used system a broadband spectrum is recorded by using the Czerny-Turner six channel spectrometer and CCD detectors, and a detailed spectral region by the ICCD detector with a separate high resolution Czerny-Turner spectrometer. [72]
LIBS systems can be applied everywhere, even on Mars. The Curiosity rover explored the surface of the planet Mars using an integrated LIBS equipment since August 2012. This encouraged scientists to build LIBS systems dedicated to operate in harsh environments. Furthermore, insitu LIBS measurements become more important. [77]
Even for applications in nuclear fusion technology LIBS can be used as an insitu measurement, like Cong Li et al.[79] showed in their review. In contrast to TGA, LIBS is not an absolute method, thus measured signal intensities must be converted into amounts of concentrations.

The simplest quantification approach is univariate calibration, to plot single line intensity against standard concentration. Some corrections can be done by baseline correction, normalization of a surrounding line for correction of laser variations. Motto-Ros et al. reported, that sometimes it is better to create the calibration curve by using the highest intensity of the emission peak and sometimes the area of the emission peak[74]. Big differences for the calibration appear for broad emission lines, e.g. emission lines of hydrogen. Besides univariate calibration, more advanced calibration techniques like partial least squares (PLS), artificial neural network (ANN), support vector machine (SVM) or multilinear regression (MLR) are used. A big problem of multivariate quantitative analyses is the high risk of overfitting. Furthermore, calibration free LIBS (CF-LIBS), where mathematical models of the plasma are used to determine the species concentration, is used. For CF-LIBS the stochiometric laser ablation from the sample, the reabsorption effects should be negligible and the local thermal equilibrium requires an electron density $N_e \geq 1.6\ 10^{12}\ T^{0.5}\Delta E^3$, where T is the plasma temperature and ΔE is the largest energy transition. [74], [80]–[83]

Certified reference materials (CRM) or in-house prepared standards can be used for signal quantification. Usually, compact standards are prepared by one of the approaches described in the paragraph below. Internal standards can be used to correct differences in ablation, transport, and ionization efficiencies. Very specific CRMs are available, like apple leaves in NIST SRM 1515, non-fat milk powder in NIST SRM 1549 or trace elements in spinach leaves in NIST SRM 1570a. If no CRM is available, in-house standards have to be prepared. Quantification strategies can be further improved by using concepts of single standard addition, multiple standard additions, or isotope dilution. [84]

A main problem of all direct solid state sampling techniques like LIBS, is the quantification. Matrix effects do affect the results and therefore matrix-matched standards need to be prepared, which is often not easy or commercially not available. The preparation of compact samples or standards requires homogenous powders, which have to be milled, grinded and/or sieved. Then there are different possibilities to form a compact sample, like pelletization, fusion to sample disks, mounting or embedding in a polymeric resin. For pelletization a hydraulic

press is used and often a binder is added to improve powder grain adhesion to produce stable pellets. Additives like for standard addition or isotope dilution purposes can be added. Homogeneity can be increased by milling/grounding the components before mixing, but in some cases the inhomogeneity restricts the reproducibility. The pressing step is optimized by varying the press power and the pressing time. In conclusion the pelletization is an easy approach without high-tech equipment.

The second approach, fusion, needs a molten flux which is realised by melting lithium tetraborate or lithium metaborate or a mixture of it at temperatures above 1000°C. The powder and additives (like for quantification or internal standards) are added and after cooling very homogenous fusion disks are obtained. The better homogeneity in comparison to the pelletization is a big advantage of the fusion technique. A big disadvantage is the need of the high temperature and combined with possible losses of analytes having low boiling points or other volatile substances. The flux substances contain Li and B and therefore those elements have to be analysed by using other techniques.

Mounting the powder on adhesive surfaces, like sticky tapes or not completely dried epoxy resin is often used for qualitative and semiquantitative analysis. The adhesiveness is a limiting factor. While ablating with the laser, the surrounding powder particle should retain and should not be damaged. Another opportunity is to completely embed in epoxy resin. Those two approaches show the big advantage to analyse single powder particles instead of analysing the mean composition of a number of particles. The varying composition of the single particles can be analysed, because ideally only one particle is ablated by the laser.[84]

3. Experimental part

3.1. List of chemicals

All materials used for the Laser Induced Breakdown Spectroscopy, Thermogravimetric Analysis and EX-SITU experiments were obtained from commercial suppliers, except the y-doped barium zirconate disks and precursor powder. The following Table 3 contains information of the origin and purity of the used chemicals.

Table 3: Information of the used chemicals.

Chemical formula	Name	CAS	Purity	Company	Notes
ZrO_2	Zirconium (IV) oxide	1314-23-4	99+ %	Alfa	Powder
$Zr(OH)_4$	Zirconium (IV) hydroxide	14475-63-9	97 %	Sigma-Aldrich	Powder
$Ba(OH)_2$	Barium hydroxide	17194-00-2	99.9 %	Sigma-Aldrich	Powder
$BaZr_{0.85}Y_{0.15}O_3$	BZY15 disk sample	-	-	NorECs – Norwegian Electro Ceramics AS	~18-20 mm diameter, ~1-2 mm thickness
$BaZr_{0.8}Ce_{0.1}Y_{0.1}O_3$ + 1 wt.% NiO	BZCY81-Ni disk sample	-	-	NorECs – Norwegian Electro Ceramics AS	~18-20 mm diameter, ~1-2 mm thickness
8YSZ, $BaCO_3$, NiO	BZY15 Precursor powder mixture	-	-	NorECs – Norwegian Electro Ceramics AS	Mixed in isopropanol for 24 h, dried at 150 °C, sieved through 150 µm mesh
$N_3O_9Y{\cdot}6H_2O$	Yttrium (III) nitrate hexahydrate	13494-98-9	99.8 %	Sigma-Aldrich	-
$ZrO(NO_3)_2{\cdot}xH_2O$	Zirconium dinitrate oxide hydrate	14985-18-3	99.9 %	Alfa Aesar	-
$Ba(NO_3)_2$	Barium nitrate	10022-31-8	99.9 %	Sigma-Aldrich	-
HCl	Hydrochloric acid fuming 37 %	7647-01-0	p.a.	Merck KGaA	-
HNO_3	Nitric acid 65 %	7697-37-2	p.a.	Merck KGaA	-
$HClO_4$	Perchloric acid 70 %	7601-90-3	p.a.	AppliChem	-
Ar	Argon	7440-37-1	99.999 %	Messer	-
H_2	Hydrogen	1333-74-0	99.999 %	Messer	-

3.2. Sample preparation and characterization

Samples, listed in the upper part of Table 4, were prepared by the company NorECs – Norwegian Electro Ceramics AS.

Table 4: List of all samples.

Sample name	Compound	Measurements	Note
BZCY81-TGA1	$BaZr_{0.8}Ce_{0.1}Y_{0.1}O_3$ + 1 wt% NiO	1.-6.TGA	-
BZY15-Powder	$BaZr_{0.85}Y_{0.15}O_3$	7.-8.TGA	green
BZY15-TGA2	$BaZr_{0.85}Y_{0.15}O_3$	9.TGA	green, colour change and cracked
BZCY81-TGA3	$BaZr_{0.8}Ce_{0.1}Y_{0.1}O_3$ + 1 wt% NiO	10.-16.TGA	-
BZY15-pieces	$BaZr_{0.85}Y_{0.15}O_3$	4.-11.EX-SITU, 17TGA	self-synthesized powder and pressed/sintered, only 11 mol% Y
BZY15 Pellet 1	$BaZr_{0.85}Y_{0.15}O_3$	12.EX-SITU	cut in A, B, C, D
BZY15-A	$BaZr_{0.85}Y_{0.15}O_3$	20.EX-SITU	-
BZY15-B	$BaZr_{0.85}Y_{0.15}O_3$	13.EX-SITU, 22.TGA	-
BZY15-C	$BaZr_{0.85}Y_{0.15}O_3$	18.TGA, 14.-18.EX-SITU	-
BZY15-D	$BaZr_{0.85}Y_{0.15}O_3$	19.EX-SITU	broke a piece for ICP-OES
BZY15-Da	$BaZr_{0.85}Y_{0.15}O_3$	19.-21.TGA	Rest of BZY15-D
BZY15 Pellet 2	$BaZr_{0.85}Y_{0.15}O_3$	22.EX-SITU	-
BZY15 Pellet 2 piece	$BaZr_{0.85}Y_{0.15}O_3$	23.EXSITU	piece of BZY15-Pellet 2
In-house sintered Pellet 1	$BaZr_{0.85}Y_{0.15}O_{2.925}$ + 1 wt% NiO	26.-27.TGA, 29.-31.TGA	-
In-house sintered Pellet 2	$BaZr_{0.85}Y_{0.15}O_{2.925}$ + 1 wt% NiO	24.EX-SITU	-
In-house sintered Pellet 3	$BaZr_{0.85}Y_{0.15}O_{2.925}$ + 1 wt% NiO	25.EX-SITU, 33.TGA	-
In-house sintered Pellet 4	$BaZr_{0.85}Y_{0.15}O_{2.925}$ + 1 wt% NiO	26.EX-SITU, 32.TGA	Grinded for powder TGA measurement
In-house sintered Pellet 5	$BaZr_{0.85}Y_{0.15}O_{2.925}$ + 1 wt% NiO	32.TGA	Grinded for powder TGA measurement

These samples were used for optimization and for first measurements. The BZY15 powder was prepared by grinding in a mortar and in a mixer mill (Retsch MM400, 2011).
BZY15 was synthesized by hydrothermal process and the educts are listed in the middle of Table 3. Therefore, zirconium nitrate was dissolved in ultrapure water, acidified with nitric acid and the concentration determined by ICP-MS measurement. All educts were dissolved in double-distilled water and 2 N NaOH added. For the precipitation of barium as an hydroxide, the solution needs to be strongly alkaline. Without mixing, all reagents were filled in a Teflon tank and put inside the autoclave (highpreactor, Berghof, Germany). The gas phase was flushed by argon and stirred at 250 rpm. The temperature was controlled by a temperature controller BTC-3000.
The temperature program is shown in Table 5.

Table 5: Temperature profile for synthesis of BZY15.

Heating rate	Holding time	Temperature
25°C/min.	61 min.	62°C
180°C/min.	335 min.	201°C
155°C/min.	13 min.	30°C
2°C/min.	1 min.	30°C

The white powder was centrifugated, washed with water and dried in a compartment drier. This powder was monoaxially pressed with 10 kN and the load was removed slowly. This pellet was sintered in a tube furnace (Carbolite, Germany) at 1500°C for 4 h and with a heating/cooling rate of 5°C/min. This pellet was broken to smaller pieces of about 0.3 cm length.

The BZY15 Pellet 1 was measured ex-situ and cut by a precision cutter (Struers MINITOM, Denmark) in four quarters (A, B, C and D). For ICP-OES measurement a piece of the sample BZY15-D was taken, and the rest of the sample is called BZY15-Da. The ICP-OES measurement is described in part 3.3.2. Furthermore, the sample BZY15 Pellet 2 was first measured ex-situ in humidified argon and secondly a part of the pellet was broken apart and measured ex-situ in dry argon again.

In-house sintered BZY15 pellet 4 and 5 were grinded in an agate mortar and a planetary micro mill (FRITSCH pulverisette, type: 07.302, Germany) for 30 min. The powder was sieved by a sieve tower and powder fractions smaller than 180 µm were used for the humidification in the TGA system. This was done to ensure short diffusion lengths in the water uptake/release experiments monitored by TGA.

Lastly some Precursor powder mixture was bought from the same company and pellets of about 1 g were prepared by their recipe, see Table 6. Therefore, a uniaxial press and a high temperature tube furnace (Carbolite, Germany) were used.

Table 6: Recipe for in-house sintered BZY15 pellet preparation.

Pressing load	20 kN.
Pressing duration	1 min., slow load removal
Heating rate	5°C/min.
Sintering temperature	1500°C
Sintering duration	12 h
Cooling rate	5°C/min.

An overview picture of all samples is shown in Figure 14.

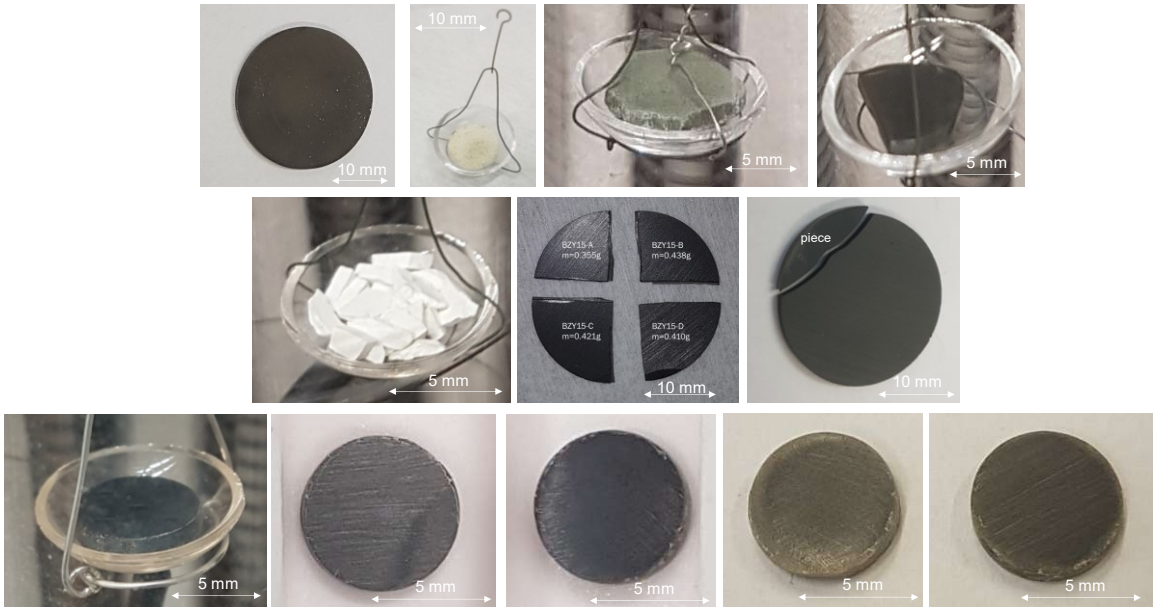

Figure 14: Images of all samples
(First row: BZCY81-TGA1, BZY15-Powder, BZY15-TGA2, BZCY81-TGA3
second row: BZY15 pieces, BZY15 Pellet 1, BZY15 Pellet 2
third row: In-house sintered BZY15 Pellet 1, 2, 3, 4 and 5)

For the diffusion profile measurement, a BZY15 Pellet was dried at 900°C under Argon flow and humidified ex-situ for 90 seconds at 550°C. Three pieces were cut by a precision cutter (Struers MINITOM, Denmark) and LIBS measurements were performed on the cross-section by line scans parallel to the surface.

3.3. Instrumentation

3.3.1. XRD measurements for characterization and quality control

The XRD measurements of the used materials show the purity and possible changes after water incorporation. Especially the XRD diffractograms before and after sintering of the in-house sintered BZY15 pellets were important to see whether the required phase formed. It was important to have the same structure of the perovskite, so the experiments can be compared.
XRD measurements were performed using an Empyrean diffractometer (Malvern Panalytical, Germany) with a focus width of 0.4 mm, equipped with a Bragg-Brentano HDCu x-ray mirror and a X'Celerator detector. Cu Kα radiation (45 kV, 40 mA) and a 2θ range from 5° to 120° was used. All scans were done with a measuring time of 15 minutes per sample and the obtained diffractograms were analysed using Panalytical Highscore. A Rietveld refinement allowed the prediction of crystallite size of the material.
The sample preparation for XRD measurements for pellets and powders were different. Pellets were positioned on plasticine coated with parafilm, powders were homogenized in an agate mortar and fixed on Vaseline or suspended in ethanol, if the powder was needed afterwards.

3.3.2. Liquid measurements for composition analysis

For characterization of the proton-conducting materials ICP-OES measurements on an iCAP 6500 RAD (Thermo Fisher Scientific, USA) were done and 0.1 g of each material (BZCY81, BZY15, BZY15 pieces and a piece of BZY15-D) was dissolved in 3 mL perchloric acid and 7 mL ultrapure water. Ultrapure Water was produced by a Barnstead™ Easypure™ II (Thermoscientific™, USA). The quality exceeds the quantitative specifications of Type 1 water as described in ASTM™ D1193, ISO 3696 and CLSI-CLRW. Dilutions of 1:100, 1:1000 and 1:10000 with 1 % HNO_3 and Europium as internal standard were introduced with an ASX-520 autosampler (CETAC Technologies, USA) and a Miramist nebulizer (Thermo Fisher Scientific, USA), a PTFE spray chamber and a ceramic injector tube torch. The used ICP-OES parameters are listed in Table 7.

Table 7: ICP-OES parameters.

RF-Power	1300 W
Radial observation height	14 mm
Cooling gas flow	12 L/min
Nebulizer gas flow	0.65 L/min
Auxiliary gas flow	0.4 L/min
Integration time per replicate	8 s
Replicates per sample	3
Purge pump flow rate	1.6 mL/min
Analysis pump flow rate	0.8 mL/min

To determine possible contaminants, an ICP-MS survey scan was done at a Thermo iCAP Q with an ASX-520 autosampler (CETAC Technologies, USA). Quantification in the MS was not possible, because the concentration was too high and a further dilution would have resulted in a bigger error, that's why the quantification was done by ICP-OES measurements. For the detected elements, five multielement-standard solutions (0.1 µg/g, 2.5 µg/g, 5.0 µg/g, 7.5 µg/g, 10.0 µg/g) with an internal standard of 1 µg/g Europium were diluted from a stock solution. The used standard solutions are listed in Table 15 in the Appendix.
Three measurements of each sample dilution, split by blank measurements were done. The used quantifier and quality control lines for the ICP-OES measurement are noted in Table 8.

Table 8: ICP-OES measured lines per element.

Element	Quantifier line (nm)	Quality control line (nm)
Ba	233.527	230.424
Ce	456.236	404.076
Cr	359.349	283.563
Hf	282.022	263.871
Ni	352.454	221.647
Y	377.433	360.073
Zr	339.198	343.823

For the calculation of the molar quantity of each element, all main cations were set to 2 and oxygen without determination to 3 in the chemical formula of $BaZrYO_3$ or $BaZrCeYO_3$. E.g., the determination for barium in BZY:

$$n(Ba) = \frac{c(Ba)}{c(Ba) + c(Y) + c(Zr)} \cdot 2 \quad \textbf{(19)}$$

Here the concentrations c are calculated by the emissions of the prepared standards and of the sample solutions.
The further determined elements are calculated by division of the concentration c of the element and the concentration of barium c(Ba), multiplied by the calculated molar quantity of barium n(Ba). Here the molar quantity of the sinter additive Ni is calculated:

$$n(Ni) = \frac{c(Ni)}{c(Ba)} \cdot n(Ba) \quad \textbf{(20)}$$

For each measurement the calculations were done, and the mean value is presented in chapter 4.1.

3.4. TGA measurements for water incorporation

The TGA setup used an inhouse-built instrument and the development of humidification experiments are interesting for characterization of proton conductors.

The final thermogravimetric analysis setup included the following parts and are summarized in Table 9.

Table 9: Thermogravimetric analysis setup.

CI Precision microbalance with a controller unit
Thermocouple (Type K)
Radiant shield made of quartz glass
Counterweight and sample mounting
Furnace with a maximum temperature of 1200°C
Circulation pump for cooling
Two air coolers
0.25 Torr and 100 Torr pressure load cells
toggle locking unit
turbomolecular pump and backing pump
mass flow controller
humidification unit (riser pipe, filled with distilled water)
magnetic and mechanic valves
relief valve and a gas bubbler

The balance operates by an electronic bridge circuit, that helps the servo system to balance the weight and counterweight. This enables a very precise and exact signal generation. The principle of the balance operation is the following: A lamp and two photocells recognize the position of the balance arm and a small displacement causes excess current flow in one photocell. This causes a bridge current and this current passing through the movement coil rapidly counteracts the external torque applied to the balance arm. The weight-proportional current is registered and represent the information of the weight.

An overview of all TGA experiments is shown in Table 16 in the Appendix.

3.4.1. TGA data processing

Weight and temperature data were recorded every 6 s and this data was further processed using two different methods, i.e., rolling mean and the Sawitzky Golay method. Sawitzky Golay uses a polynom-smoothing in a defined moving window and results in a weighted summation of the surrounding data. The rolling mean calculates the mean in a defined moving window. Moreover, the number of data points in the moving window used for the smoothing method was varied, see Figure 15.

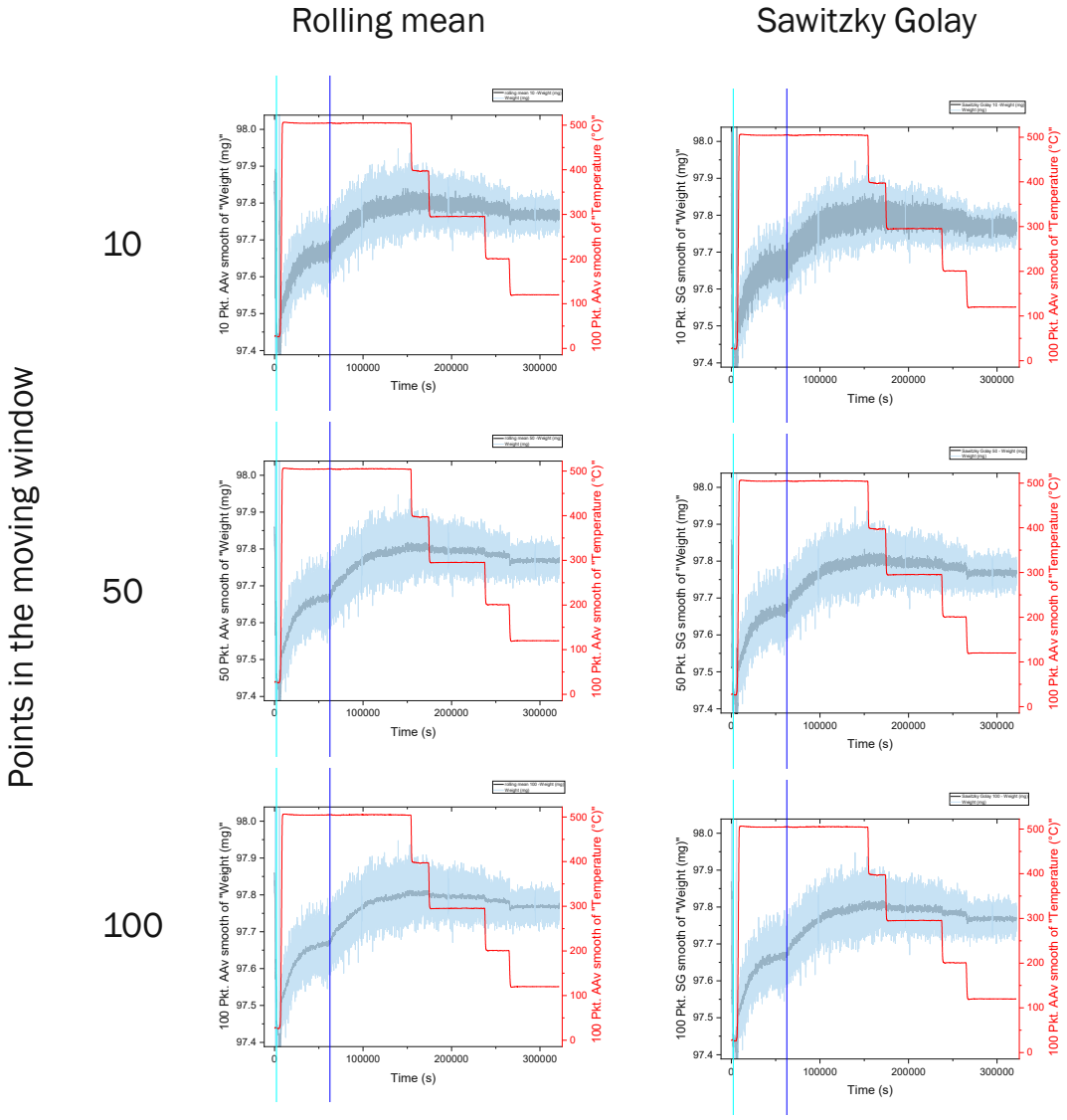

Figure 15: TGA data processing – smoothing methods (first row: 10 points in the moving window and rolling mean, Sawitzky Golay; second row: 50 points in the moving window and rolling mean, Sawitzky Golay; third row: 100 points in the moving window and rolling mean, Sawitzky Golay)

In general, by increasing the points in the moving windows the smoothing effect is increased. If the number is too low, the smoothing of the data is not good enough and noise can be misinterpreted as occurring weight changes. On the other hand, a too high number for smoothing leads to over smoothed data and little weight changes are not recognisable anymore.

For the measurements of this work, the rolling mean smoothing with 100 points in the moving window turned out to be appropriate.

In the section 4 “Results and Discussion”, thermogravimetric analysis figures include the smoothed data and error bars. The error bars were calculated by the standard deviation in sections of about 2 h, that means for example the error bar is shown at the x-axis at 1 h and represents the standard deviation of the original data of about two hours.

3.4.2. Ex-situ measurements for validation

A setup to simulate a TGA measurement was used to validate the TGA apparatus and performance. Furthermore, ex-situ measurements allowed to hydrate more than one sample at the same time and due to the simple setup measurements were less time-consuming. A furnace (Carbolite GERO, Germany) with an operating range of 30-1000°C, a furnace controller, two air cooler, a glass tube that is flushed by argon, a thermocouple (type K) to measure the temperature of the glass tube near the sample and a riser pipe which contains water for the humidification of argon was used.

3.5. LIBS measurements for hydrogen quantification

A J200 Tandem (Applied Spectra, USA) with a 266 nm nanosecond Quantel Ultra Nd-YAG laser (Quantel, USA) and two different collection optics were used for the LIBS measurements. One optical system includes six Czerny-Turner charge coupled-device (CCD) spectrometers, each 2048 pixels and covering together a spectral range of 187.6 nm to 1047.7 nm. The other collection optic is made up of a high resolution Czerny-Turner spectrometer and an intensifier charge-couples device to represent a focused part of the spectrum. A moveable sample chamber and an integrated microscope made it possible to focus a sample spot of 60 µm to 200 µm and place laser patterns. The laser was pulsed with a frequency up to 10 Hz and a pulse energy which can be adapted by a attenuator. The parameters are summarized in Table 10. The values in the brackets are conditions, which were only used in some cases.

Table 10: LIBS parameters for hydrogen quantification.

Laser Energy	90 % = 3 mJ			
Laser Pattern	X = 1.5 mm (3 mm), Y = 0.5 mm			
Gate Delay (CCD)	0.1 µs			
Stage Speed	0.5 mm s^{-1} (2 mm s^{-1})			
Spot Size	100 µm (80 µm)			
Repetition Frequency	10 Hz			
Measurement Atmosphere	Helium			
Gas Flow	2 L min^{-1}			
ICCD	Condition A	Condition B	Condition C	Condition D
Gate Delay	0.2 µs	0.2 µs	0.7 µs	1 µs
Gate Width	0.2 µs	0.5 µs	5 µs	2 µs
Intensifier Gain	10x	10x	20x	30x
Blaze	500 nm			
Possible Interferences	Wavelength (nm)			
Ba	659.53 (I)			
Ce	655.17 (I), 655.57 (I), 657.91 (I), 660.64 (I)			
H	656.27 (I), 656.28 (I), 656.29 (I)			
He	667.82 (I), 706.5190 (I)			
Ni	664.36 (I)			
Y	653.86 (I), 661.38 (II)			
Zr (all not intense)	650.33 (I), 650.64 (I), 655.05 (I), 656.94 (I), 657.66 (I), 659.20 (I), 659.67 (I), 659.88 (I), 660.33 (I), 662.06 (I)			

The laser pattern is illustrated in Figure 16. Furthermore, four different ICCD settings were used to optimize hydrogen quantification.

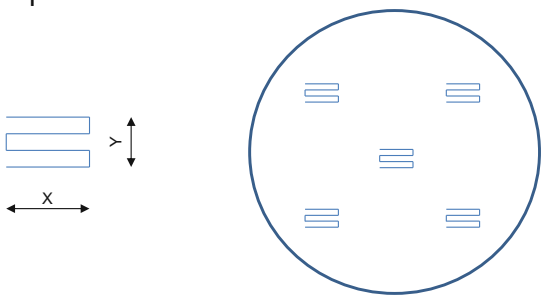

Figure 16: Laser pattern for LIBS measurements on matrix matched standards for hydrogen quantification

3.5.1. LIBS standards preparation

For quantification of hydrogen, solid standards had to be prepared, because no commercially available solid hydrogen standards were available. An overview of all prepared standards is shown in Table 11.

Table 11: List and preparation details of LIBS standards.

Material B	Standards	Mixing	Pressure load
ZrO_2	5 standards (0.24-1.21 wt-%), $Zr(OH)_4$, ZrO_2	agate mortar	50 kN, 10 sec.
ZrO_2	5 standards (0.07-0.35 wt-%)	ball mill	50 kN, 10 sec.
BZY15	5 standards (0.05-0.61 wt-%), BZY15pressed	agate mortar	60 kN, 20 sec.
BZCY81	5 standards (0.04-0.61 wt-%), BZCY81pressed	agate mortar	60 kN, 30 sec.
BZY15*	5 standards (0.04-0.62 wt-%), BZY15pressed	agate mortar	60 kN, 1 min.
BZY15*	5 standards (0.04-0.62 wt-%), BZY15pressed	ball mill	60 kN, 1 min.

*…sintered Precursor powder

The schematic of the preparation in Figure 17 shows, that a material B is grinded in a ball mill at 20 Hz and four minutes (Retsch MM400, steel tank 10 mL and steel balls Ø12 mm, Germany), dried and mixed with zirconium hydroxide - as a material with a defined hydrogen content - in a mortar. These mixtures were pressed monoaxially.
For proof of concept the first standards were prepared by mixing $Zr(OH)_4/ZrO_2$. To minimize different matrix effects the perovskite pellet was grinded. In the end, the bought and sintered BZY15 precursor powder were used, so it is comparable to the in-house sintered BZY15 pellets.

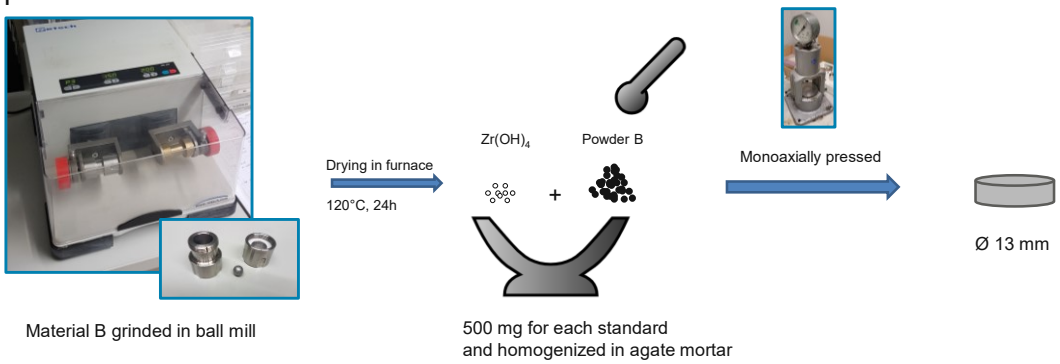

Figure 17: Schematic of the LIBS standard preparation

3.5.2. LIBS evaluation

The hydrogen emission at 656 nm area was normalized by the area of barium at 659 nm for each measurement. The areas were determined by integration with a python (v 3.7.6, https://www.python.org) code using a defined start and end wavelength. These integration window should include the emission peak and some data points of the surrounding. Furthermore, the background was generated automatically from the surrounding pixels by a linear curve. The integration tool subtracts the area under the background line from the area under the emission peak and therefore only the hydrogen emission is represented by the area.

The concentration for each standard was calculated with the amount of zirconium hydroxide and the used material B, as illustrated in Figure 17.
For each standard a mean value and standard deviation is calculated to form a calibration curve.

3.5.3. Hydrogen diffusion profile

The pellet “BZY15 Pellet 2” was dried under Argon and at 900°C in an ex-situ experiment for 5 h. The humidification was done for 90 s, but here it has to be mentioned that the gas exchange from dry to fully humidified argon needs some time. Three different pieces were cut by a precision cutter (Struers MINITOM, Denmark), as illustrated in Figure 18. LIBS measurements determined the hydrogen content on the cut surface, which was polished by P1000 and dry cleaned. The laser pattern of lines parallel to the surface of the pellet allowed to get information of the hydrogen diffusion.

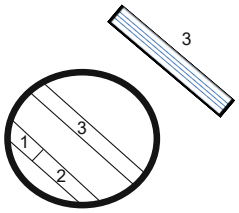

Figure 18: Schematic sample preparation
(1, 2 and 3 represent sample pieces obtained by cutting the disk-shaped pellet and each cross section was measured by aligned LIBS lines)

4. Results and Discussion

In the following section the main results of the Laser Induced Breakdown Spectroscopy and Thermogravimetric Analysis are discussed.

4.1. Material composition

The used barium yttrium zirconate pellets, barium cerium yttrium zirconate pellets and self-made barium yttrium zirconate powder were analysed by ICP-OES to evaluate the purity and amount of dopant. In Table 12 the expected and the determined compositions are compared. The uncertainty for all elements were less than 0.002 mol, calculated by the mean of three measurements.

Table 12: Composition of used Y/Ce-doped barium zirconate

	Expected Composition	By ICP-OES determined composition
BZY15	$BaZr_{0.85}Y_{0.15}O_3$ + 1w% NiO	$Ba_{1.002}Zr_{0.837}Y_{0.161}O_3$ (0.011 mol Hf, 0.030 mol Ni, 0.001 mol Cr, 0.004 mol Ce)
BZCY81	$BaZr_{0.8}Ce_{0.1}Y_{0.1}O_3$ + 1w% NiO	$Ba_{1.014}Zr_{0.830}Ce_{0.050}Y_{0.105}O_3$ (0.011 mol Hf, 0.044 mol Ni, 0.001 mol Cr)
BZY15 (green)	$BaZr_{0.85}Y_{0.15}O_3$	$Ba_{1.018}Zr_{0.826}Y_{0.157}O_3$ (0.010 mol Hf, 0.001 mol Ni, 0.001 mol Cr, 0.001 mol Ce)
BZY-powder	$BaZr_{0.85}Y_{0.15}O_3$	$Ba_{1.014}Zr_{0.875}Y_{0.111}O_3$ (0.010 mol Hf, 0.001 mol Ni, 0.001 mol Cr, 0.001 mol Ce)

The BZY15 pellets show a little higher concentration of yttrium, but in general the measured values are sufficiently close to the expected composition. The determined concentration of cerium in Ce and Y-doped barium zirconate is less than expected. The self-synthesized powder shows a significantly lower concentration of yttrium that is most likely related to peculiarities of the synthesis route of the barium zirconate. Furthermore, hafnium was determined in small concentration, which was expected because zirconium is always found in combination with hafnium[85]. Some Ni and Cr were determined as well, but only for BZY15 and BZCY81 with NiO added to improve the sintering behaviour, the amount Ni is notable.

4.1.1. Y- and Ce-doped barium zirconate BZCY81

The first water incorporation measurements were done with Y- and Ce-doped barium zirconate. The diffractogram in Figure 19 recorded before humidification shows four different phases, barium yttrium zirconium oxide, yttrium zirconium oxide, barium cerium yttrium zirconium oxide and cerium zirconium oxide. Rietveld refinement allowed a quantitative suggestion of about 98.7% barium zirconium oxide and 1.3% cerium zirconium oxide.

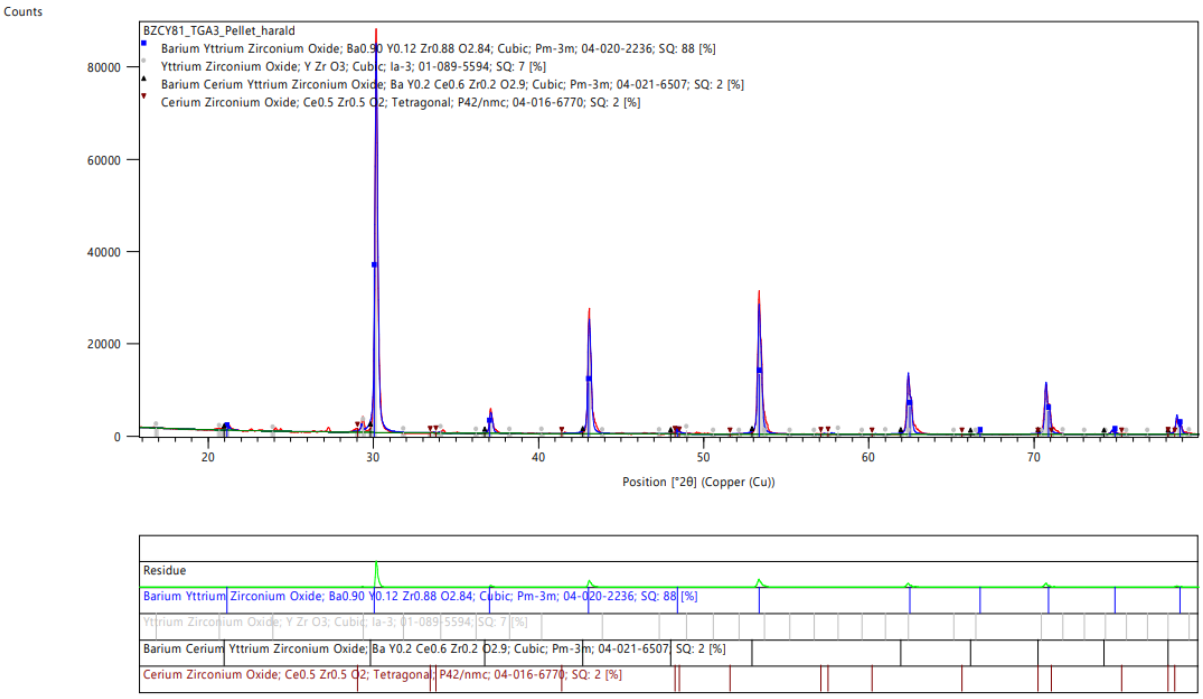

Figure 19: Diffractogram of Y- and Ce-doped barium zirconate pellet (SQ=semi quantitative)

4.1.2. Y-doped barium zirconate BZY15 pellets

Two different Y-doped barium zirconates, a green Y-doped barium zirconate and a black Y-doped barium zirconate were analysed. Both showed the same phase in their diffractogram with the same reflexes, therefore only one diffractogram is shown in Figure 20. The diffractogram shows no other phase.
The main difference is the sintering process resulting in a lower density of the green BZY15 compared with the black one, which contains NiO as sintering additive.

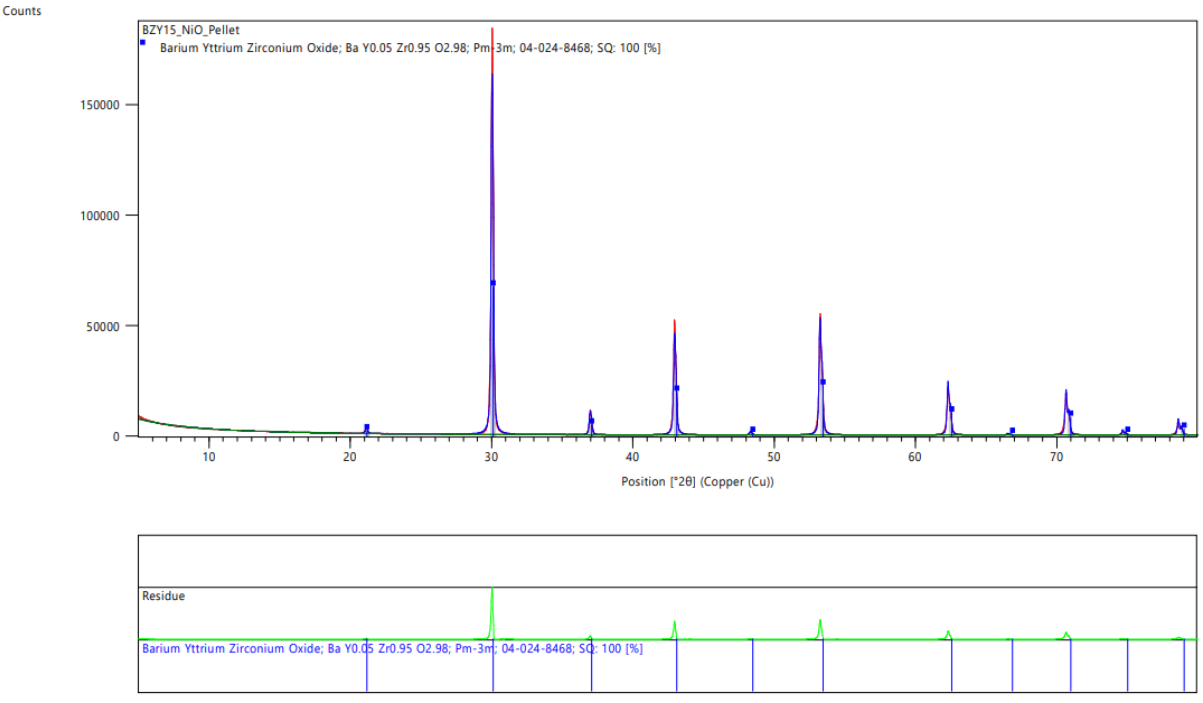

Figure 20: Diffractogram of the black Y -doped barium zirconate pellet (SQ=semi quantitative)

4.1.3. In-house sintered y-doped barium zirconate pellets

To prepare pellets by ourselves, a bought precursor powder was used to form monoaxially pressed and sintered pellets.

Sintering and characterization

It was important to coat the pellet in precursor powder to prevent loss of barium in the pellets at higher temperatures.
After sintering the white corundum crucible was coloured in blue due to incorporation of Ni from the sintering aid and the surface of the precursor powder was white, see Figure 21.

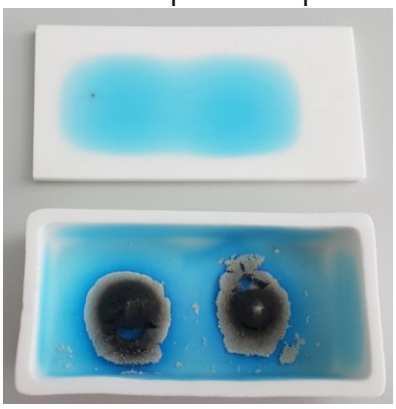

Figure 21: Two in-house sintered BZY15 pellet surrounded by precursor powder after sintering in a corundum crucible

Additional LIBS measurements approved enrichment of barium and nickel in the blue areas of the corundum crucible. The pellet and the white precursor powder of the surface show some similar reflexes, but different phases were predicted, see Figure 22.

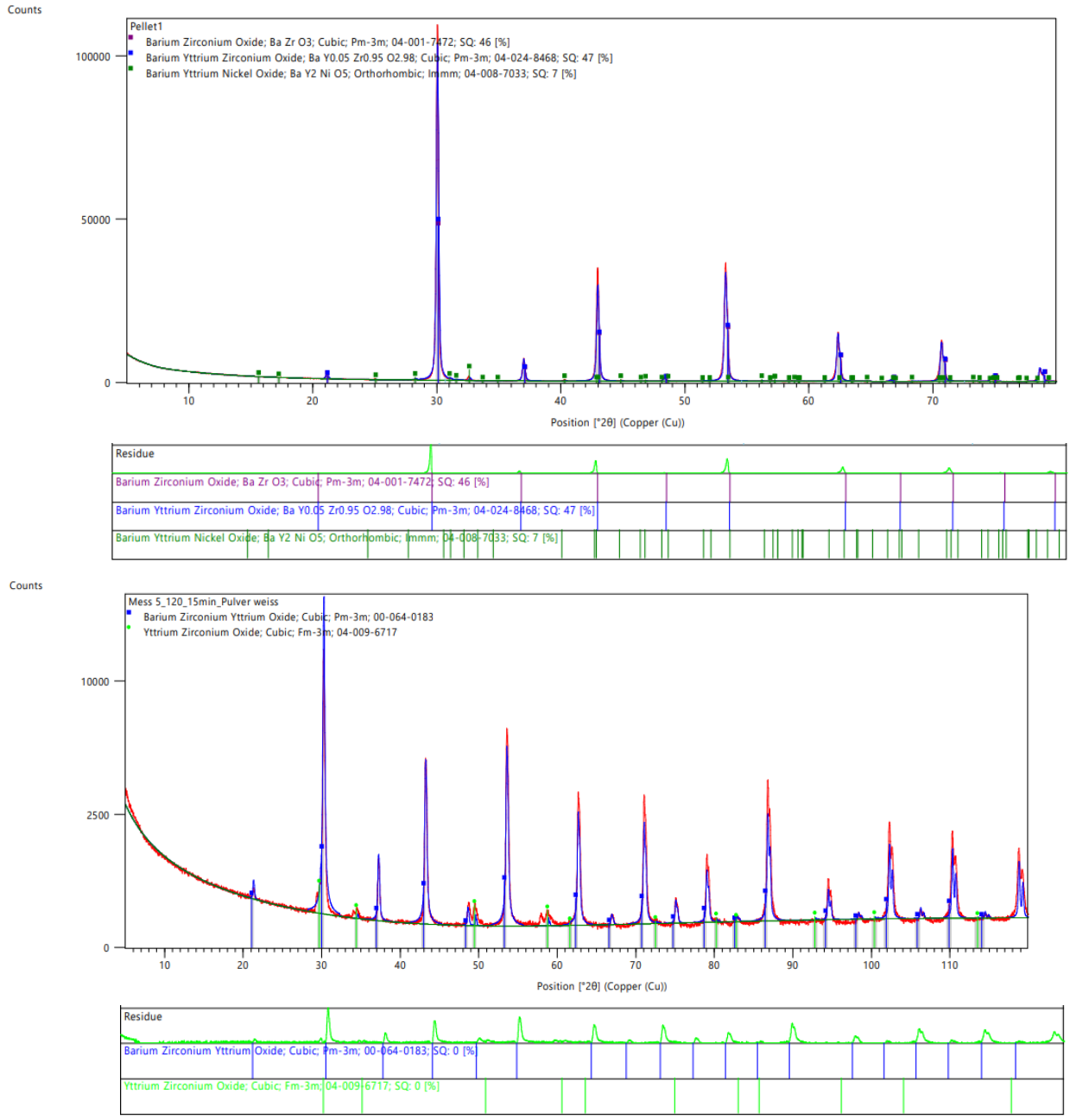

Figure 22: X-ray diffraction of the sintered in-house sintered BZY15 pellet (first row: XRD of in-house sintered BZY15 pellet 1; second row: XRD of the white sintered precursor powder of the surface)

The in-house sintered BZY15 pellet shows a barium zirconium oxide phase, a Y-doped barium zirconium phase and a phase of the barium yttrium oxide with the sintering additive NiO. It has to be considered, that the prediction of the undoped and doped barium zirconium oxide is the same phase and cannot be differentiated by our X-ray measurement. The Rietveld refinement predicted 92.2 % barium zirconium oxide and 7.8 % barium yttrium nickel oxide.
In comparison, the white precursor powder showed only two phases, barium zirconium yttrium oxide and an yttrium zirconium oxide phase. The phase without barium and no NiO-including phase underline the diffusion of barium and nickel at elevated temperatures from the surface of the precursor powder into the corundum crucible.

4.2. Thermogravimetric analysis setup and optimization

The setup and the optimization of the TGA is illustrated in Figure 23.

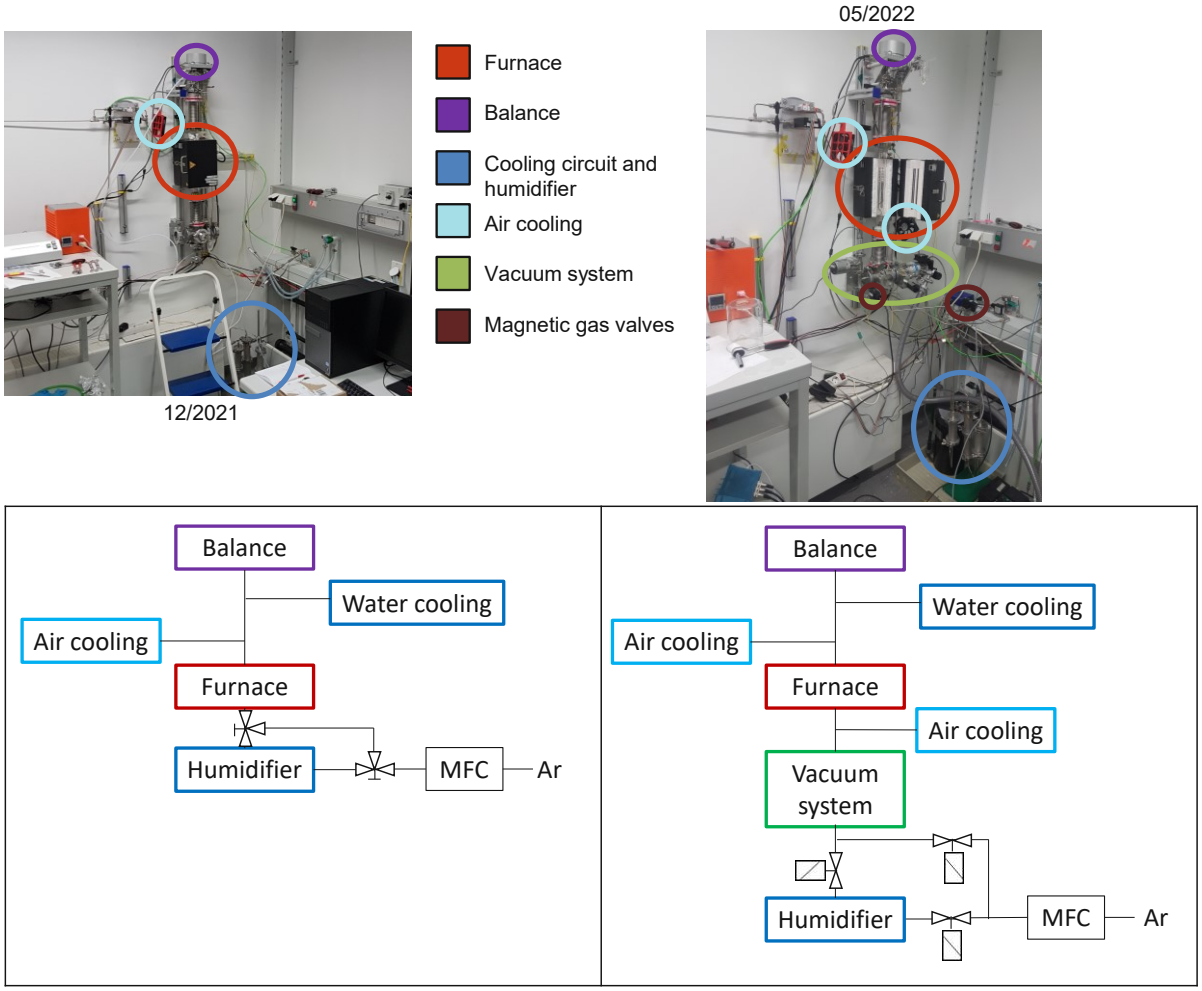

Figure 23: Optimization of the TGA setup (left: how it started in December 2021; right: how it was in May 2022)

Before the approach implemented within this thesis, the TGA setup was basically a furnace (maximum of 1000°C), a microbalance MK2-M5 Weigh Head and DISBAL Control Unit (Precision), an air ventilation, a riser pipe for humidification, a mass flow control (MFC) and cooling circuit above the furnace. The plastic gas pipes were connected and disconnected by Swagelok® quick-connects and the gas stream was from the bottom to the top with a gas flow of 20 sccm.

For further optimization first water incorporation experiments by thermogravimetric analysis from a BZCY81 pellet were done, see Figure 24. The first row on the left shows a drying step at 800°C under dry argon, decreasing temperature to 400°C and flushing the gas phase by humidified argon after reaching equilibrated weight. Here no weight change is visible. Maybe the diffusion of the oxygen vacancies at 400°C was too slow and therefore no weight change is visible. The followed increasing temperature to 800°C shows an increase in weight due to the less density of humidified argon at 800°C and some possible water uptake. The temperature is decreased to room temperature and the weight is still at a higher level than at 400°C. This indicates a weight change due to water uptake. The first row on the right shows the drying of the BZCY81 pellet under dry argon. By reducing the temperature and holding the temperature each 100°C step shows the influence of the temperature-dependent gas density. High temperatures lead to low density of the gas phase and therefore higher weight of the

sample. From 1000-700°C every temperature change is visible in the weight change curve, which is about 0.02% (0.002 wt. % H). Only at the step from 200 to 100°C and from 100°C to room temperature the weight change is positive, which is probable due to adsorption of some residual moisture. In general, it was suspected that the effect of oxygen vacancy generation or annihilation introduces a bigger weight change than the gas density at different temperature steps. The residual oxygen content in the apparatus should be high enough to visualize the increase in weight but maybe slow surface kinetics prevents the incorporation of oxygen and only the gas effect is visible.

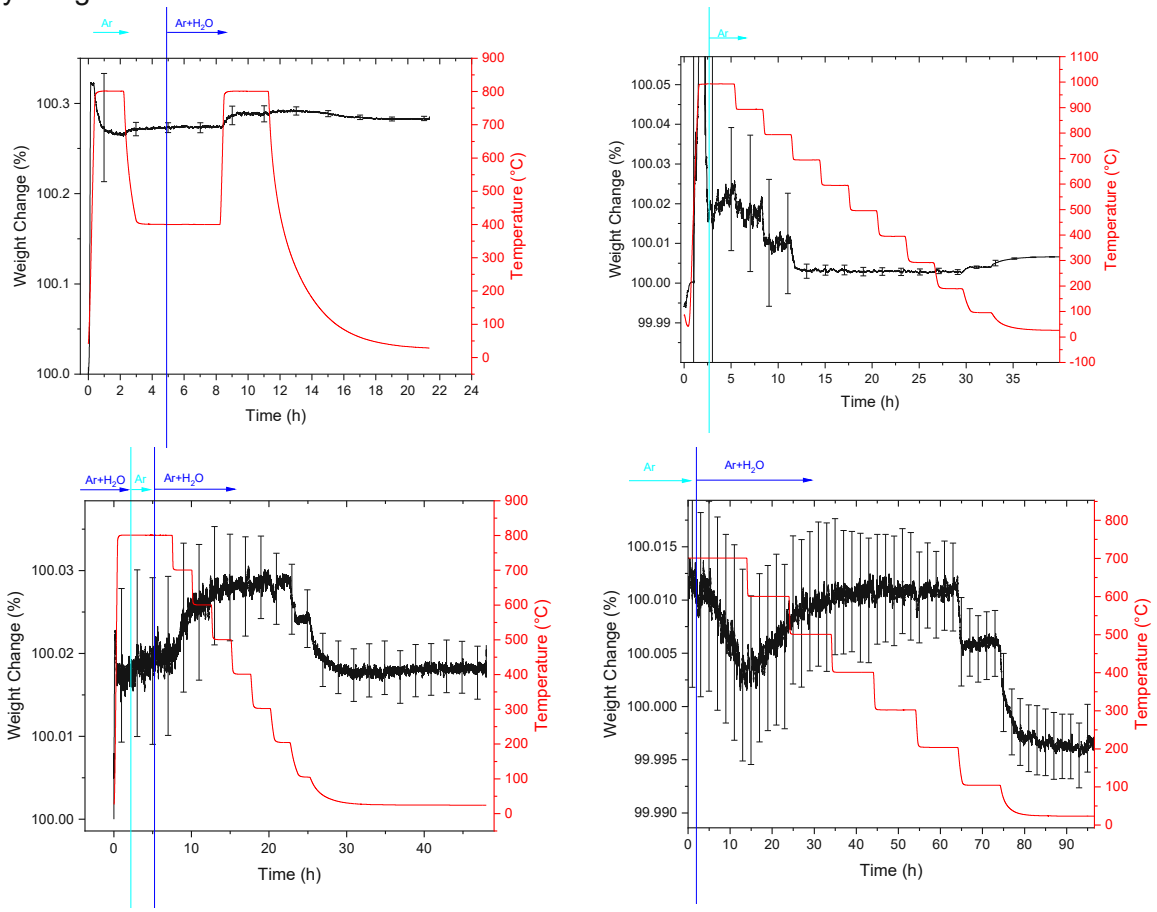

**Figure 24: Thermogravimetric analysis measurements of Y- and Ce-doped barium zirconate (first row: 1.TGA humidification at 400°C and 800°C, 15.TGA drying and gas effects at decreasing temperature steps;
second row: 2.TGA humidification at decreasing temperature steps, 4.TGA humidification at decreasing temperature steps)**

In the second row of Figure 24, two humidification experiments at decreasing temperature steps show two different phenomena. By decreasing the temperature, the gas density becomes denser and the weight of the sample decreases. On the other hand, the water uptake is more favoured at lower temperatures and therefore the weight should increase. After all available and useable oxygen vacancies are filled, the sample weight probably only decreases in the steps from 200 to 100°C and 0°C due to the increase of the gas density.
Due to the surprisingly small water uptake of BZCY81 which apparently was in the same order as gas density changes with varying temperature, this type of ceramic was not further investigated by means of TGA.

The direction of gas flow was changed after the 6.TGA measurement because the balancing seemed to be more stable by streaming the gas from the bottom to the top.
After the eighth TGA measurement water adsorption inside the system was recognized. To have the opportunity to dry the whole system, a turbomolecular pump, a toggle locking unit, a backing pump with a screw valve and a relief valve before the gas bubbler was added. Furthermore, the water cooling was changed from the in-house cooling circuit to a cooling circuit at room temperature. The strong cooling effect of the inhouse cooling resulted in condensation above the furnace and the room temperature cooling circuit prevented this effect. After the 19th TGA measurement, possible gas diffusion through the plastic gas pipes was eliminated by using metal gas pipes and gas valves and later magnetic gas valves made a more automatic measurement possible. A second air ventilation was added under the furnace to have a more controlled cooling of the glass tube.
The optimized thermogravimetric analysis setup is illustrated in Figure 25 on the left side and a more detailed view of the sample mounting on the right. Besides the main components, like the balance and furnace, a cooling circuit cools down the system above the furnace with water at room temperature by a circulation pump. Air coolers above and underneath the furnace ensures a cooler temperature for the sealing rings, which are used to connect the glass tube with the flanges. Flexible metal tubes allow to centre the sample easier. The whole system is flushed by a gas stream of argon and controlled by a mass flow controller (MFC). If valve 2 and valve 4 are open, the argon bubbles through a riser pipe which contains water and this humidified gas phase gets into the system and bubbles through the relief valve, which opens at an overpressure of 1 psi (68.9 mbar) and an oil (gas bubbler). This relief valve helps to visualize, if the apparatus is airtight or if somewhere a leak allows diffusion to or from the lab air. The system can be under vacuum by running a backing pump and a turbomolecular pump by controlling the necessary valves (spool and rotary valve). This allows to dry the apparatus faster or find leaks in the apparatus. The pressure can be measured by two pressure load cells, for the prevacuum and high vacuum level. To prevent leaks, the connection between glass pipe and metal flange system by ceramic glue or two-components glue was changed to an aluminium flange and implemented Viton® sealings. Viton® allows temperatures of about 200°C and the leak tightness is guaranteed by using screws in the aluminium flange system to tighten the sealing with the same force all over the sealing surface.

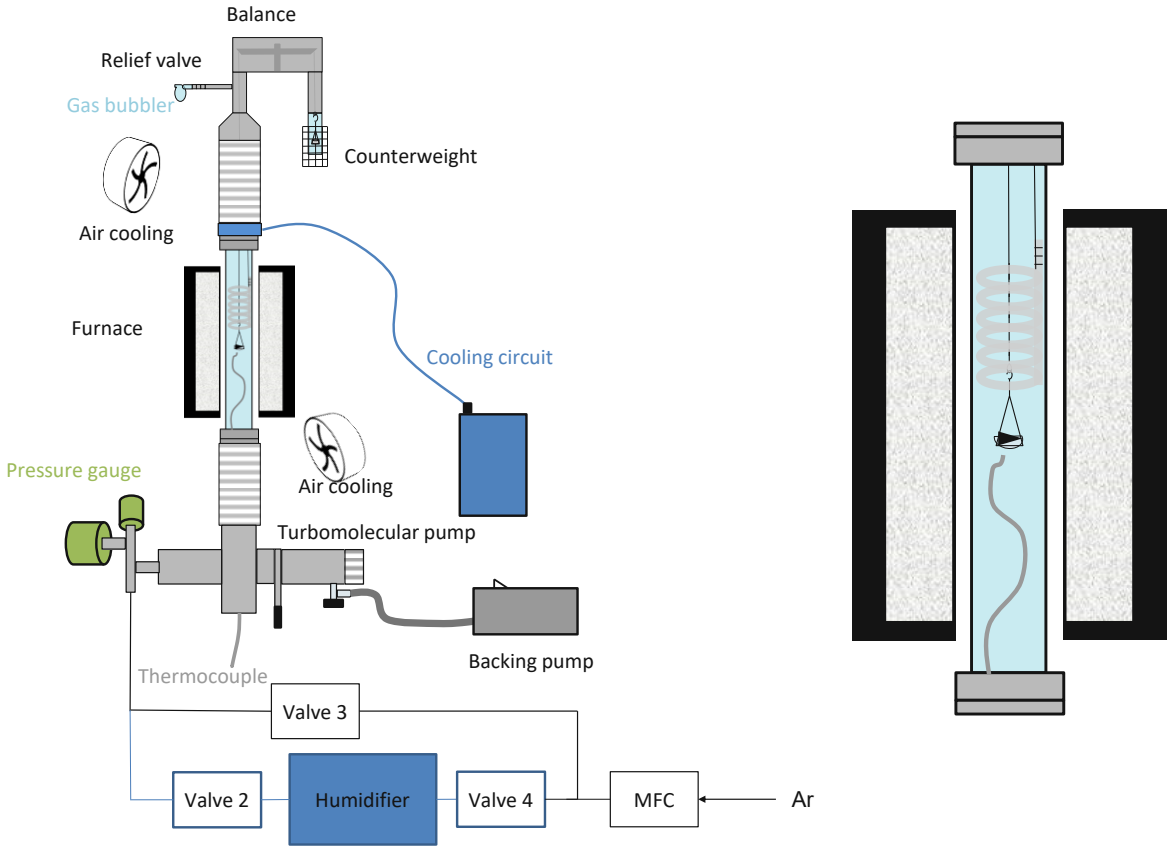

Figure 25: Schematic visualization of the used thermogravimetric analysis setup (left: overview of all components; right: detail view of sample mounting)

On the right side in Figure 25, the sample mounting is shown in more detail. From the bottom a thermocouple (type K) measures the temperature within about 1 cm distance to the sample. Quartz glass and platin hooks are connected to the balance beam and to the sample mounting. A quartz bowl is fixed inside the sample mounting and holds the sample. Above the sample a shield made out of glass is used to prevent fluctuations and decrease noise, as described by Saadatkhah et al. [69]. It is fixed at the upper flange, to be as stable as possible.

4.3. Water incorporation experiments

After the optimization of the TGA set-up, water incorporation experiments were done. Here the aim was to find the perfect temperature for water incorporation. Diffusion and thermodynamics suggest different optimum temperatures for water incorporation. While diffusion of oxygen vacancies and hydrogen is preferred at elevated temperatures, thermodynamics suggest low temperatures for higher water uptake. In the beginning, oxygen vacancies near the surface are quickly used for water uptake, but only at higher temperatures the oxygen vacancies in the middle of the sample have enough mobility. Especially for pellets the diffusion length is bigger and this increases the necessary temperature.
Therefore, the temperature for the water incorporation experiments was optimized and this temperature was used for water incorporation experiments described in chapter 4.3.2.

4.3.1. Varying the temperature to find the highest water incorporation

First temperature varying TGA measurements were done with the green BZY15 pellet, but big weight losses appeared while humidification at elevated temperatures. The pellet fractured, probably due to hydration induced expansion. Some smaller pieces fell off the sample mounting and caused those weight losses. Furthermore, the colour of the sample changed from green to yellow, see Figure 26.

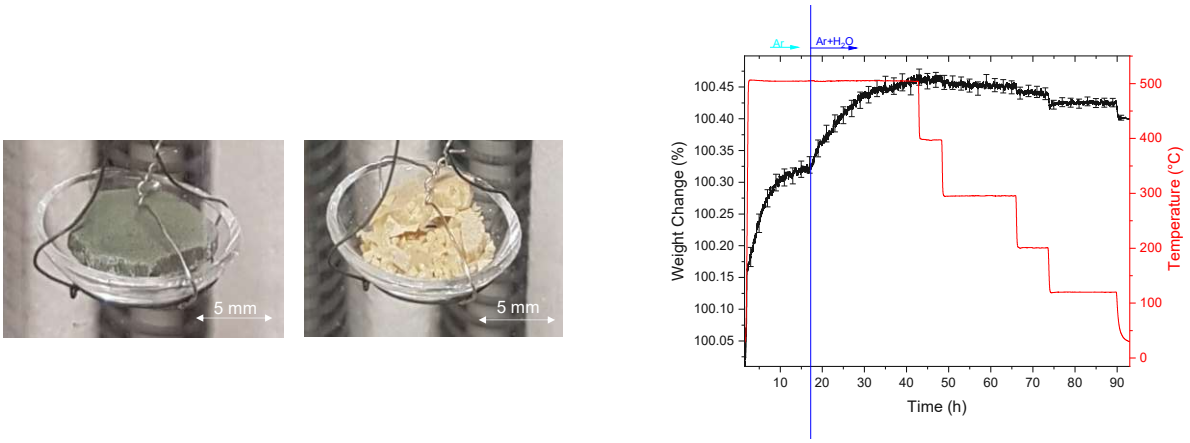

Figure 26: Thermogravimetric analysis measurements of Y-doped barium zirconate (left: optical difference due to humidification of green BZY15 pellet, right: 19.TGA humidification of black BZY15 at decreasing temperature steps and equilibration times of 26 h at 505°C, 5 h at 400°C, 17 h at 294°C, 7 h at 201°C and 15 h at 119°C)

Han et al.[86] already found such a phase separation, as well as thermal and chemical expansion at higher temperatures and humidification. Fabbri et al. [14] already published the shrinkage behaviour of green BZY pellets, which increased with the amount of Y-dopant. Fabbri et al. [14] reported about a shrinkage at 400°C under flowing air due to water release. Already grinding broke the green BZY15 apart and shows how brittle it was. In comparison, the black BZY15 did not show this behaviour. It was denser and more stable due to an improved sintering process using sintering additive NiO. The sintering process included a ramp rate of 5°C/min to 1500°C and dwell time of 12 h. A ramp rate of 1°C/min to 1200°C and 5°C to room temperature concluded the sintering process.

The humidification of the black BZY15 pellet at decreasing temperature steps is shown on the right side of Figure 26. First suggestions include that the optimal temperature range was lower than 500°C. Here the pellet was dried at 500°C and by switching to humidified argon the weight increased simultaneously. Decreasing the temperature only shows the gas density effect since the weight decreases, although from thermodynamics and literature it is known that the water uptake increases with decreasing temperature. Consequently, the water uptake kinetics at these low temperatures are expected to be poor and the decreasing weight with decreasing temperature is most probably due to increasing gas density. The biggest weight change was recognized at 500°C suggesting that the weight change may be even higher at elevated temperatures.

Therefore, the starting temperature for the humidification at decreasing temperature steps of the in-house sintered BZY15 pellet was increased to 800°C, see Figure 27. In general, directly after switching from dry argon to humidified argon the weight increases, but 10 h after switching to humidified argon the mass decreases for about 7 h. This phenomenon is not understood till now. For each following temperature step, the weight change is increasing till

the difference of gas density is higher than the uptake of water and therefore the curve shows a negative change in mass. The biggest weight change is in the range of 700-500°C.

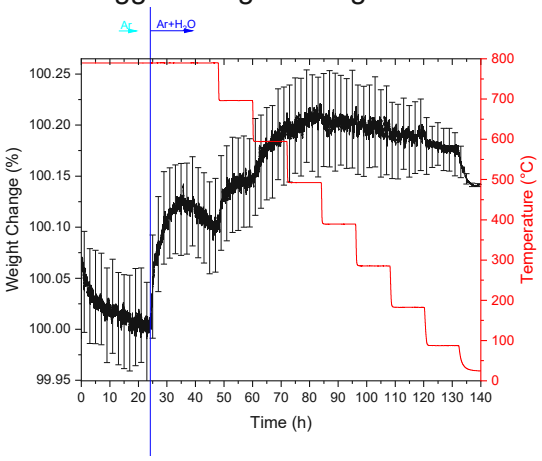

Figure 27: Thermogravimetric analysis – water uptake of in-house sintered BZY15 pellet at decreasing temperature steps and equilibration time of 24 h at 789°C and 12 h for all other temperatures (31.TGA)

To analyse the influence of the temperature of humidification faster, different temperatures were used ex-situ to humidify a BZY15 pellet. In Figure 28, a BZY15 pellet was measured with the same drying program used in the TGA at 800°C for 24 h, but humidification at different temperatures for 20 h (300°C, 550°C, 600°C). Here the error bar represents the uncertainty of the balance.

The first humidification shows the highest weight change which probably is due to the more complete drying. Therefore, more oxygen vacancies are available and a higher water uptake is possible. By reducing the temperature to 300°C, thermodynamically a higher water uptake is expected, but the diffusion is decreased and therefore it needs more time to reach an equilibrium. Due to the same dwell time at 300°C as at 550°C, the water uptake is maybe not equilibrated. By increasing the temperature to 650°C, thermodynamics predicts lower water uptake, which is recorded in the data, and a faster equilibration time is suspected. Changing the temperature again to 550°C, the water content is less compared to the first humidification at 550°C. The less complete drying, like already mentioned, can be the reason for this difference.

A possible error in this setting could be a little change of the sample position in the furnace which causes little changes in the temperature of the sample. But in general, this will only affect little changes in the water uptake. Furthermore, we can not be sure that the equilibration time for water uptake is covered in our measurement time of 20 h, especially for lower temperatures. The temperature steps directly after the gas phase change maybe do include some effects due to not equilibrated humidified gas phase.

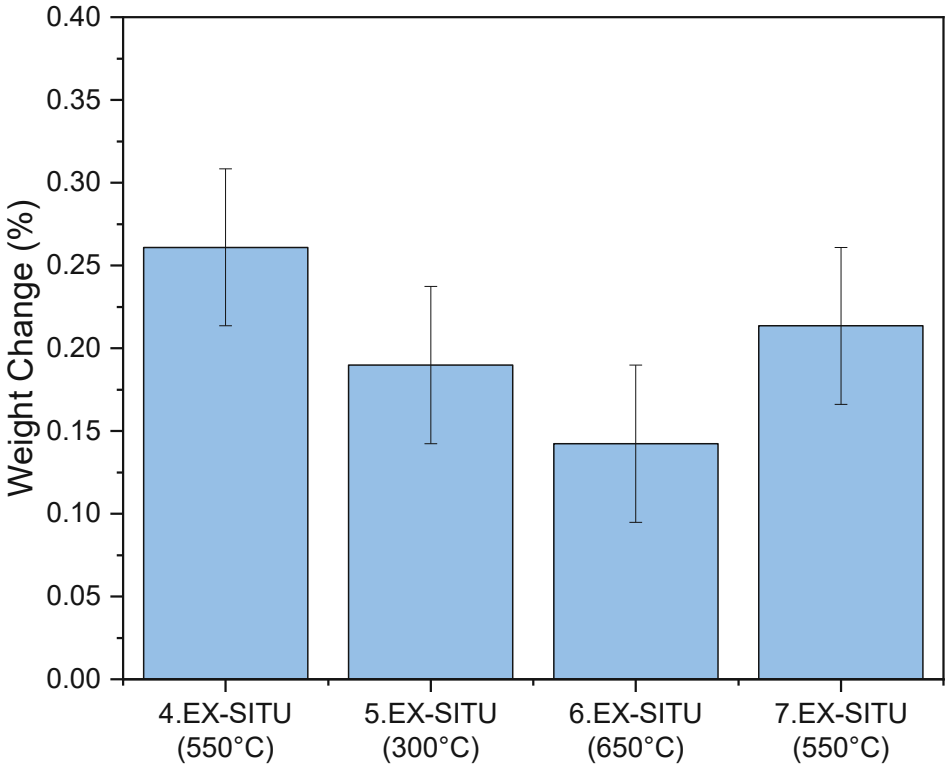

Figure 28: Temperature variation for ex-situ humidification of a Y-doped barium zirconate pellet (BZY15-B)

A temperature of about 550°C seems to be the optimum for the humidification of our BZY15 pellet. In the literature only BZY powders were used for thermogravimetric analysis and Groß et al.[17] generally predicted a higher water uptake at lower temperatures, but we measured pellets and this can introduce another factor. This factor is the temperature-dependency of the diffusion kinetics of oxygen vacancies. Powders require a much shorter diffusion length, which leads to fast equilibration times. At low temperatures and with long diffusion lengths as in pellets, long equilibration times can be expected. In order to compare our results with literature, in-house sintered BZY15 pellets were grinded and the TGA humidification of this powder is shown in Figure 29.

The powder was dried at 800°C in argon and the gas phase was changed to humidified argon by increasing the gas flow to 5 L/min for five minutes, see right side of Figure 29. This procedure should ensure a faster equilibration of the humidified gas phase in the TGA apparatus. The higher gas flow introduces a weight decrease, because the sample is lifted due the flow and furthermore the temperature decreases as well. After switching back to the standard gas flow of 20 sccm (0.02 L/min), the weight change curve rises up again, even a little higher than before flushing most probably due to an already started water incorporation of the sample. The temperature approaches the same level, but while coming closer to the starting temperature, it rises in some stair treads. Probably this is caused by a smaller heating rate when the temperature almost reached the set-temperature and to stabilize the temperature.

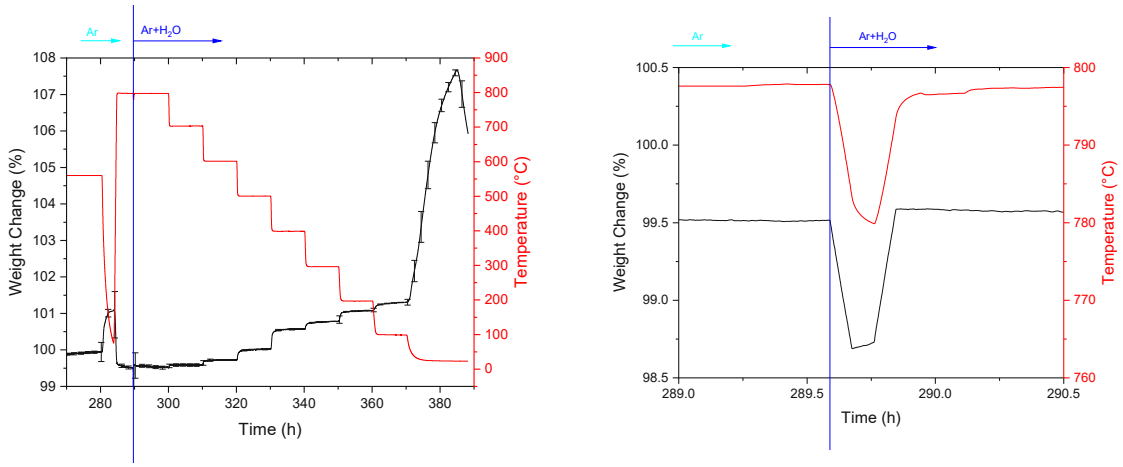

Figure 29: Thermogravimetric analysis – water uptake of grinded in-house sintered BZY15 powder at decreasing temperature steps (32.TGA: BZY15 Powder). The right diagram shows flushing with higher gas flow of 5 L/min.

The weight change at each temperature step is summarized in Table 13. The difference from the actual temperature and the temperature step before defines the water uptake for the actual temperature, if only water incorporation is assumed. The hydrogen uptake is calculated by multiplying the factor 2/18, the molecular weight proportion of hydrogen in water.

Table 13: Weight change and Hydrogen uptake at temperature steps

Temperature (°C)	Weight change (%)	Water uptake (wt. %)	Hydrogen uptake (wt. %)
797.6	99.52	-	-
703.2	99.59	0.0705	0.0078
601.6	99.72	0.1327	0.0147
500.6	100.02	0.2967	0.0330
398.4	100.57	0.5501	0.0611
296.3	100.78	0.2128	0.0236
196.7	101.08	0.2962	0.0329
99.1	101.30	0.2236	0.0248

The highest weight change at 400°C indicates the best conditions for water incorporation of this BZY15 powder. In the end, the sample is cooled down to room temperature and a big weight change is visible, most probably due to water adsorption on the powder surface.

The determined hydrogen uptake is compared in Figure 30 to the literature data (calculated and ^{15}N NRRA measured H-concentrations), which was already discussed in chapter 2.3 (see Figure 8).
The hydrogen concentrations of the TGA measurement deviate from the calculated data, but at 600°C the determined H-concentration is comparable to the literature.

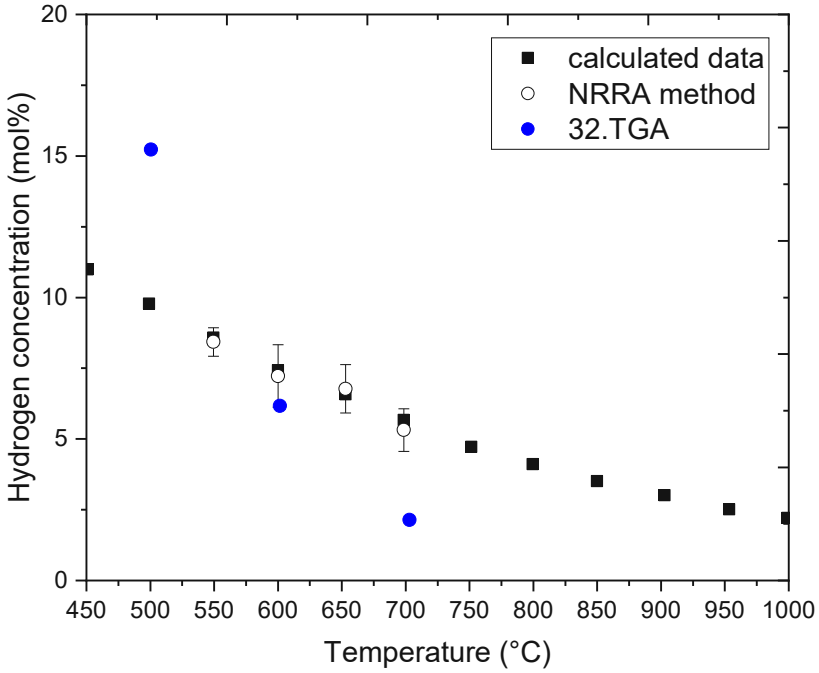

Figure 30: Hydrogen concentration in BZY15 determined by thermogravimetric analysis, ^{15}N NRRA method and calculated data.
(black squares represent calculated hydrogen concentration, modified from[17];
open circles represent measured data using the ^{15}N NRRA method, including the statistical errors modified from[17];
blue circles represent measured thermogravimetric analysis date of the 32.TGA: grinded in-house sintered BZY15 powder at decreasing temperature steps)

Like shown before, BZY15 pellets show bigger weight changes in the range of 500-700°C and ex-situ measurements showed the highest weight change at 550°C. This difference of the optimum temperature compared to the powder experiments is ascribed to the diffusion limitation of the pellet samples at low temperatures. Therefore, the optimized temperature for pellets seems to be in the range of 550°C. This temperature is used in the water incorporation experiments in the next chapter.

4.3.2. Water incorporation experiments at optimal temperature

After optimization, the following procedure was considered as standard measurement protocol for water incorporation experiments of pellet samples: A drying step at 800°C for 6 h, an equilibration step at 550°C for 20 h and a humidification step at 550°C for 24 h.

The water incorporation experiment of a BZY15 pellet is shown in Figure 31. After drying at 800°C, the weight stabilized at 550°C and an immediate increase while humidification is registered. The slope of the weight change is almost linear and finds a plateau after 10 h of humidification. This long equilibration time maybe is due to slow diffusion and equilibration of

the humidified atmosphere. Diffusion is slower at 550°C compared to higher temperatures and especially for longer diffusion distances like in pellets. The gas phase equilibrates slow, because humidified argon is mixed with dry argon inside the apparatus and the mixture bubbles through the relief valve.
In the end the temperature decreases to room temperature and the fast decrease in weight is due to the higher gas density at room temperature.
Besides the gas density, the temperature effects the standard deviation. Fluctuations due to heating can introduce bigger disturbances due to buoyancy and thermally introduced turbulences therefore result in higher standard deviations at elevated temperatures. At room temperature the standard deviation is much smaller than for example at 550°C.

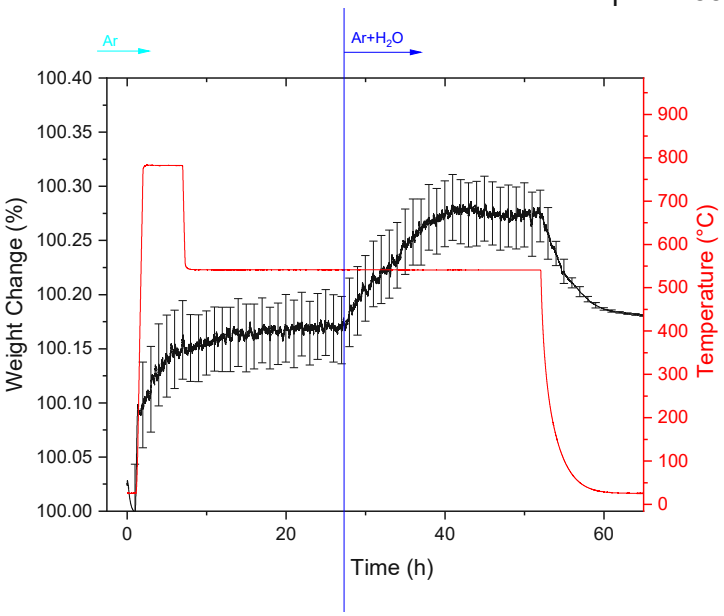

Figure 31: Thermogravimetric analysis – water uptake of Y-doped barium zirconate pellet (21.TGA)

In comparison to powder measurements in literature and in this study, the experimentally determined 0.1062 % (0.0118 wt. % H) weight change of the BZY15 pellet, see Figure 31, is smaller.
Yamazaki et al.[16] showed a weight change from 800°C to 500°C of about 0.18 % for 20 mol% Y-doped barium zirconate powder, which can be corrected by the factor of 15/20 for an expected weight change of 0.135 % for BZY15. Gonçalves et al.[15] reported a weight change of 0.15 % for BZY15, when applying a correction factor of 15/20 to the BZY20 results. The water uptake experiment of Yamazaki et al.[16] included a drying step at 1000°C for 0.5 h under dry nitrogen to remove water and possible surface carbon dioxide. The gas phase was saturated by water (p_{H_2O}=0.023 atm) and the temperature decreased by steps of 100°C to room temperature and equilibration times of 2 h. The water uptake experiments of Goncalves et al.[15] only differ by usage of dry air and humidified air (p_{H_2O}=0.021 atm) and the equilibration time for each temperature of 3 h was programmed.

Theoretically maximum possible water incorporation in BZY15 allows 0.4923% (0.0547 wt. % H), with the assumption of one hydrogen for each yttrium, because two yttrium result in a protonation of an oxygen and incorporation of OH in an oxygen vacancy. Groß et al.[17] predicted by their NRRA measurement 9 mol % H for humidifying dry BZY15 at 550°C. This equals a weight change of 0.2952 % (0.0328 wt. % H), which is in very good agreement with the values we found – compare Table 13.

The main difference between the literature and our experiments is that we used pellets and in literature only powders were measured. For us it was important to use pellets, which can be analysed by LIBS because powders need to be pressed and this can introduce more error sources for the hydrogen quantification.

Furthermore, in literature only fresh sintered powder is used and the humidified powder is not dried again and used for another measurement. In some experiments the drying and humidification result in lower weight changes compared to the fresh sintered pellets (1600°C) or powders. The drying temperature of 800°C seems to be not high enough to reproduce the same amount of oxygen vacancies like for the first measurement directly after the sintering process. Groß et al.[17] showed a dependency of the hydrogen concentration to the temperature of drying. In section 4.3.3 the dependency of the number of humidification and drying temperature is described in more detail.

The reproducibility of the new setup of the thermogravimetric analysis needed to be confirmed and therefore ex-situ measurements were performed in a separated furnace and weight determination by an analytical balance at room temperature. Two ex-situ experiments are plotted in Figure 32. In each measurement a drying step at 800°C and the humidification at 590°C was included to allow comparison to the thermogravimetric analysis. Therefore, the weight of the sample was determined before drying, after drying and after humidification. Here a weight change of 0.1514 % (0.0168 wt. % H) and 0.1279 % (0.0142 wt. % H) was registered. The first measurement was directly after sintering and the second measurement was directly after the first measurement. The smaller weight change indicates a not complete drying and therefore less available oxygen vacancies result in a lower water incorporation.

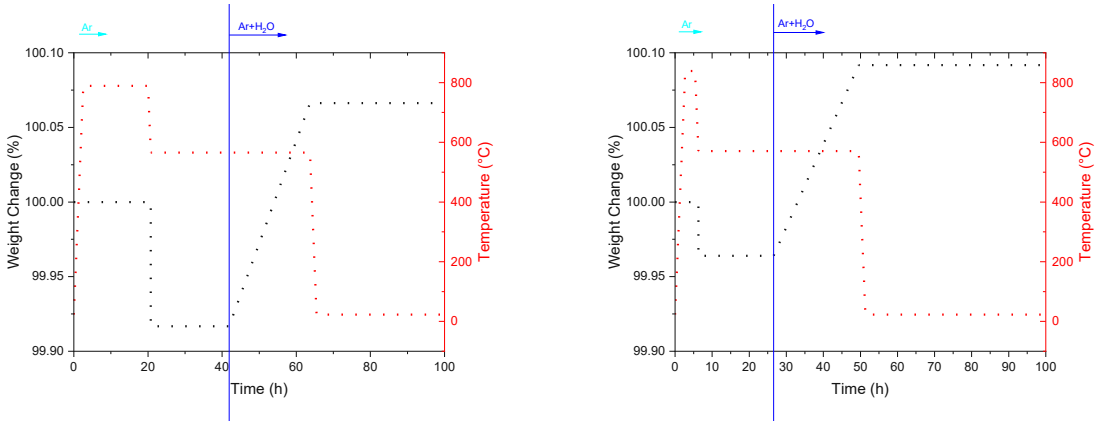

Figure 32: Ex-situ humidification experiments of BZY15 pellets (left: 10.EX-SITU BZY15-Da; right: 11.EX-SITU BZY15-Pellet2)

The thermogravimetric measurements of the in-house sintered BZY15 pellets are shown in Figure 33. The first water uptake experiment in the left plot shows the highest weight change of 0.1420 % (0.0158 wt. % H) due to the higher drying temperature while sintering. After humidification the temperature was decreased to room temperature, but the curve shows a smaller decrease in weight compared to the TGA measurement in Figure 31. The weight change should be comparable due to the higher gas density at room temperature. Maybe in the end of the measurement, the sample mounting touched the radiation shield or static charge caused the smaller than suspected decrease in weight. The bigger standard deviation at room temperature indicates this as well. The second and third measurement on the right plot show weight changes of 0.0801 % (0.0089 wt. % H) and 0.0780 % (0.0087 wt. % H) that indicate a not fully-dried sample and therefore only a fraction of the oxygen vacancies are available for water incorporation.

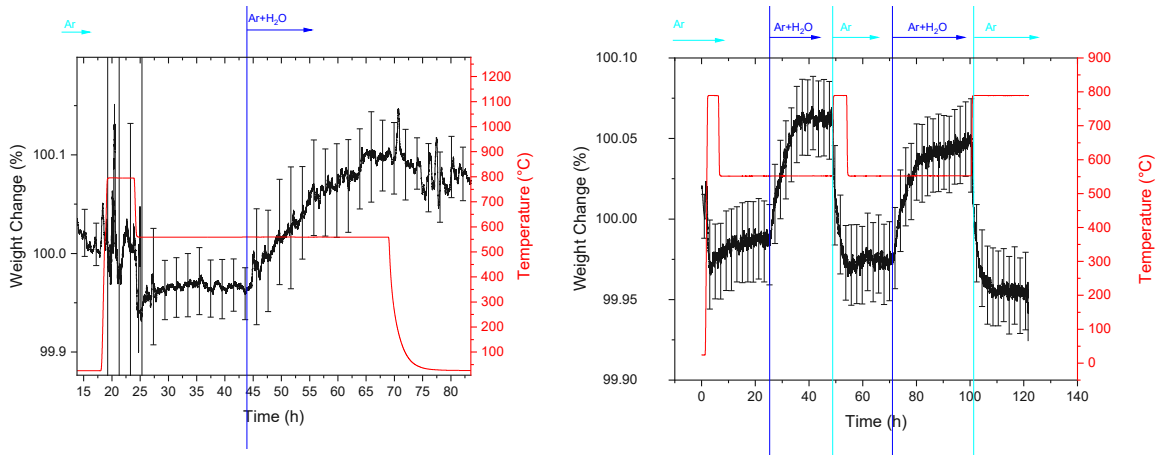

Figure 33: Thermogravimetric analysis – water uptake of in-house sintered BZY15 pellet (left: 27.TGA; right: 29.TGA including two humidification experiments)

The same trend due to the not complete drying of the BZY15 pellets at 800°C under dry argon is registered for inhouse-sintered (IHS) BZY15 pellets, see right plot of Figure 33. The first measurement shows a water uptake of about 0.1 % and the followed measurement shows a smaller weight change.
Furthermore, in Figure 33 different equilibration times can be compared. Drying at the higher temperature of about 800°C and dry argon shows a faster weight change compared to the weight change at 550°C under humidified argon. The diffusion length is the same, but the temperature effects diffusion strongly. Therefore, the humidification needs much more time than the drying step. Additionally, the long equilibration time, approximately 12 h, at 550°C indicate the long diffusion lengths for the pellet.

The ex-situ measurements show similar results of the water uptake experiments. Here, water uptake of 0.1415 % (0.0157 wt. % H) and 0.0996 % (0.0111 wt. % H) were registered, see Figure 34. The higher water uptake was directly after the sintering process and the lower water uptake was registered after humidification and drying at 800°C. The reason for this difference of water amount is again due to the incomplete drying and therefore smaller availability of oxygen vacancies for water incorporation, like already told in the sections before.

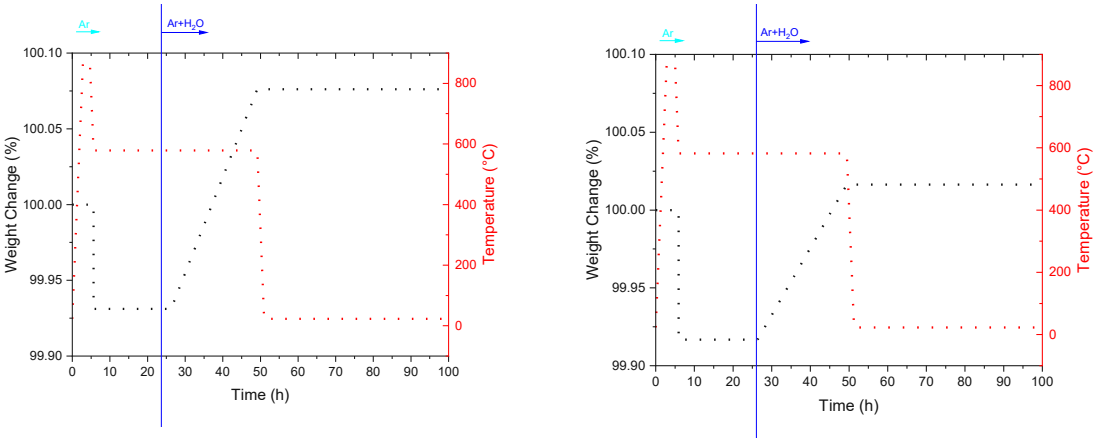

Figure 34: Ex-situ water incorporation experiments of in-house sintered BZY15 pellets (left: 13.EX-SITU; right: 14.EX-SITU)

The XRD Rietveld refinement of the dried in-house sintered BZY15 Pellet and humidified pellet allowed to show the difference of the crystallite size due to humidification. It shows an increase

of 578.0 Å (estimated standard deviation ESD 0.731 Å) to 711.9 Å (ESD 1.050 Å). Han et al.[86] also reported chemical expansion due to water uptake in the crystalline structure.

Due to the strong influence of drying, the in-house sintered BZY15 pellets were dried again at 1500°C, like in the sintering process. The measurement of this sintered pellet, denoted as IHS BZY15, is shown in Figure 35. The procedure is comparable to the measurement in Figure 33, but the measurement apparatus was flushed with humidified Ar with a flow of 5 L/min for 5 min. After this flush time the flow was reduced to 20 sccm. This procedure should ensure a faster equilibration of the humidified gas phase in the apparatus. The higher gas flow introduces a temporary weight decrease, because the sample is lifted due the flow. The temperature decreases as well because of this high flow. After switching back to the standard gas flow of 20 sccm, the weight change curve rises up again, even a little higher most probably due to water incorporation which already occurred during flushing. The temperature approaches the same level as before.

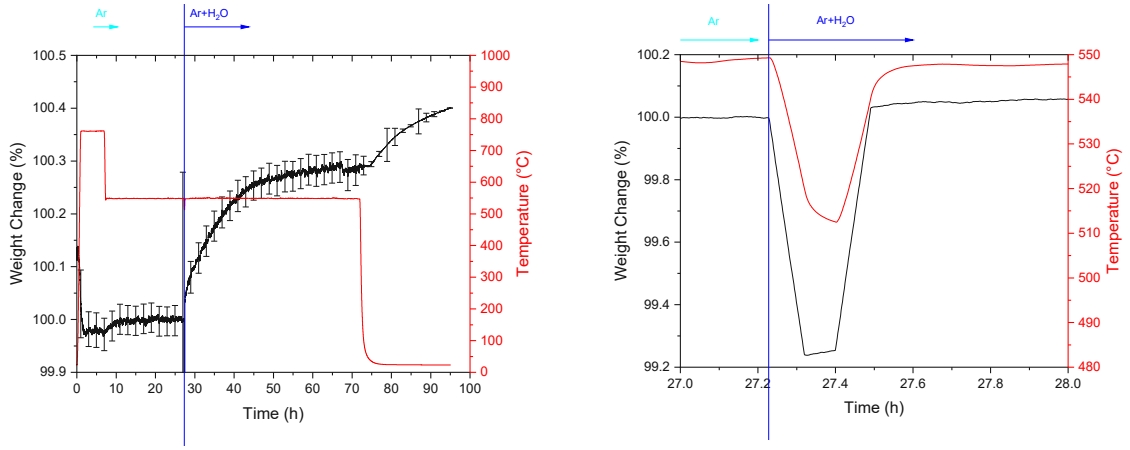

Figure 35: Thermogravimetric analysis – water uptake of the fresh sintered in-house sintered BZY15 pellet. The right diagram shows the humidification at higher gas flow of 5 L/min. (33.TGA)

In general, the weight change curve resembles a diffusion profile with a higher slope in the first 10 h. Then the slope decreases and the curve reaches a plateau after 35 h. A possible reason for this is the more available oxygen vacancies in the beginning and after this fast humidification of the surface near oxygen vacancies it needs more time to fill up the remaining oxygen vacancies. The weight change of 0.2872 % (0.0319 wt.%) is much higher than the weight change of the IHS BZY15 pellet in Figure 33. This further indicates that the drying temperature has a big influence for humidification and therefore the used 1500°C produces much more oxygen vacancies than drying at 800°C. Furthermore, eventually the density of the inhouse sintered pellets and extern sintered pellets slightly differ which can cause different water incorporation behaviour.
Compared to the TGA measurement of the BZY15 pellet in Figure 29, the equilibration time seems to be comparable. The higher gas flow while humidification does not decrease the equilibration time and therefore the equilibration of the gas phase is not the critical procedure. The long equilibration time is strongly affected by the slow diffusion of oxygen vacancies and hydrogen. Furthermore, the shape of the curve in Figure 35 shows a typical diffusion profile because the equilibration of the gas phase was ensured by the increased gas flow while humidification. The curve in Figure 31 maybe shows two processes, equilibration of the humidified gas phase and diffusion, at the same time.

In the end, the temperature is decreased to room temperature and a further increase of the weight is visible. This is due to thermodynamics, which predicted higher water incorporation at lower temperatures, but adsorption of water on the surface may also play a role here.

To show the difference in diffusion, grinded in-house sintered BZY15 powder was measured with the same procedure. In Figure 36 three different measurements of the powder are shown. All powder measurements show a fast increase of the weight and therefore connected fast humidification in the beginning and a followed process which takes more time for equilibration and to settle down in a plateau.

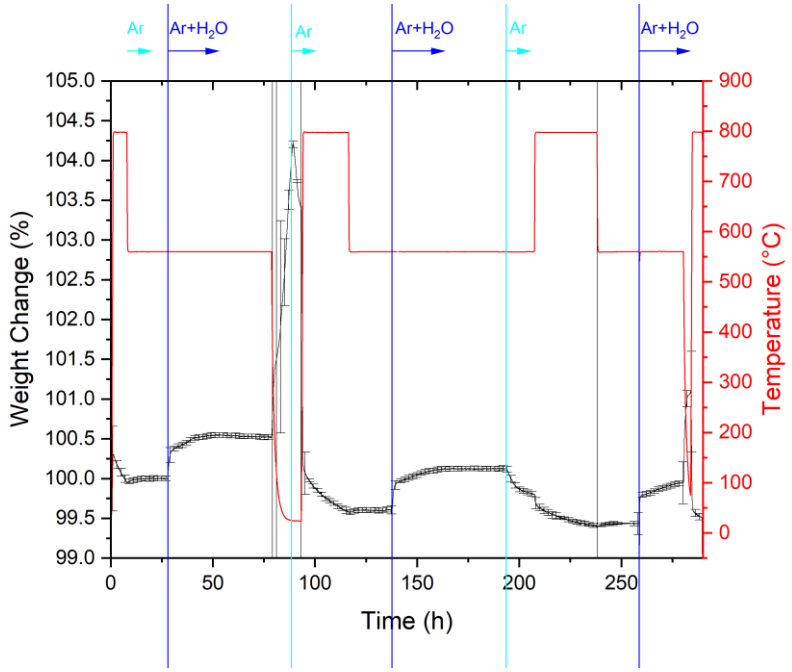

Figure 36: Thermogravimetric analysis – water uptake of grinded IHS BZY15 powder (32.TGA, overview of all measurements)

The first measurement, see first row of Figure 37 represents the humidification of the powder after sintering at 1500°C. After switching to humidified argon, the weight increases immediately and after 20 h the plateau visualizes the equilibrium. Compared to the equilibration time of the pellet with 35 h, the equilibrium is faster due to shorter diffusion lengts. A water uptake of about 0.5238 % is much higher than the compared weight change of the pellet of the same material. In the end, the temperature was decreased to room temperature and a very big weight change appeared, especially at low temperatures adsorption can introduce this increase due to the high surface area of powders. The surface area is very important for the kinetics of a reaction and for samples with a high surface the adsorption becomes more important. Often in literature, the Brunauer-Emmett-Teller (BET) method was used for determination of the surface area[15], [16].

The second measurement, see second row of Figure 37, should show the effect of drying at 800°C and if the following humidification is comparable to the humidification after sintering. Here the drying step was for 22 h and after switching to humidified argon, the equilibrium was reached after 25 h. A weight change due to water incorporation of 0.5216 % is comparable to the humidification after sintering. This indicates, that the drying at 800°C is high enough for the powder.

The third measurement in the third row of Figure 37 includes faster equilibration of the humidified argon gas phase inside the TGA due to increasing the gas flow to 2.5 L/min for nine minutes. In this measurement the drying step at 800°C was for 30 h and here the decreasing weight shows that the drying needs time. In the beginning, the drying works well, but the slope of the weight change gets smaller and smaller. Therefore, reaching equilibrium which results in a plateau needs a lot of time. The higher gas flow for humidification result in a decrease of the weight and temperature, like already told in the sections before. Compared to the first and second measurement, the plateau of equilibrated water incorporation was reached faster, approximately 20 h after humidification. This shows that the gas phase of full-saturated argon helps to accelerate the reaction. Groß et al.[17] showed that the proton concentration is dependent from the partial pressure of water, see Figure 8 in the section 2.3.. A higher pressure delivers higher proton concentrations, and this effect is shown if humidification is at higher flows and ensures a fast equilibrated water partial pressure. A water uptake of 0.5113 % is little less than the measurements before, but maybe the equilibrium was not entirely reached already and therefore some more time was needed.

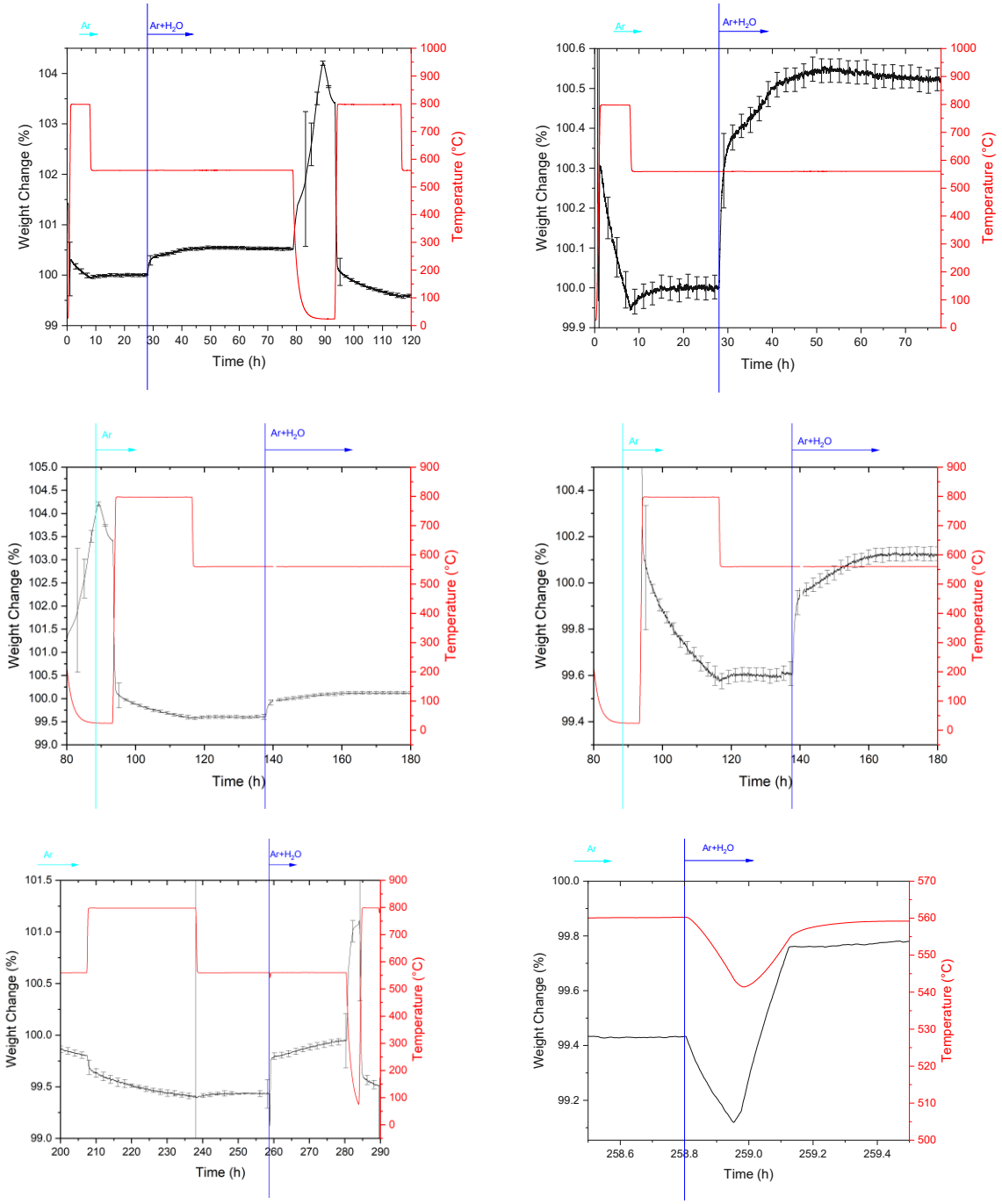

Figure 37: Thermogravimetric analysis – water uptake of grinded IHS BZY15 powder (first row: fresh sintered powder humidification at 550°C, detail of diagram; second row: drying at 800°C and humidification at 550°C, detail of diagram; third row: drying at 800°C and faster humidification by higher gas flow of 2.5 L/min., detail of increased gas flow)

Often the water uptake was dependent on the drying before humidification and this is discussed in more detail in the next chapter.

4.3.3. Water uptake dependency of the number of humidifications and drying temperature

In Figure 38 the number of humidification processes of an in-house sintered BZY15 pellet and a commercial (black) BZY15 pellet are compared. The first humidification is directly after the sintering at 1600°C, the second and third was dried in the TGA at only 800°C. Groß et al.[17] suggested the drying of the humidified BZY samples is a limiting factor for the reproducibility of the humidification. Like in Figure 8 visible, the hydrogen content is a function of the temperature and for reproducibility the drying temperature is important. According to Groß et al.[17], the drying step at 800°C leads to a residual hydrogen fraction of about 4 mol%. For BZY15, Groß et al.[17] published a residual hydrogen fraction of 1.75 mol% could not be removed at 700°C in a dried argon-oxygen (80/20) atmosphere. The experimental data shows that every humidification after drying at 800°C only shows a smaller weight change than the first humidification after sintering.

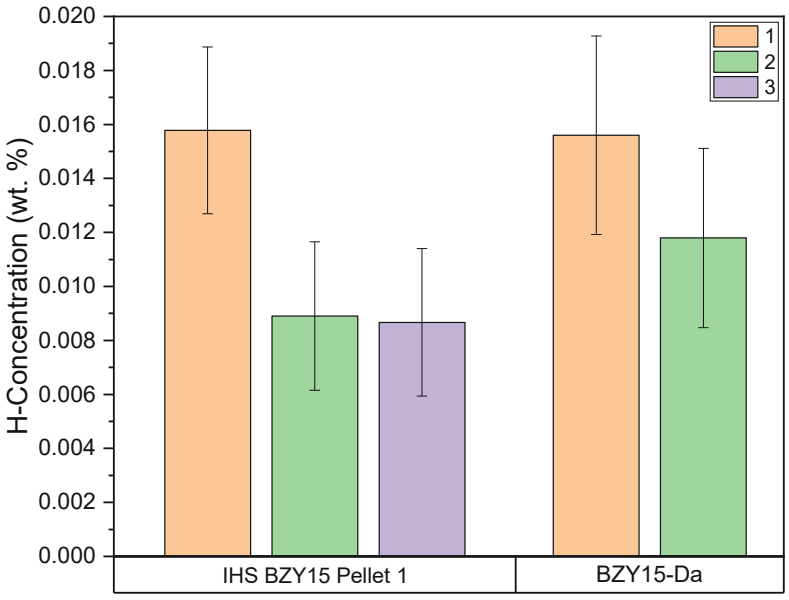

Figure 38: Water uptake dependency of the number of thermogravimetric analysis humidifications of the in-house sintered BZY15 pellet and a BZY15 pellet. The error bar represent the standard deviation of the mass at 550°C before humidification under dry argon.

Due to the new set-up of the TGA it was necessary to prove the weight changes and this is discussed in the next section.

4.3.4. Comparison of TGA and ex-situ measurements

We compared the TGA measurements to ex-situ experiments with the same temperature profile in a separate furnace. The weight changes were measured at room temperature with an analytical balance.

In Figure 39, TGA and ex-situ measurements of the same samples are compared. All samples are BZY15 samples. In general, the TGA experiments show a smaller weight change than the ex-situ determined values. Especially, the BZY15-B sample shows a bigger difference. Before this measurement, the TGA setup needed to be adapted and this resulted in a lower temperature for humidification. The same set-temperature was used, but probably the sample was at a slightly different position and possibly the glass wool insulated the furnace worse. The lower temperature limits the diffusion, especially for pellets and may explain the lower water uptake.

The error bars represent the standard deviation of the weight curve at the temperature of humidification at dry argon. For the ex-situ experiments the error bars represent the inaccuracy of balancing the same sample for three times. The sample “BZY15 Pellet 2” shows a smaller error bar, because the mass of the sample was much higher than the other samples.

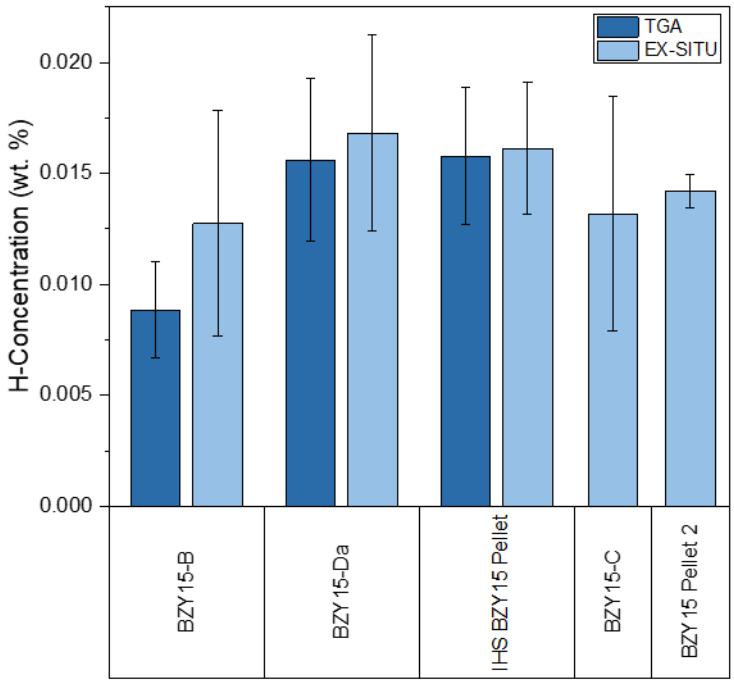

Figure 39: Comparison of TGA and ex-situ measurements (BZY15-B: 22.TGA and 2.EX-SITU; BZY15-Da: 19.TGA and 10.EX-SITU; IHS BZY15 Pellet: 27.TGA and 13.EX-SITU; BZY15-C:4.EX-SITU; BZY15 Pellet 2: 11.EX-SITU)

The relation between the thermogravimetric analysis and ex-situ data is visualized in Figure 40. The dotted line represents the ideal linear fit and the error bars of both measurement types are plotted. There is an almost ideal linear fit between TGA and ex-situ experiments. In general, ex-situ experiments show a little higher H-concentration, which can be caused due to measuring the weight change at different temperatures. Water adsorption mostly occurs at lower temperatures and therefore it is not included in the hydrogen concentration determined by TGA measurements. ex-situ measurements are measured at room temperature and water adsorption plays an important role, which leads to higher determined hydrogen concentrations. For example, the TGA measurement of BZY15 powder in Figure 29 or the TGA measurement of the inhouse-sintered BZY15 pellet in Figure 36 show an increase in weight at room temperature most probably due to water adsorption.

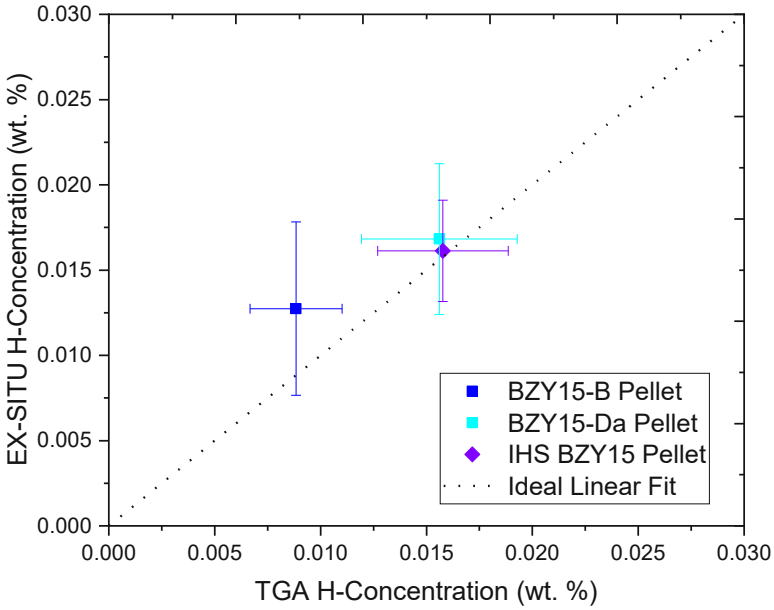

Figure 40: Comparison of TGA and ex-situ measurements. The dotted line represents the ideal linear fit. (BZY15-B: 22.TGA and 2.EX-SITU; BZY15-Da: 19.TGA and 10.EX-SITU; IHS BZY15 Pellet: 27.TGA and 13.EX-SITU)

The difference between powder and pellet measurements resulted in discussing the diffusion while humidification. Therefore, depth profiling found our interest and is discussed in the next section.

4.4. LIBS optimization and Hydrogen-Calibration curves

The quantification of small hydrogen amounts requests an optimization of the parameters to detect the hydrogen intensity with less background noise and minimal overlapping lines of other elements. Therefore, the parameters of the ICCD detector like the gate delay GD, the gate width GW and the intensifier gain IG were optimized while measuring the highest standard with a hydrogen concentration of 0.6142 wt. %. The variation of each parameter is illustrated in Figure 41. By increasing the gate delay, the measurement window is later and the intensity for hydrogen decreases. Therefore, a gate delay of 0.2 µs shows higher intensity than a gate delay of 1.2 µs. The width of the measurement window, also called gate width, delivers higher intensity when the width is increased. The last parameter, the intensifier gain is always optimized in the end, because every detector has a saturation limit and with that parameter a saturation can be avoided without losing information of the optimized measurement. Furthermore, using helium instead of argon showed better emissions for quantification of hydrogen and therefore better calibration curves.

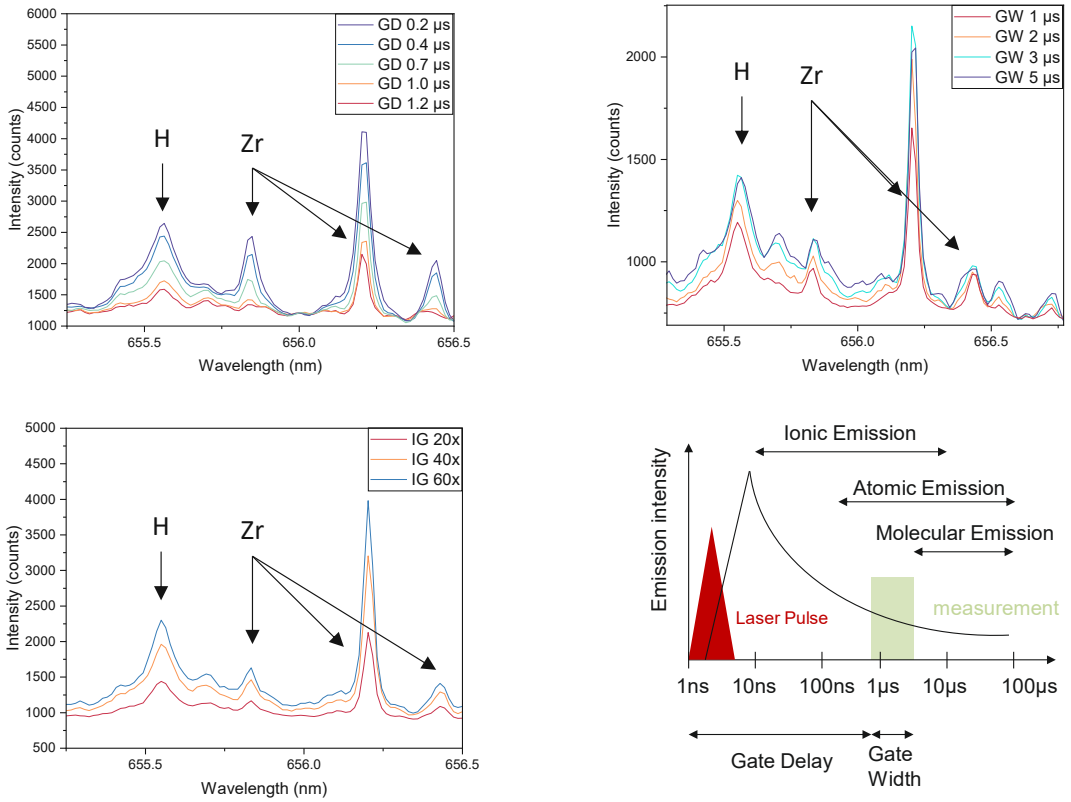

Figure 41: Laser-induced Breakdown Spectroscopy optimization for hydrogen quantification (first row: Variation of Gate Delay GD, Variation of Gate Width GW; second row: Variation of Intensifier Gain IG, schematic LIBS spectra and declaration of Gate Delay GD and Gate Width GW)

After optimization of each single parameter, the prepared $Zr(OH)_4$/BZY15 standards were measured with different combinations of gate delay and gate width and the background corrected, integrated intensity was connected to the hydrogen concentration. Every measurement led to a calibration curve and two of them were used for further quantification of hydrogen, which are visualized in Figure 42. The intensity and linear fit of the calibration, like the slope of the regression are deciding factors.

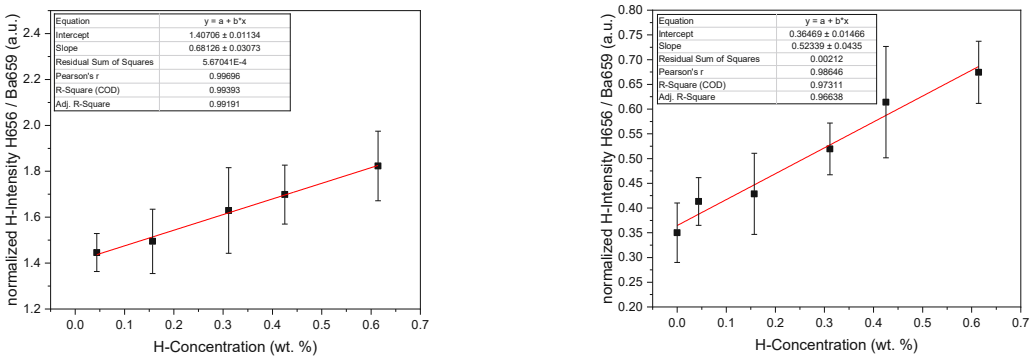

Figure 42: Calibration curves for hydrogen quantification by LIBS measurements (left: 5 standards, Gate Delay 0.7 µs, Gate Width: 5 µs; right: 5 standards and 1 blank standard, Gate Delay 1 µs, Gate Width 2 µs)

The points in the diagrams represent the mean and standard deviation of five measurements. And each measurement is already an averaged spectra from about 132 single spectra to

reduce noise. Furthermore, the hydrogen intensity is normalized to barium. The limit of detection (LOD) for both calibration curves were calculated by using the standard deviation of the first standard, multiplied by three and divided by the slope of the calibration curve. A LOD of 0.363 wt. % for the left calibration curve and 0.277 wt.% for the right calibration curve was determined. These limits of detection seem not to be good enough, but the preparation of less concentrated standards introduced higher standard deviations and therefore even worse LODs. These calibration curves are used, but the calculated concentrations must be critically discussed.

In general, for hydrogen quantification by LIBS measurements some further optimizations were done. Due to measuring hydrogen, the gas phase in the LIBS system needs to be dry, clean and tight as possible. Therefore, we used the tighter tandem chamber and after introducing the samples, the chamber is flushed for at least 30 minutes with dry argon to avoid measuring additional hydrogen due to a humidified gas phase.
For the LIBS measuring itself, a big pattern helped to compensate the inhomogeneity of the inhouse prepared standards. The pattern is illustrated in section 3.5, see Figure 16. Additionally, preablation helped to determine more stable hydrogen contents and therefore the first measurement was not included in the hydrogen quantification. This can be caused through adsorption or inhomogeneity at the surface.
Additionally, a high temperature chamber was used, to have the opportunity to heat the chamber and sample. This further improved to measure only the hydrogen content of the sample, but this has to be improved before applying in future.

A problem for hydrogen depth profiling is the caused heat while laser ablation which causes errors. The additional heat can evaporate hydrogen and therefore less hydrogen is erroneously quantified.
An idea was to increase the stage speed and reduce the spot size, so the heating while measuring is decreased. Furthermore, the pattern was increased to realise a more representive and steady signal.

4.4.1. Comparison of ex-situ and LIBS-measurements

One of the main targets of this thesis was to develop a method for determining the hydrogen amount by laser-induced breakdown spectroscopy. Therefore, the ex-situ experiments were compared to the laser-induced breakdown spectroscopy measurements, calibrated by the self-prepared $Zr(OH)_4$/BZY15 standards. We used the ex-situ samples instead of TGA samples, because the handling to measure LIBS directly after humidification in the ex-situ setup was easier and introduces less errors. Furthermore, once a TGA sample was mounted and a measurement worked, several following measurements with the same sample were done.

The higher hydrogen concentration of powder measurements in literature let us introduce the idea of manufacture small pieces of pressed and sintered powder of some millimetres, see “BZY15 pieces” in Figure 14 in chapter 3.2.
The manufactured BZY15 pieces were humidified, dried ex-situ and pieces were taken to analyse the hydrogen content by Laser-induced Breakdown Spectroscopy measurements. Therefore, the left calibration curve in Figure 42 was used to calculate the hydrogen concentration from the normalized intensity. Both bar charts are shown in Figure 43, on the left side the hydrogen concentration analysed by LIBS and on the right side the hydrogen concentration determined from the ex-situ measurements.

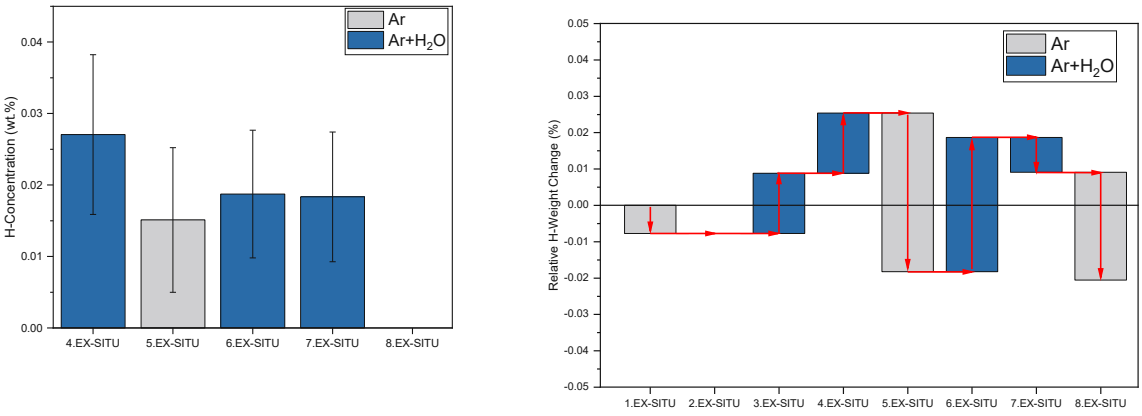

Figure 43: Humidification and drying of BZY15 pieces
(left: Laser-induced Breakdown Spectroscopy measurement of the hydrogen concentration due to left calibration curve in Figure 42; right: ex-situ weight changes corrected hydrogen concentration)

In general, the BZY15 pieces were dried (grey) in the first and second ex-situ experiment at 900°C for 20 h. The second drying step did not result in weight loss. All humidification steps include a treatment of humidified Argon at 550°C for 20 h, only the 4.EX-SITU experiment was at 450°C. Thermodynamics underline the higher water uptake at the lower temperature of 450°C. The humidification in the 3rd and 4th EX-SITU experiment result in higher hydrogen concentration compared to the other humidification. The sintering at temperatures about 1500°C introduced more oxygen vacancies and resulted in higher water uptake. The drying in the ex-situ furnace at 900°C is not complete and therefore the humidification results in smaller weight increase. The humidification steps, illustrated in blue bars show comparable hydrogen contents of the weight changes ex-situ and hydrogen concentrations by LIBS measurement. The 7.EX-SITU step was with humidified Argon, but a weight loss was registered. LIBS showed a decrease of the hydrogen concentration. A higher temperature due to a different

position of the sample in the furnace could explain loss of water and the resulting lower hydrogen concentration.

Additional to the LIBS measurements, X-ray diffraction Rietveld refinement allow an estimation of the crystallite size in the BZY15 pieces. For every humidification or drying step a crystallite size and estimated standard deviation (ESD) is listed in Figure 14.

Table 14: XRD refinement – Estimated crystallite size in HighScore

	Crystallite Size (Å)	Crystallite Size ESD (Å)
4.EX-SITU	671.7	1.478
5.EX-SITU	735.0	1.556
6.EX-SITU	882.1	0.980
7.EX-SITU	848.7	1.130
8.EX-SITU	825.4	0.960

For better visualization the estimated crystallite sizes and estimated standard deviation (ESD) are shown in Figure 44.

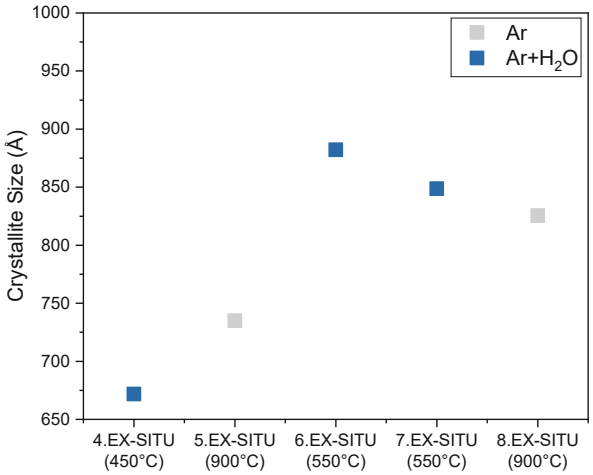

Figure 44: Estimated crystallite size of BZY15 pieces, XRD Rietveld refinement

The humidified steps of the 6. and 7. EX-SITU experiment show bigger crystallite sizes compared to the dried experiments. The crystallite size of the 4.EX-SITU experiment is smaller than the other. Han et al.[86] reported chemical expansion due to water uptake in the crystalline structure.

The comparison of the hydrogen concentration evaluated by ex-situ and LIBS measurements is shown in Figure 45. All thermogravimetric analysis and ex-situ results are referred to the sample weight and therefore the weight change in % is noted. In comparison, laser induced breakdown spectroscopy measurements deliver H-concentrations in wt. % by using the calibration curve of the self-prepared standards. To compare both results, the units can be transferred to each other by multiplying or dividing the factor of 2/18, the molecular weight portion of hydrogen in water. Furthermore, the error bars represent the uncertainty of the balance and for LIBS measurements the standard deviation was calculated by determining different laser patterns on different spots on the same sample.

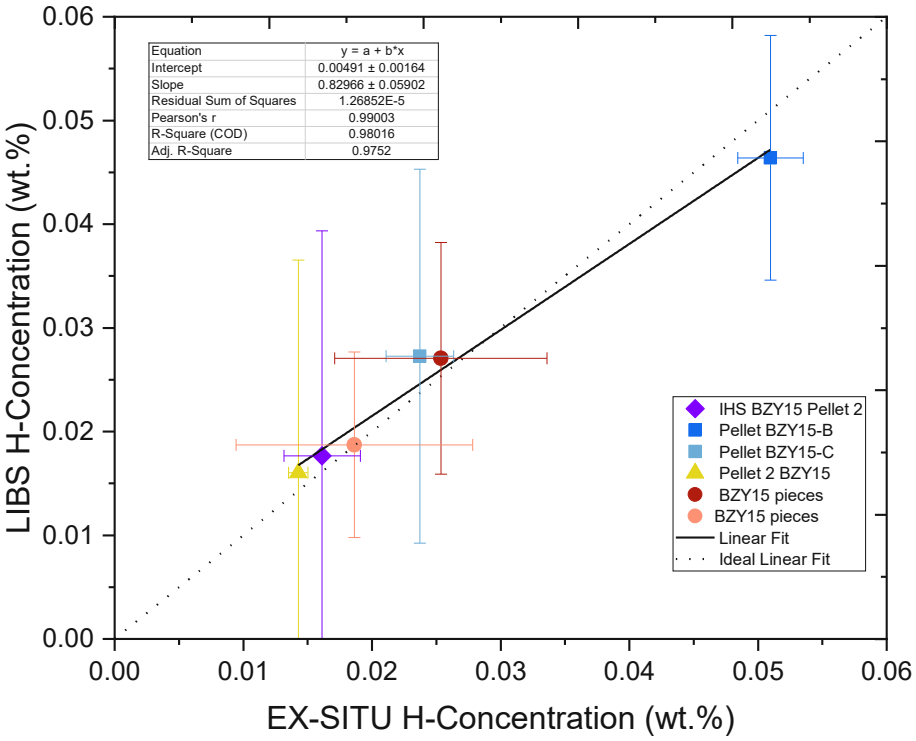

Figure 45: Comparison of ex-situ and LIBS-measurements

In general, the determination of the hydrogen concentration by LIBS is little higher than for the ex-situ experiments except the measurement of BZY15-B. This can be because of the calibration by self-prepared standards. In contradiction, the H-concentration of the sample BZY15-B is much higher compared to the other samples.
Due to the comparability of the TGA and ex-situ experiments, the LIBS measurements fit to the TGA experiments as well.

4.4.2. Preliminary results of depth profiling and diffusion profile of hydrogen

To analyse the water uptake in more detail, depth profiling and diffusion profiles of hydrogen help to understand the process of water incorporation in more detail. Here the pellet was dried ex-situ at 900°C and humidified for 90 seconds at 550°C.
A problem for hydrogen depth profiling is the created heat while laser ablation and therefore the stage speed was increased and the spot size was reduced. Furthermore, the pattern was increased to realise a more representive and steady signal. The experimental data is shown in Figure 46. Multiple laser pattern were measured to realise depth profiling. Here the level of hydrogen of the humidifed samples is higher than the dried sample BZY15-A. The humidification for the BZY15-B sample show a higher hydrogen signal than the BZY15-C sample.

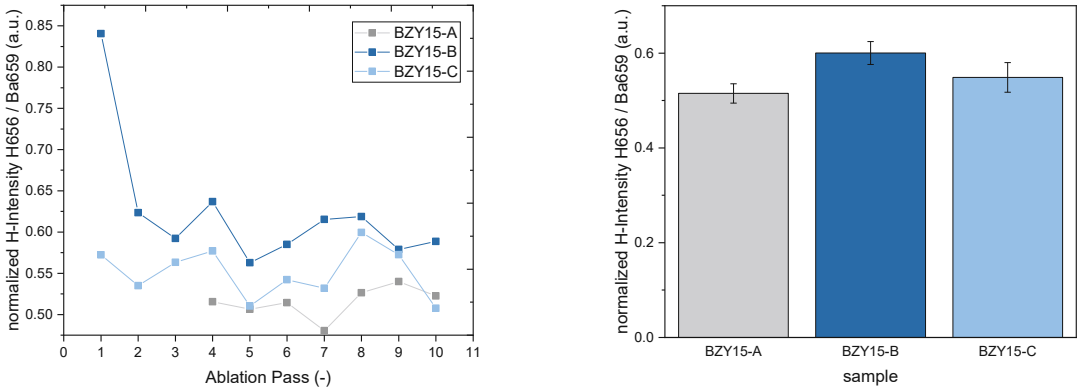

Figure 46: Depth profiling of hydrogen by laser-induced breakdown spectroscopy (left: normalized hydrogen intensity visualized over number of ablation pass on the same spot; right: comparison of the mean normalized intensity of humidified (blue) and dry (grey) samples.)

This type of depth profile measurement shows a disadvantage because every shot creates a profile with tilted walls and a rough surface. The following ablation pass targets the layer above as well due to the tilted walls which introduces a gradual error. Therefore, the strategy was changed to measure the depth profile on the cross section directly by lines parallel to the surface of humidification.

In our diffusion profile, the LIBS measurement was done on the cross section and laser line profiles were placed to determine the hydrogen content in dependence of diffusion depth. The diffusion profile of the pellet with a thickness of about 1.2 mm is shown in Figure 47. Here two maxima are visible. This occurs because the diffusion happened from both surfaces. The laser lines near the diffusion surfaces will introduce a higher content of hydrogen, which is due to adsorption. In the second line from the surface, the heating of the sample could set adsorbed water molecules of the diffusion surface free and these can be detected additionally. The other data points seem to be reliable. To see the effect of adsorbed water molecules on the cross section, three ablation passes were measured. The first ablation pass shows in general a higher hydrogen concentration, which can be probably referred to the adsorbed water. Some hydrogen concentrations are above the theoretical maximum water incorporation of BZY15, but till now it is not clear where this comes from.

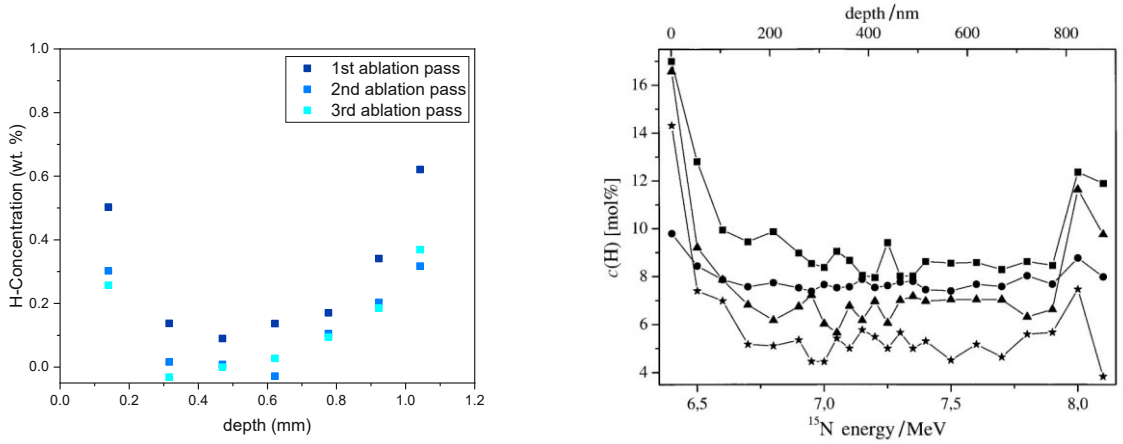

Figure 47: Hydrogen depth profile
(left: Diffusion profile of a 1.2 mm thick BZY15 pellet humidified for 90 s and hydrogen measured by LIBS and normalised by Ba-line at 659.5 nm ;
right: Hydrogen depth profile of 1 µm film samples charged at ■ 550°C, ● 600°C, ▲ 650°C, ★ 700°C and a constant water vapour pressure of 100 mbar.)

The hydrogen depth profile of Groß et al.[17] by nuclear resonance reaction analysis in Figure 47 shows two maxima. Here the sample were prepared by coating with a precursor solution and sintering for 12 h at 600°C, a sol-gel process. The water incorporation was done at different temperatures (550°C, 600°C, 650°C, 700°C) and a constant water vapour pressure of 100 mbar for 12 h. By quick cooling, the hydrogen the high temperature thermodynamic equilibrium was frozen. One maximum is on the sample surface and the other at the interface between the ceramic film and the substrate. The hydrogen content in between is approximately constant. The maximal possible hydrogen content of BZY15 is 15 mol%, which is exceeded on the surface in the measurements at 550 and 650°C, this can be due to additionally adsorbed water.

5. Conclusions

In this thesis the dopant concentration of yttrium in Y-doped barium zirconate is very important and therefore the yttrium concentration was determined by ICP-OES analysis. The purchased material showed the expected Y-concentration, but the self-synthesized BZY powder included only about 11 mol% Y, instead of 15 mol%. The phase identification by X-ray diffraction, allowed to make sure, that only the suspected phase of the material is responsible for water incorporation. In an alternative sample preparation approach, in which purchased BZY15 precursor powder was pressed and sintered to pellets, a loss of Ba and of the sintering aird NiO was observed. This was confirmed by laser-induced breakdown spectroscopy measurements of parts of the crucible in which the sintering process was conducted. A counter strategy to prevent this loss of material constituents was that the pellet was surrounded by precursor powder for the sintering step.

After first water incorporation experiments, the thermogravimetric analysis setup was optimized. The main optimization can be separated in two topics, improving the drying and humidification steps and stabilizing the balance measurements. The water saturated argon flushes the TGA and exits through the relief valve. In the beginning the water cooling above the furnace, which is required to protect the balance unit, was connected to the in-house water-cooling circle and therefore introduced about 12°C cold water. The strong cooling resulted in condensation of the water inside the apparatus. This impeded the fast change to dry argon gas phase for the next measurement. Therefore, the in-house cooling circuit was replaced by a cooling circuit at room temperature. Additionally, to speed up the drying process, the opportunity to setevacuate the TGA was applied by connecting a backing pump and a turbomolecular pump. With two pressure gauges the gas pressure is monitored and, furthermore, allows to find leaks. The second big optimization step is the stabilizing of the balance measurements. A new aluminium flange system with Viton® sealings helps to prevent leaks after operating at higher temperatures. Furthermore, the tightness is guaranteed by fixing the sealing with screws. A thermo shield above the sample mounting helps to decrease the stack effect and therefore reduces the turbulences at higher temperatures.

After finding the optimal TGA setup, a procedure for humidification and the optimal temperature for water incorporation of barium zirconate was searched. In all water incorporation experiments a strong interplay of diffusion limited kinetics and thermodynamic boundary conditions was noticed. For water uptake and release, diffusion is strongly dependent on the temperature, therefore higher temperatures accelerate the diffusion of OH into the ceramic. A higher water uptake is favoured at lower temperatures. Furthermore, in comparison to powder measurements, the longer diffusion required in case of measuring on macroscopic pellets is important and results in longer equilibration times. All these factors were considered to find the optimal temperature range.

Therefore, TGA measurements at decreasing temperatures steps revealed that BZY15 pellets show highest water uptake in the range of 500-700°C and ex-situ experiments helped to find the optimal temperature of 550°C. The in-house sintered BZY15 powder show highest water uptake at 400°C. The optimal TGA setup included a drying step at 800°C for 6 h under dry argon, a stabilization step at 550°C for 20 h under dry argon, a humidification step at 550°C under humidified argon for 24 h and cooling down to room temperature. To avoid effects of long equilibration times of the measurement atmosphere in the TGA apparatus, the humidification was done with higher gas flow (2.5 – 5 L/min).

In literature, Yamazaki et al.[16] predicted 0.135 % and Gonçalves et al.[15] 0.15 % weight change for BZY15 at 500°C, when applying a correction factor of 15/20 to the BZY20 results. Theoretically a water uptake of 0.492 % for BZY15 is possible if all oxygen vacancies are filled and for humidification at 550°C Groß et al.[17] predicted 9 mol %, which corresponds to a weight change of 0.295 %. Considering this scatter of slightly more than a factor of two, the data situation in the literature must be regarded rather critically.

Within the present experiments, a purchased BZY15 pellet showed a weight change of 0.1062 % (0.0118 wt. % H). For comparison, BZY15 pellets were also prepared in-house from a commercial precursor powder with the same sintering procedure as for the purchased pellet. This pellet was dried at sintering temperature and measured again. The weight change of 0.1420 % (0.0157 wt. % H) and 0.2872 % (0.0319 wt. % H) after additional drying showed a strong dependency of the drying procedure, thus being a possible explanation for the rather high scatter of water uptake reported in literature. From the experimental data reported here, it can be concluded that for pellets a drying step performed at 800°C is not high enough to reproducibly measure the water incorporation into BZY-type ceramics. Therefore, the samples need to be dried at elevated temperatures ex-situ and subsequently humidified in the TGA, because the TGA restricts the temperature to about 800°C due to the used gaskets. Ex-situ experiments also had the advantage of saving time due to the faster changing of samples and due to the opportunity to prepare more samples at the same time. The results of the ex-situ experiments are comparable to the TGA results and an almost ideal linear relationship between TGA and ex-situ results was obtained.

The second main part of this thesis was the quantification of hydrogen by laser-induced breakdown spectroscopy. For hydrogen measurements, it was important to measure in a dry and clean chamber that was ensured by flushing the chamber for 30 minutes before LIBS measurements. Furthermore, measuring hydrogen under helium flow instead of argon increased the emission intensity, which resulted in better calibration curves. For hydrogen calibration, matrix matched standards were prepared by ball milling and pelletisation. Two calibration curves with optimized gate delay and gate width were used for further quantification of hydrogen. Here it was important to use a big laser pattern to avoid errors due to inhomogeneity in the standards. Furthermore, the first ablation pass was not used for the hydrogen quantification to prevent measuring adsorbed water. ex-situ humidification allows to quickly transport the sample to the LIBS setup directly after humidification to analyse the hydrogen concentration. The comparison of proton concentrations in BZY-based ceramics obtained by measuring the mass difference upon water incorporation and LIBS show almost a perfectly linear relationship with a slope very close to one. Only at higher hydrogen concentrations the LIBS measurements yield a slightly lower hydrogen content in comparison to ex-situ experiments. Due to the linear connection between TGA and ex-situ and secondly between ex-situ and LIBS, it can further be concluded that a good agreement between TGA results and LIBS hydrogen measurements was found.

Additionally, due to the importance of hydrogen diffusion, first preliminary measurements of depth profiles were performed by LIBS. Two different implementations were analysed. Firstly, measuring of the humidified surface by laser ablation passes on the same spot. Here the difference between dried and humidified sample was shown. The second implementation included the humidification, cutting of the sample and measuring on the cross section. This resulted in a depth profile of hydrogen with maxima at each surface and decreasing hydrogen concentration to the middle of the sample. This confirmed the hydrogen diffusion from both sides, but more research and experiments are needed to optimize the hydrogen depth profiling.

6. Outlook

6.1. Optimization of the used techniques and prevention of errors

Thermogravimetric analysis

The progress of the TGA setup was already described in section 4.2. Here notes and advice for further TGA measurements are given.

If something happens unregularly in a TGA, it is often not easy to find the origin of error. Often the apparatus can be leaky, which introduces more fluctuations and a higher noise in the balance data. To make sure this is the origin, the apparatus can be pumped down to vacuum and if it is not possible to go down to a reasonably low pressure level one has found the issue. In our system often the glass tube and the flange connection with sealings were leaky. If sealings get too hot, the plastic decomposes or gets a rough surface and the system becomes leaky. A change of the sealings will help. In the beginning of the thesis, the connection between glass and metal flanges were done by ceramic glue or two-components glue and after a longer period at higher temperatures and some stresses, leaks appeared. Adding alcohol on these places upon evacuating the tube can show if the pressure rises from vacuum fast and indicates that the system is leaky. To prevent this origin of error, the connection was changed to an aluminium flange and implemented Viton® sealings. Viton® allows temperatures of about 200°C and the leak tightness is guaranteed by using screws in the aluminium flange system to tighten the sealing with the same force all over the sealing surface.

A further problem can be the radiation shield. If rings are loose, they can vibrate in the stream of gas and introduce further noise to the balance. Electrostatic forces have to be limited, therefore a Kanthal® wire was winded around the glass tube and was grounded. Heating up with a small handheld torch can also help to get rid of electrostatic forces. A bigger distance of the platinum wire hook and glass radiation shield decreases these forces.
Another important point is the thermic insulation. When the noise increases dramatically at higher temperatures this can be the problem. We used fiberglass to insulate the glass tube at the ends of the furnace, so axial diffusion is limited. The stack effect [87] is when the hot air streams to the top due to its lower density. This introduces negative pressure and sucks air and this may introduce noise.

Lastly the TGA setup was optimized to be tight by changing how to change the sample. To save time, the flange connection and the whole glass tube stays in place and only by opening the flange, where the thermocouple is introduced, the sample is mounted by a bar and a handling tool. The main advantage is that all elements stay in the same place and therefore the tightness of the apparatus and the correctness of the measurement stays the same. No additional optimizing by adjusting the radiation shield, glass tube or even the sealings is necessary.

Laser induced breakdown spectroscopy

The main advice for hydrogen measurements is to find the best parameters with the material which is measured in the end. Standards created by yourself may not include all of the elements, which are included in the sample and therefore create emission or in the worst-case overlapping emissions. This can introduce little changes in the best parameters for the LIBS measurement. In general, standards prepared by mixing and grinding in a ball mill show better homogeneity than by mixing in a mortar. Here it is important to use a material for balls and housing that will not influence your quantification. Secondly at the beginning of hydrogen measurements the chamber needs to be flushed, so no additional water content is inside and creates additional hydrogen emission intensity. By using helium instead of argon, the hydrogen emission was more intense, and the calibration curves were better. The first shots on a surface should not be included to the determination of the hydrogen content of the sample, because this includes adsorbed water molecules and leads to a higher predicted concentration.

7. Appendix

Table 15: List of used ICP Standard solutions.

Name	Compound	Product Nr.	Concentration ± 2k (µg/mL)	Company
Zirkonium ICP Standard	NIST $ZrOCl_2$ in 7 % HCl	1.70370.0100	963 ± 5	Merck KGaA
Barium Standard for ICP	Ba in 2% HNO_3	101166324	1000 ± 2	Fluka Analytical
Yttrium ICP standard	$Y(NO_3)_3$ in HNO3 2-3 %	1.70368.0100	988 ± 6	Merck KGaA
Cerium, plasma standard solution	Ce in 5 % HNO_3	13815	978 ± 3	Alfa Aesar
Chromium standard solution	$CrCl_3$ in HCl	9948	2000 ± 3	Merck KGaA
Indium ICP standard	$In(NO_3)_3$ in 2-3 %HNO_3	1.70324.0100	986 ± 5	Merck KGaA
Europium, plasma standard solution	Eu_2O_3 in 5 % HNO_3	35753	992 ± 5	Alfa Aesar
Hafnium, plasma standard solution	$HfCl_2O$ in 5 % HCl	13843	1003 ± 5	Alfa Aesar
Nickel ICP standard	NIST Ni $(NO_3)_2$ in 2-3 % HNO3	1.70336.0100	988 ± 3	Merck KGaA

Table 16: List of all TGA measurements. Program notation for each temperature in °C (d=dry argon, w= humidified argon)

TGA	Sample	Program	Ar-Flow (sccm)
1	BZCY81-TGA1	800d_400d_400w_800w_0d	20
2	BZCY81-TGA1	0w_800w_800d_800w_700w_600w_500w_400w_300w_200w_100w	40
3	BZCY81-TGA1	0w_700w_700d_700w	40
4	BZCY81-TGA1	700d_700w_700w_600w_500w_400w_300w_200w_100w_0w	40
5	BZCY81-TGA1	0w_100w_200w_300w_400w_500w_600w_700w	40
6	BZCY81-TGA1	700w_200w_0w_open	40
7	BZY15-Powder	0d_400d_400w	40
8	BZY15-Powder	400w_800d_400d_400w	40
9	BZY15-TGA2	800d_400d_400w_0w	20
10	BZCY81-TGA3	800d_400d_400w_0w	20
11	BZCY81-TGA3	400w_800w_700w_600w_500w_400w_300w_200w	20
12	BZCY81-TGA3	0d_vac_800d_700d_600d_500d_400d_300d_200d_100d_0d	20
13	BZCY81-TGA3	0d_800d_800w_700w_600w_500w_400w_300w_200w_100w_0w	20
14	BZCY81-TGA3	23vac_1000vac_1000d_1000w_900w_800w_700w_600w_500w_400w_300w_200w_100w_0w	20
15	BZCY81-TGA3	23vac_1000vac_1000d_900d_800d_700d_600d_500d_400d_300d_200d_100d_0d	20
16	BZCY81-TGA3	23vac_1000vac_1000d_1000w_900w_800w_700w_600w_500w_400w_300w_200w_100w_0w	20
17	BZY15-pieces	0w_590w	20
18	BZY15-C	600d	20
19	BZY15-Da	600d_600w_0w	20
20	BZY15-Da	830d_590d	20
21	BZY15-Da	830d_590d_590w_0w	20
22	BZY15-B	830d_590d_590w_0w	20
23	Quartz-A	830d_590d_590w_0w	20
24	Quartz-A	830d_590d_590w_0w	20
25	Quartz-A	830d_590d_590w_0w	20
26	IHS BZY15 Pellet 1	830d_590d	20
27	IHS BZY15 Pellet 1	830d_590d_590w_0w	20
28	Quartz-A	830d_590d_590w_0w	20
29	IHS BZY15 Pellet 1	830d_590d_590w_830d_590d_590w_830d	20
30	IHS BZY15 Pellet 1	830d_830w_735w_632w_529w_425w_320w_214w_108w_0w	20
31	IHS BZY15 Pellet 1	830d_830w_735w_632w_529w_425w_320w_214w_108w_0w (two times measured)	20
32	IHS BZY15 Powder	835d_594d_594w_594d_835d_594d_594w(9 min. 2.5L/min, 20 sccm)_0w_835d_835w(5 min. 5L/Min, 20sccm)_739w_636w_533w_428w_322w_216w_109w_0w_0d	20
33	Sintered IHS BZY15 Pellet 3	835d_640d_640w(5 min 5L/min, 20 sccm)_0w	20

List of References

[1] J. O. Abe, A. P. I. Popoola, E. Ajenifuja, and O. M. Popoola, 'Hydrogen energy, economy and storage: Review and recommendation', *Int. J. Hydrog. Energy*, vol. 44, no. 29, pp. 15072–15086, Jun. 2019, doi: 10.1016/j.ijhydene.2019.04.068.

[2] A. Züttel, A. Remhof, A. Borgschulte, and O. Friedrichs, 'Hydrogen: the future energy carrier', *Philos. Trans. R. Soc. Math. Phys. Eng. Sci.*, vol. 368, no. 1923, pp. 3329–3342, Jul. 2010, doi: 10.1098/rsta.2010.0113.

[3] E. Crawford, 'Arrhenius' 1896 Model of the Greenhouse Effect in Context', *Ambio*, vol. 26, no. 1, pp. 6–11, 1997.

[4] European Commission, *Hydrogen energy and fuel cells: a vision of our future*. Luxembourg: Office for Official Publications of the European Communities, 2003.

[5] H. T. Hwang and A. Varma, 'Hydrogen storage for fuel cell vehicles', *Curr. Opin. Chem. Eng.*, vol. 5, pp. 42–48, Aug. 2014, doi: 10.1016/j.coche.2014.04.004.

[6] O. Z. Sharaf and M. F. Orhan, 'An overview of fuel cell technology: Fundamentals and applications', *Renew. Sustain. Energy Rev.*, vol. 32, pp. 810–853, Apr. 2014, doi: 10.1016/j.rser.2014.01.012.

[7] N. L. R. M. Rashid *et al.*, 'Review on zirconate-cerate-based electrolytes for proton-conducting solid oxide fuel cell', *Ceram. Int.*, vol. 45, no. 6, pp. 6605–6615, Apr. 2019, doi: 10.1016/j.ceramint.2019.01.045.

[8] L. Yan, W. Sun, L. Bi, S. Fang, Z. Tao, and W. Liu, 'Effect of Sm-doping on the hydrogen permeation of Ni–La2Ce2O7 mixed protonic–electronic conductor', *Int. J. Hydrog. Energy*, vol. 35, no. 10, pp. 4508–4511, May 2010, doi: 10.1016/j.ijhydene.2010.02.134.

[9] K. D. Kreuer, 'Proton-Conducting Oxides', *Annu. Rev. Mater. Res.*, vol. 33, no. 1, pp. 333–359, Aug. 2003, doi: 10.1146/annurev.matsci.33.022802.091825.

[10] K. D. Kreuer, St. Adams, W. Münch, A. Fuchs, U. Klock, and J. Maier, 'Proton conducting alkaline earth zirconates and titanates for high drain electrochemical applications', *Solid State Ion.*, vol. 145, no. 1–4, pp. 295–306, Dec. 2001, doi: 10.1016/S0167-2738(01)00953-5.

[11] J. M. Polfus, T. S. Bjørheim, T. Norby, and R. Bredesen, 'Surface defect chemistry of Y-substituted and hydrated $BaZrO_3$ with subsurface space-charge regions', *J. Mater. Chem. A*, vol. 4, no. 19, pp. 7437–7444, 2016, doi: 10.1039/C6TA02067D.

[12] Y. Yamazaki, R. Hernandez-Sanchez, and S. M. Haile, 'High Total Proton Conductivity in Large-Grained Yttrium-Doped Barium Zirconate', *Chem. Mater.*, vol. 21, no. 13, pp. 2755–2762, Jul. 2009, doi: 10.1021/cm900208w.

[13] D. Pergolesi *et al.*, 'High proton conduction in grain-boundary-free yttrium-doped barium zirconate films grown by pulsed laser deposition', *Nat. Mater.*, vol. 9, no. 10, pp. 846–852, Oct. 2010, doi: 10.1038/nmat2837.

[14] E. Fabbri, D. Pergolesi, S. Licoccia, and E. Traversa, 'Does the increase in Y-dopant concentration improve the proton conductivity of BaZr1−xYxO3−δ fuel cell electrolytes?', *Solid State Ion.*, vol. 181, no. 21–22, pp. 1043–1051, Jul. 2010, doi: 10.1016/j.ssi.2010.06.007.

[15] M. D. Gonçalves, A. Mielewczyk-Gryń, P. S. Maram, Ł. Kryścio, M. Gazda, and A. Navrotsky, 'Systematic Water Uptake Energetics of Yttrium-Doped Barium Zirconate—A High Resolution Thermochemical Study', *J. Phys. Chem. C*, vol. 124, no. 21, pp. 11308–11316, May 2020, doi: 10.1021/acs.jpcc.0c01049.

[16] Y. Yamazaki, P. Babilo, and S. M. Haile, 'Defect Chemistry of Yttrium-Doped Barium Zirconate: A Thermodynamic Analysis of Water Uptake', *Chem. Mater.*, vol. 20, no. 20, pp. 6352–6357, Oct. 2008, doi: 10.1021/cm800843s.

[17] B. Groß and R. Hempelmann, 'Dissociative water vapour absorption in BaZr0.85Y0.15O2.925/H2O: pressure-compositions isotherms in terms of Fermi-Dirac statistics', p. 5, Nov. 1999.

[18] H. G. Bohn and T. Schober, 'Electrical Conductivity of the High-Temperature Proton Conductor BaZr0.9Y0.1O2.95', *J. Am. Ceram. Soc.*, vol. 83, no. 4, pp. 768–772, Dec. 2004, doi: 10.1111/j.1151-2916.2000.tb01272.x.
[19] K. D. Kreuer, 'Aspects of the formation and mobility of protonic charge carriers and the stability of perovskite-type oxides', *Solid State Ion.*, vol. 125, no. 1–4, pp. 285–302, Oct. 1999, doi: 10.1016/S0167-2738(99)00188-5.
[20] M. D. McCluskey, S. J. Jokela, and K. K. Zhuravlev, 'Infrared spectroscopy of hydrogen in ZnO', p. 4, Nov. 2002.
[21] H. Iwahara, T. Yajima, T. Hibino, K. Ozaki, and H. Suzuki, 'Protonic conduction in calcium, strontium and barium zirconates', p. 5, 1993.
[22] K. J. Alvine, M. Tyagi, C. M. Brown, T. J. Udovic, T. Jenkins, and S. G. Pitman, 'Hydrogen species motion in piezoelectrics: A quasi-elastic neutron scattering study', *J. Appl. Phys.*, vol. 111, no. 5, p. 053505, Mar. 2012, doi: 10.1063/1.3691114.
[23] C. Foo *et al.*, 'Importance of Hydrogen Migration in Catalytic Ammonia Synthesis over Yttrium-Doped Barium Zirconate-Supported Ruthenium Nanoparticles: Visualization of Proton Trap Sites', *J. Phys. Chem. C*, vol. 125, no. 42, pp. 23058–23070, Oct. 2021, doi: 10.1021/acs.jpcc.1c04002.
[24] P. Babilo, 'Processing and Characterization of Proton Conducting Yttrium Doped Barium Zirconate for Solid Oxide Fuel Cell Applications', p. 69, 2007.
[25] F. A. Stevie, C. Zhou, M. Hopstaken, M. Saccomanno, Z. Zhang, and A. Turansky, 'SIMS measurement of hydrogen and deuterium detection limits in silicon: Comparison of different SIMS instrumentation', *J. Vac. Sci. Technol. B Nanotechnol. Microelectron. Mater. Process. Meas. Phenom.*, vol. 34, no. 3, p. 03H103, May 2016, doi: 10.1116/1.4940151.
[26] T. Stephan, 'TOF-SIMS in cosmochemistry', *Planet. Space Sci.*, vol. 49, no. 9, pp. 859–906, Aug. 2001, doi: 10.1016/S0032-0633(01)00037-X.
[27] D. Han, K. Shinoda, S. Sato, M. Majima, and T. Uda, 'Correlation between electroconductive and structural properties of proton conductive acceptor-doped barium zirconate', *J. Mater. Chem. A*, vol. 3, no. 3, pp. 1243–1250, 2015, doi: 10.1039/C4TA05701E.
[28] D. Han, S. Uemura, C. Hiraiwa, M. Majima, and T. Uda, 'Detrimental Effect of Sintering Additives on Conducting Ceramics: Yttrium-Doped Barium Zirconate', *ChemSusChem*, vol. 11, no. 23, pp. 4102–4113, Dec. 2018, doi: 10.1002/cssc.201801837.
[29] D. Han, X. Liu, T. S. Bjørheim, and T. Uda, 'Yttrium-Doped Barium Zirconate-Cerate Solid Solution as Proton Conducting Electrolyte: Why Higher Cerium Concentration Leads to Better Performance for Fuel Cells and Electrolysis Cells', *Adv. Energy Mater.*, vol. 11, no. 8, p. 2003149, Feb. 2021, doi: 10.1002/aenm.202003149.
[30] Y. Yamazaki, C.-K. Yang, and S. M. Haile, 'Unraveling the defect chemistry and proton uptake of yttrium-doped barium zirconate', *Scr. Mater.*, vol. 65, no. 2, pp. 102–107, Jul. 2011, doi: 10.1016/j.scriptamat.2010.12.034.
[31] Y. Yamazaki, A. Kuwabara, J. Hyodo, Y. Okuyama, C. A. J. Fisher, and S. M. Haile, 'Oxygen Affinity: The Missing Link Enabling Prediction of Proton Conductivities in Doped Barium Zirconates', *Chem. Mater.*, vol. 32, no. 17, pp. 7292–7300, Sep. 2020, doi: 10.1021/acs.chemmater.0c01869.
[32] Y. Yamazaki *et al.*, 'Proton trapping in yttrium-doped barium zirconate', *Nat. Mater.*, vol. 12, no. 7, pp. 647–651, Jul. 2013, doi: 10.1038/nmat3638.
[33] E. Rebollo *et al.*, 'Exceptional hydrogen permeation of all-ceramic composite robust membranes based on BaCe0.65Zr0.20Y0.15O3ÀÐ and Y- or Gd-doped ceria', *Environ. Sci.*, p. 12, 2015.
[34] G. Galbács, A. Kéri, I. Kálomista, É. Kovács-Széles, and I. B. Gornushkin, 'Deuterium analysis by inductively coupled plasma mass spectrometry using polyatomic species: An experimental study supported by plasma chemistry modeling', *Anal. Chim. Acta*, vol. 1104, pp. 28–37, Apr. 2020, doi: 10.1016/j.aca.2020.01.011.
[35] D. W. Hahn and N. Omenetto, 'Laser-Induced Breakdown Spectroscopy (LIBS), Part I: Review of Basic Diagnostics and Plasma—Particle Interactions: Still-Challenging Issues

within the Analytical Plasma Community', *Appl. Spectrosc.*, vol. 64, no. 12, pp. 335A-336A, Dec. 2010, doi: 10.1366/000370210793561691.
[36] S. Smetaczek, 'Investigation of stabilized Li7La2Zr3O12 garnets by combining electrochemical measurements with chemical analysis', p. 112, Jun. 2021.
[37] F. Giannici, M. Shirpour, A. Longo, A. Martorana, R. Merkle, and J. Maier, 'Long-Range and Short-Range Structure of Proton-Conducting Y:BaZrO $_3$', *Chem. Mater.*, vol. 23, no. 11, pp. 2994–3002, Jun. 2011, doi: 10.1021/cm200682d.
[38] M. M. Welander, D. J. Goettlich, T. J. Henning, and R. A. Walker, 'Yttria-stabilized barium zirconate surface reactivity at elevated temperatures', *MRS Commun.*, vol. 10, no. 3, pp. 455–460, Sep. 2020, doi: 10.1557/mrc.2020.43.
[39] M. Karlsson, I. Ahmed, A. Matic, and S. G. Eriksson, 'Short-range structure of proton-conducting BaM0.10Zr0.90O2.95 (M=Y, In, Sc and Ga) investigated with vibrational spectroscopy', *Solid State Ion.*, vol. 181, no. 3–4, pp. 126–129, Feb. 2010, doi: 10.1016/j.ssi.2009.03.020.
[40] M. Karlsson, A. Matic, C. S. Knee, I. Ahmed, S. G. Eriksson, and L. Börjesson, 'Short-Range Structure of Proton-Conducting Perovskite BaIn $_x$ Zr $_{1-x}$ O $_{3-x/2}$ (x = 0−0.75)', *Chem. Mater.*, vol. 20, no. 10, pp. 3480–3486, May 2008, doi: 10.1021/cm7025448.
[41] J. D. Holladay, J. Hu, D. L. King, and Y. Wang, 'An overview of hydrogen production technologies', *Catal. Today*, vol. 139, no. 4, pp. 244–260, Jan. 2009, doi: 10.1016/j.cattod.2008.08.039.
[42] A. Steinfeld and R. Palumbo, 'Solar Thermochemical Process Technology', p. 22, 2001.
[43] E. D. Wachsman and K. T. Lee, 'Lowering the Temperature of Solid Oxide Fuel Cells', *Science*, vol. 334, no. 6058, pp. 935–939, Nov. 2011, doi: 10.1126/science.1204090.
[44] P. Sharma, 'Chapter 1. Proton exchange membrane fuel cells: fundamentals, advanced technologies, and practical applications', *Adv. Technol.*, p. 24, 2022.
[45] Z. Tao, L. Yan, J. Qiao, B. Wang, L. Zhang, and J. Zhang, 'A review of advanced proton-conducting materials for hydrogen separation', *Prog. Mater. Sci.*, vol. 74, pp. 1–50, Oct. 2015, doi: 10.1016/j.pmatsci.2015.04.002.
[46] D. G. Thomas and J. J. Lander, 'Hydrogen as a Donor in Zinc Oxide', p. 8, Oct. 2004.
[47] J. M. Pope, 'The use of BaTiO as a solid-electrolyte to determine water vapor effects upon electrical transport mechanisms', vol. 9, no. 9, p. 7, 1974.
[48] H. Iwahara, T. Yajima, T. Hibino, K. Ozaki, and H. Suzuki, 'Protonic conduction in calcium, strontium and barium zirconates', *Solid State Ion.*, vol. 61, no. 1–3, pp. 65–69, May 1993, doi: 10.1016/0167-2738(93)90335-Z.
[49] R. J. D. Tilley, *Perovskites: Structure-Property Relationships*. Chichester, UK: John Wiley & Sons, Ltd, 2016. doi: 10.1002/9781118935651.
[50] M. K. Hossain *et al.*, 'Recent progress in barium zirconate proton conductors for electrochemical hydrogen device applications: A review', *Ceram. Int.*, vol. 47, no. 17, pp. 23725–23748, Sep. 2021, doi: 10.1016/j.ceramint.2021.05.167.
[51] M. L. Ferreira Nascimento, 'Determination of Mobility and Charge Carriers Concentration from Ionic Conductivity in Sodium Germanate Glasses above and below T g', *ISRN Electrochem.*, vol. 2013, pp. 1–10, Feb. 2013, doi: 10.1155/2013/240571.
[52] H. Iwahara, 'Proton conducting ceramics and their applications', *Solid State Ion.*, vol. 86–88, pp. 9–15, Jul. 1996, doi: 10.1016/0167-2738(96)00087-2.
[53] R. Hempelmann, 'Muon diffusion and trapping in proton conducting oxides', *Solid State Ion.*, vol. 107, no. 3–4, pp. 269–280, Apr. 1998, doi: 10.1016/S0167-2738(97)00543-2.
[54] M. Pionke, T. Mono, W. Schweika, T. Springer, and H. Schober, 'Investigation of the hydrogen mobility in a mixed perovskite: Ba[Ca(1+x)/3Nb(2−x)/3]O3−x/2 by quasielastic neutron scattering', *Solid State Ion.*, vol. 97, no. 1–4, pp. 497–504, May 1997, doi: 10.1016/S0167-2738(97)00077-5.
[55] F. A. Kröger and H. J. Vink, 'Relations between the Concentrations of Imperfections in Crystalline Solids', in *Solid State Physics*, vol. 3, F. Seitz and D. Turnbull, Eds. Academic Press, 1956, pp. 307–435. doi: 10.1016/S0081-1947(08)60135-6.
[56] J. Tong, D. Clark, M. Hoban, and R. O'Hayre, 'Cost-effective solid-state reactive sintering method for high conductivity proton conducting yttrium-doped barium zirconium

ceramics', *Solid State Ion.*, vol. 181, no. 11–12, pp. 496–503, Apr. 2010, doi: 10.1016/j.ssi.2010.02.008.
[57] D. Gao and R. Guo, 'Structural and electrochemical properties of yttrium-doped barium zirconate by addition of CuO', *J. Alloys Compd.*, vol. 493, no. 1–2, pp. 288–293, Mar. 2010, doi: 10.1016/j.jallcom.2009.12.082.
[58] T. Schober, 'Water vapor solubility and electrochemical characterization of the high temperature proton conductor BaZr0.9Y0.1O2.95', *Solid State Ion.*, vol. 127, no. 3–4, pp. 351–360, Jan. 2000, doi: 10.1016/S0167-2738(99)00283-0.
[59] J. Bu, P. G. Jönsson, and Z. Zhao, 'Ionic conductivity of dense BaZr0.5Ce0.3Ln0.2O3−δ (Ln = Y, Sm, Gd, Dy) electrolytes', *J. Power Sources*, vol. 272, pp. 786–793, Dec. 2014, doi: 10.1016/j.jpowsour.2014.09.056.
[60] P. Sawant, S. Varma, B. N. Wani, and S. R. Bharadwaj, 'Synthesis, stability and conductivity of BaCe0.8−xZrxY0.2O3−δ as electrolyte for proton conducting SOFC', *Int. J. Hydrog. Energy*, vol. 37, no. 4, pp. 3848–3856, Feb. 2012, doi: 10.1016/j.ijhydene.2011.04.106.
[61] J.-S. Kim, J.-H. Yang, B.-K. Kim, and Y.-C. Kim, 'Proton conduction at BaO-terminated (001) BaZrO3 surface using density functional theory', *Solid State Ion.*, vol. 275, pp. 19–22, Jul. 2015, doi: 10.1016/j.ssi.2015.03.021.
[62] T. He, 'Impedance spectroscopic study of thermodynamics and kinetics of a Gd-doped BaCeO3 single crystal', *Solid State Ion.*, vol. 95, no. 3–4, pp. 301–308, Mar. 1997, doi: 10.1016/S0167-2738(96)00613-3.
[63] N. Bonanos, 'Transport properties and conduction mechanism in high-temperature protonic conductors', *Solid State Ion.*, vol. 53–56, pp. 967–974, Jul. 1992, doi: 10.1016/0167-2738(92)90278-W.
[64] D. Hu *et al.*, 'High-performance protonic ceramic fuel cell cathode using protophilic mixed ion and electron conducting material', *J. Mater. Chem. A*, vol. 10, no. 5, pp. 2559–2566, 2022, doi: 10.1039/D1TA07113K.
[65] A. Lesnichyova *et al.*, 'Water Uptake and Transport Properties of La1−xCaxScO3−α Proton-Conducting Oxides', *Materials*, vol. 12, no. 14, p. 2219, Jul. 2019, doi: 10.3390/ma12142219.
[66] K. D. Kreuer and S. Adams, 'Proton conducting alkaline earth zirconates and titanates for high drain electrochemical applications', p. 12, 2001.
[67] T. Schober, 'Water vapor solubility and electrochemical characterization of the high temperature proton conductor BaZr0.9Y0.1O2.95', *Solid State Ion.*, vol. 127, no. 3–4, pp. 351–360, Jan. 2000, doi: 10.1016/S0167-2738(99)00283-0.
[68] A. W. Coats and J. P. Redfern, 'Thermogravimetric analysis. A review', *The Analyst*, vol. 88, no. 1053, p. 906, 1963, doi: 10.1039/an9638800906.
[69] N. Saadatkhah *et al.*, 'Experimental methods in chemical engineering: Thermogravimetric analysis—TGA', *Can. J. Chem. Eng.*, vol. 98, no. 1, pp. 34–43, Jan. 2020, doi: 10.1002/cjce.23673.
[70] NETZSCH, 'TG 209 F3 Tarsus® Thermogravimetric Analysis – TGA Method, Technique and Applications'. [Online]. Available: https://analyzing-testing.netzsch.com/en/products/thermogravimetric-analysis-tga-thermogravimetry-tg/tg-209-f3-tarsus
[71] ELTRA, 'ELTRA TGA Thermostep - Thermogravimetric analyzer'. [Online]. Available: https://www.eltra.com/de/produkte/thermische-analysatoren/tga-thermostep/
[72] S. N. Thakur and J. P. Singh, *Laser-Induced Breakdown Spectroscopy*. Elsevier, 2020. doi: 10.1016/B978-0-12-818829-3.00001-0.
[73] S. Musazzi and U. Perini, Eds., *Laser-Induced Breakdown Spectroscopy: Theory and Applications*, vol. 182. Berlin, Heidelberg: Springer Berlin Heidelberg, 2014. doi: 10.1007/978-3-642-45085-3.
[74] V. Motto-Ros *et al.*, 'Critical aspects of data analysis for quantification in laser-induced breakdown spectroscopy', *Spectrochim. Acta Part B At. Spectrosc.*, vol. 140, pp. 54–64, Feb. 2018, doi: 10.1016/j.sab.2017.12.004.

[75] I. V. Cravetchi, M. T. Taschuk, Y. Y. Tsui, and R. Fedosejevs, 'Evaluation of femtosecond LIBS for spectrochemical microanalysis of aluminium alloys', *Anal. Bioanal. Chem.*, vol. 385, no. 2, pp. 287–294, May 2006, doi: 10.1007/s00216-005-0287-z.
[76] R. Russo, 'Laser ablation in analytical chemistry—a review', *Talanta*, vol. 57, no. 3, pp. 425–451, May 2002, doi: 10.1016/S0039-9140(02)00053-X.
[77] S. N. Thakur and J. P. Singh, 'Fundamentals of LIBS and recent developments', in *Laser-Induced Breakdown Spectroscopy*, Elsevier, 2020, pp. 3–22. doi: 10.1016/B978-0-12-818829-3.00001-0.
[78] H. J. van der Meiden *et al.*, 'Monitoring of tritium and impurities in the first wall of fusion devices using a LIBS based diagnostic', *Nucl. Fusion*, vol. 61, no. 12, p. 125001, Dec. 2021, doi: 10.1088/1741-4326/ac31d6.
[79] C. Li, C.-L. Feng, H. Y. Oderji, G.-N. Luo, and H.-B. Ding, 'Review of LIBS application in nuclear fusion technology', *Front. Phys.*, vol. 11, no. 6, p. 114214, Dec. 2016, doi: 10.1007/s11467-016-0606-1.
[80] J. El Haddad, L. Canioni, and B. Bousquet, 'Good practices in LIBS analysis: Review and advices', *Spectrochim. Acta Part B At. Spectrosc.*, vol. 101, pp. 171–182, Nov. 2014, doi: 10.1016/j.sab.2014.08.039.
[81] T. Zhang, H. Tang, and H. Li, 'Chemometrics in laser-induced breakdown spectroscopy', *J. Chemom.*, vol. 32, no. 11, p. e2983, Nov. 2018, doi: 10.1002/cem.2983.
[82] J. Dong *et al.*, 'A method for improving the accuracy of calibration-free laser-induced breakdown spectroscopy (CF-LIBS) using determined plasma temperature by genetic algorithm (GA)', *J. Anal. At. Spectrom.*, vol. 30, no. 6, pp. 1336–1344, 2015, doi: 10.1039/C4JA00470A.
[83] S. Pandhija and A. K. Rai, 'In situ multielemental monitoring in coral skeleton by CF-LIBS', *Appl. Phys. B*, vol. 94, no. 3, pp. 545–552, Mar. 2009, doi: 10.1007/s00340-008-3343-5.
[84] A. Limbeck, P. Galler, M. Bonta, G. Bauer, W. Nischkauer, and F. Vanhaecke, 'Recent advances in quantitative LA-ICP-MS analysis: challenges and solutions in the life sciences and environmental chemistry', *Anal. Bioanal. Chem.*, vol. 407, no. 22, pp. 6593–6617, Sep. 2015, doi: 10.1007/s00216-015-8858-0.
[85] A. S. Solovkin and Z. N. Tsvetkova, 'Modern methods of separating zirconium and hafnium', *Russ. Chem. Rev.*, p. 16, 1967.
[86] D. Han, N. Hatada, and T. Uda, 'Chemical Expansion of Yttrium-Doped Barium Zirconate and Correlation with Proton Concentration and Conductivity', 2016, doi: 10.1111/jace.14377.
[87] J. H. T. Bates, P. D. Sly, J. Sato, B. L. K. Davey, and B. Suki, 'Correcting for the Bernoulli effect in lateral pressure measurements', *Pediatr. Pulmonol.*, vol. 12, no. 4, pp. 251–256, Apr. 1992, doi: 10.1002/ppul.1950120410.

Table of Figures

List of tables